Karlsruhe Institute of Technology

Light trapping using correlated disordered media for planarized solar cells

Zur Erlangung des akademischen Grades eines
Doktors der Naturwissenschaften
(Dr. rer. nat.)

von der KIT-Fakultät für Physik
des Karlsruher Instituts für Technologie (KIT)

angenommene
DISSERTATION

von

M.Sc. Prerak Dhawan

am Institut für Theoretische Festkörperphysik

Tag der mündlichen Prüfung: 01.12.2023

Referent:	Prof. Dr. Carsten Rockstuhl
Korreferent:	Prof. Dr. Ralf Wehrspohn

Selbstständigkeitserklärung

Eidesstattliche Versicherung gemäß §13 Absatz 2 Ziffer 3 der Promotionsordnung des Karlsruher Instituts für Technologie (KIT) für die KIT-Fakultät für Physik:

1. Bei der eingereichten Dissertation zu dem Thema
   Light trapping using correlated disordered media for planarized solar cells
   handelt es sich um meine eigenständig erbrachte Leistung.

2. Ich habe nur die angegebenen Quellen und Hilfsmittel benutzt und mich keiner unzulässigen Hilfe Dritter bedient. Insbesondere habe ich wörtlich oder sinngemäß aus anderen Werken übernommene Inhalte als solche kenntlich gemacht.

3. Die Arbeit oder Teile davon habe ich wie folgt/ bislang nicht an einer Hochschule des In- oder Auslands als Bestandteil einer Prüfungs- oder Qualifikationsleistung vorgelegt.

   Titel der Arbeit:
   Light trapping using correlated disordered media for planarized solar cells,

   Hochschule und Jahr:
   KIT-Fakultät für Physik des Karlsruher Instituts für Technologie (KIT), 2023,

   Art der Prüfungs- oder Qualifikationsleistung:
   Dissertation.

4. Die Richtigkeit der vorstehenden Erklärungen bestätige ich.

5. Die Bedeutung der eidesstattlichen Versicherung und die strafrechtlichen Folgen einer unrichtigen oder unvollständigen eidesstattlichen Versicherung sind mir bekannt. Ich versichere an Eides statt, dass ich nach bestem Wissen die reine Wahrheit erklärt und nichts verschwiegen habe.

Karlsruhe, den 22.10.2023,

. . . .
M.Sc. Prerak Dhawan

Abstract

The history of solar cells is marked by a journey of innovation and discovery that has paved the way for a sustainable energy future. Since their inception, solar cells, also known as photovoltaic cells, have witnessed significant advancements in materials, technology, and efficiency. As the world faces critical challenges, including climate change, diminishing fossil fuel reserves, and the ever-increasing demand for clean energy, solar cells have emerged as a beacon of hope. The efficiency of solar cells plays a pivotal role in their significance. The pursuit of a high solar cell efficiency is of particular significance due to the increasingly limited availability of land for solar cell installations in the near future. For this purpose, integrating dielectric nanostructures into solar cells for the purpose of light management have recently emerged as a highly favoured approach for reducing the reflection loss from the front interface of the solar cell and increasing the absorption of the sunlight. This choice is more favourable when compared to the traditional approaches like direct texturing of the light-absorbing layer, as the dielectric nanostructures, when integrated into a standard planar solar cell, successfully overcome the detrimental impact on electrical performance due to texturing while also increasing the light absorption in comparison to a planar solar cell.

In this thesis, we investigate the utilization of correlated disorder in the design of dielectric nanostructures. The resulting structures are used for planar crystalline silicon solar cells. The approach used in the thesis involves designing a spatially inhomogeneous distribution of material. It builds upon an existing notion of a smoothly varying refractive index coating being an ideal broadband anti-reflection structure for solar cells. However, due to light reciprocity, such planarized anti-reflection coatings also increase the portion of outcoupled light not absorbed in the solar cell. We discuss a graded-index based design strategy that includes lateral features for light-trapping in the solar cell. By introducing index variation along the lateral direction, the incoupled light can be scattered inside the absorbing medium of the solar cell into oblique angles, thereby trapping the light in the system while also serving the purpose of an anti-reflection coating. Our final structures contain lateral features tailored towards a correlated, hyperuniform disorder while individual scattering elements are designed seeking inspiration from transformation optics. The resulting metasurface designed this way, was experimentally realized on macroscopically large wafers using self-assembly nanofabrication and atomic layer deposition techniques by experimental partners from the Martin-Luther University Halle-Wittemberg. We numerically and experimentally demonstrate that our disordered graded-index metasurface can significantly improve the light-trapping and antireflective performance of a solar cell.

Contents

List of Figures

List of publications

Peer-reviewed journal articles

6. **Dhawan, P.,** Gaudig, M., Sprafke, A., Wehrspohn, R. B. & Rockstuhl, C. Light-trapping structures for planar solar cells inspired by transformation optics. *Optics Express* **29,** 19903–19919 (2021)
7. **Dhawan, P.,** Schulte, L., Piechulla, P., Augenstein, Y., Gaudig, M., Sprafke, A., Wehrspohn, R. B. & Rockstuhl, C. On the reliability of the collective coordinate method to simulate metasurfaces with correlated disorder used for light management. *Journal of the Optical Society of America B* **40,** B8–B18 (2023)
8. Piechulla, P. M., Slivina, E., Bätzner, D., Fernandez-Corbaton, I., **Dhawan, P.,** Wehrspohn, R. B., Sprafke, A. N. & Rockstuhl, C. Antireflective Huygens' metasurface with correlated disorder made from high-index disks implemented into silicon heterojunction solar cells. *ACS Photonics* **8,** 3476–3485 (2021)
9. **Dhawan, P.,** Gaudig, M., Sprafke, A., Piechulla, P., Wehrspohn, R. B. & Rockstuhl, C. Anti-Reflective Graded-Index Metasurface with Correlated Disorder for Light Management in Planar Silicon Solar Cells. *Advanced Optical Materials,* 2302964 (2024)

Conference contributions

1. **Dhawan, P.,** Gaudig, M., Sprafke, A., Wehrspohn, R. B. & Rockstuhl, C. Planar light-trapping structures based on Schwarz-Christoffel mappings. *SPIE Photonics West, San Francisco, USA* (2021)
2. **Dhawan, P.,** Gaudig, M., Piechulla, P., Sprafke, A., Wehrspohn, R. B. & Rockstuhl, C. Anti-reflective conformal gradient index structures with correlated disorder for planar Silicon solar cells. *Metamaterials Congress, Siena, Italy* (2022)
3. **Dhawan, P.,** Gaudig, M., Piechulla, P., Sprafke, A., Wehrspohn, R. B. & Rockstuhl, C. Anti-reflective metasurface with tailored and correlated disorder for light-management in solar cells. *DisoMAT, Plankstetten, Germany* (2023)
4. **Dhawan, P.,** Gaudig, M., Piechulla, P., Sprafke, A., Wehrspohn, R. B. & Rockstuhl, C. Gradient-index Metasurface with Correlated Disorder for Light-management in Solar Cells. *Metamaterials Congress, Crete, Greece* (2023)

1 Introduction

Long before the first World Environment Day was celebrated in 1972 to increase general public awareness of environmental challenges, scientists were hinting at harnessing the limitless power of the sun to address pressing energy challenges. In the late 1800s, French engineer and mining expert, Louis Simonin, was one among many others who voiced fears about the inevitable depletion of the world's coal reserves. In response to the exhausting coal mines, Simonin suggested that researchers should turn their attention toward the Sun as a potential energy source of the future, writing "We must learn to bottle the sunbeams" [1]. In 1883, an American inventor Charles Fritts made the first solar cell by coating selenium with a thin layer of gold [2]. While Fritts had envisioned his solar cells as contenders against coal-fired power plants, their less-than-one-percent efficiency rendered them far from a practical energy solution. The concept of harnessing the Sun's radiant energy to power our world has since evolved from a compelling idea to a vital necessity.

In the ongoing global shift toward sustainable and renewable energy sources, photovoltaics will play a pivotal role in power generation. In 2022, photovoltaics contributed around 60.8 TWh of energy to the public grid in Germany, accounting for nearly 11% of the total electricity consumption. This represents a substantial increase compared to less than 2% contribution in 2010 [3, 4]. With a projected total electricity consumption of approximately 650 TWh by 2030, photovoltaics is anticipated to constitute over 30% of the total. Meeting this energy demand requires a substantial expansion of installed PV capacity while also ensuring high conversion efficiencies for solar cells. The pursuit of high solar cell efficiency is of particular significance due to the increasingly limited availability of land for solar cell installations in the near future.

Modern solar cells boast significantly higher conversion efficiencies when compared to Fritts' 1% efficiency solar cells. By stacking different semiconductor materials on top of each other to make a multi-junction solar cell, researchers are attempting to surpass the theoretical efficiency limit of 29.4% for a single-junction silicon solar cell and convert sunlight into electricity even more efficiently [5, 6]. Already this year (2023), Fraunhofer-Institut für Solare Energiesysteme and NWO-Institute AMOLF, successfully fabricated one such multi-junction solar cell with highest ever efficiency of 36.1% for silicon-based solar cells [7].

Silicon-based solar cells remain a crucial component within the expanding sustainable energy sector, with a market share of over 90% [4]. Such a remarkable market domination prevails despite silicon's band gap being slightly too small for optimal absorption of the solar radiation, and having a low absorption coefficient from being an indirect semiconductor. Such a strong hold in the market is because of the natural abundance of silicon on Earth, and its well-established use in the semiconductor manufacturing industry. Furthermore, silicon is known to be environmentally safe, posing no biohazards or environmental risks and holding no adverse effects on human health. However, to use this naturally occurring silicon in photovoltaics, a process of purification and crystallization is imperative [8].

In this thesis, we will use crystalline silicon (c-Si) as the light-absorbing material. Silicon, as mentioned earlier, has a low absorption coefficient in the spectral region where the solar irradiation is largest. Therefore, it is of paramount importance to enhance the interaction of incident light within the absorbing medium while minimizing reflection losses from the solar cell [9]. One well-established, and arguably a widely adopted approach, involves directly structuring the light-absorbing layer. The texturing of the interface induces diffused scattering of incident light inside the absorbing medium. This increases the optical path length thereby leading to an enhanced light absorption [10]. Remarkably, by randomizing the texture, it becomes possible to randomize the angular distribution of light, approaching the thermodynamic limit of light-trapping [11]. A particularly promising candidate for such a surface texture is *black silicon* texture for crystalline silicon (c-Si) solar cells [12]. This texture consists of stochastically arranged nano- to micrometer-sized, tapered Si needles, giving rise to broadband and quasi-omnidirectional strong suppression of back reflection and light-trapping close to the thermodynamic limit [12, 13].

Although nanotextures like black silicon offer excellent optical properties for the aforementioned reasons, they often lead to a degradation of the solar cell's electronic properties. This degradation arises because texturing the absorber layer introduces additional defects during the fabrication process and, due to the significant increase in surface area, results in a higher total number of defect sites [12, 14]. These defect states contribute to increased surface recombination current, which ultimately reduces the output current and, consequently, the solar cell's efficiency. In essence, despite black silicon's exceptional optical properties, these advantages do not necessarily translate into an increased short-circuit current due to prevailing electrical losses.

Recent research has demonstrated that applying conformal thin-film coatings to electronically passivate the texture can effectively recover most of the electrical degradation introduced during the fabrication process. However, the increase in surface area is inherent to texturing the interface. As a result, surface recombination for solar cells with textured interfaces will always be higher compared to an untextured interface [15, 16]. Therefore, planar interfaces are highly favored, and various light-trapping and light management strategies employing metallic grating structures [17], photonic crystals [18], dielectric nanospheres [19–21], disordered metasurfaces [P3, 22], and many more have been explored to achieve enhanced broadband absorption enhancement.

In this thesis, we capitalize on the notion of correlated disorder to realize geometrically disordered photonic structures that can directly be integrated onto a planar solar cell. Unlike a periodic structure where the angular distribution of the scattered light is limited by the periodicity of the scattering elements, the angular distribution of the scattered light for a disordered structure is larger thus offering more light-scattering channels. Tailoring the correlational statistics of the scatterers comprising the disorder can then utilize these light-scattering channels to give a broadband absorption enhancement. Moreover, disordered systems, where the correlational statistics are directly determined from an interaction potential, can often be fabricated on large surfaces in a cost-effective manner using colloidal self-assembly techniques [23].

The primary objective of this thesis lies in designing all-dielectric disordered structures whose scattering response mimics correlated disordered surface textures. This way, the resulting structures preserve the geometrical flatness but are optically like a textured interface. The optical and electronic properties of the textured interface are, therefore, decoupled, and the resulting structure can be integrated onto a planar silicon. To address this challenge, the approach adopted in this thesis is rather unique. We utilize a spatially inhomogeneous material distribution as an anti-reflection and light-trapping structure for planar solar cells. The intuition behind such a structure comes from the fact that a smoothly varying refractive index distribution in the longitudinal direction (along the illumination axis) is known to give good anti-reflection properties [24–26]. While the refractive index distribution along the lateral direction can potentially give good light-trapping properties. The "recipe" for designing such structures in this thesis is as follows:

- In the first stage, the refractive index distribution is obtained using transformation optics. Using a conformal coordinate transformation, a textured interface is mapped onto a planar interface. The resulting graded index structure inherits the statistical properties of a disordered texture. Through this modeling approach, an optimally performing planar light-trapping structure is obtained by determining an optimally performing surface texture.

- At a later stage, we leave the notion of an "optimal texture" altogether. In this modeling approach, the graded index structures are directly parameterized within a parameter space accessible for its experimental realization. Here, the optimally performing planar light-trapping structure is obtained by optimizing the reciprocal space scattering response of the structure along with other geometrical parameters characterizing the graded index structure.

Furthermore, the novelty of the work presented in the thesis goes beyond designing the graded index structures. The computational analysis for such correlated disordered structures remains a bottleneck since capturing its long-ranged scattering response requires considering a sufficiently large simulation domain. To overcome this, we use the collective coordinate method to identify small computational domains that preserve the spatial correlation statistics of the larger system, and that are more feasible for a computational analysis.

Thesis structure

After an introduction, the chapters are organized as follows:

- **Chapter 2** provides an extensive theoretical background needed for discussing the research methods and the obtained results in the subsequent chapters. The chapter comprises of five parts. The first part introduces the Maxwell equations and fundamentals of electromagnetic wave theory. This knowledge is utilized throughout the thesis for understanding the optical properties of the considered structures. The second part discusses the theory of transformation optics and outlines a few important aspects of conformal coordinate transformations needed for designing spatially inhomogeneous light-trapping structures. The third section covers the fundamental aspects of solar cells that are necessary for understanding the light-trapping and anti-reflection strategies used in the thesis. The fourth section describes the statistical properties that quantify the disordered-ness in a system. These properties are used for tailoring the scattering properties of a corrugated surface texture and of discrete particles. Finally, the fifth part discusses the numerical methods used throughout the thesis for simulating the optical response of the designed systems.

- **Chapter 3** discusses the application of transformation optics in designing light-trapping structures for thin-film solar cells. We use conformal coordinate transformations to map a disordered textured interface onto a planar equivalent. The resulting inhomogeneous and planar light-trapping structures have similar optical functionality as a textured interface and are anticipated to have improved electrical properties.

- **Chapter 4** extensively studies how positional disorder in a system can be tuned using its statistical properties to give a prescribed scattering response. With the help of a collective coordinate optimization, we obtain unique ground-state spatially disordered configurations that can be deployed in a disordered metasurface for solar cells. Later, we describe an alternate configuration that can be fabricated on larger surfaces using self-assembly methods. Finally, we use the same optimization procedure to realize small-scale disordered samples that can circumvent the need for ensemble-averaging in the system.

- **Chapter 5** utilizes the knowledge of designing an inhomogeneous media using transformation optics, and designing a disordered metasurface using statistical properties of a correlated disorder, to ultimately design a graded index metasurface with correlated disorder. The design strategy and parameterization for such a structure directly come from the fabrication constraints imposed by the available technology. We experimentally and numerically demonstrate the superior optical performance for such disordered graded index metasurfaces throughout the parametric space of the fabricated samples.

- **Chapter 6** summarizes this thesis and provides an outlook on the prospective research topics that are beyond the scope of the work presented.

2 Theoretical background and computational methods

This chapter aims at introducing the essential theoretical and computational concepts employed throughout the thesis for generating and interpreting the results. Section 2.1 focuses on the fundamentals of electromagnetic wave theory required for understanding light propagation in a medium. Section 2.3 describes the working principles and optical properties of a solar cell while also discussing the use of light-trapping for solar cells. Section 2.2 focuses on fundamentals of transformation optics and conformal transformations for designing a prescribed inhomogeneous medium. Section 2.4 emphasises on the statistical properties of surface roughness and positional disorder that are later used for designing light-scattering elements. Finally, Sec. 2.5 discusses the numerical methods used for simulating the electromagnetic response from a given solar-cell. These simulations are either based on the finite-difference frequency-domain or the finite-difference time-domain method which we discuss briefly.

2.1 Electromagnetic wave theory

This section summarizes equations that govern the propagation of electromagnetic waves and puts them into context. We start from expressing the macroscopic Maxwell's equations in an arbitrary coordinate system and elaborate on its form-invariance. This aspect will be important when we later outline in Sec. the details of transformation optics. Next, the angular spectrum representation is introduced followed by reflection and transmission of plane waves at a planar interface. Finally the duality transformation of Maxwell's equations is briefly discussed. These aspects will be important when describing light propagation in the structures of relevance throughout the thesis.

2.1.1 Maxwell's equations

To describe the propagation of electromagnetic fields through a medium, we rely on the Maxwell equations in their macroscopic formulation. These equations govern the relationship between electric and magnetic fields in a given medium and are solved for a given set of boundary conditions. For an inhomogeneous medium, they can be written in space-time domain as [27]

$$\nabla \cdot \mathbf{D}(\mathbf{r},t) = \rho(\mathbf{r},t)\,, \tag{2.1}$$

$$\nabla \times \mathbf{E}(\mathbf{r},t) = -\frac{\partial \mathbf{B}(\mathbf{r},t)}{\partial t}\,, \tag{2.2}$$

$$\nabla \cdot \mathbf{B}(\mathbf{r},t) = 0\,, \tag{2.3}$$

$$\nabla \times \mathbf{H}(\mathbf{r},t) = \frac{\partial \mathbf{D}(\mathbf{r},t)}{\partial t} + \mathbf{J}(\mathbf{r},t)\,, \tag{2.4}$$

where $\mathbf{E}(\mathbf{r},t)$ and $\mathbf{H}(\mathbf{r},t)$ are the electric and magnetic fields, $\mathbf{D}(\mathbf{r},t)$ is the electric displacement, $\mathbf{B}(\mathbf{r},t)$ is the magnetic flux density, and $\rho(\mathbf{r},t)$ and $\mathbf{J}(\mathbf{r},t)$ are charge and current densities, respectively. The relationship between the electric and magnetic field ultimately comes through the constitutive relations given as,

$$\mathbf{D}(\mathbf{r},t) = \varepsilon_0\mathbf{E}(\mathbf{r},t) + \mathbf{P}(\mathbf{r},t)\,, \tag{2.5}$$

$$\mathbf{B}(\mathbf{r},t) = \mu_0(\mathbf{H}(\mathbf{r},t) + \mathbf{M}(\mathbf{r},t))\,, \tag{2.6}$$

where $\mathbf{P}(\mathbf{r},t)$ and $\mathbf{M}(\mathbf{r},t)$ are the polarization and magnetization while ε_0 and μ_0 are the electric permittivity and magnetic permeability of free space. These equations are invariant under a coordinate transformation. It implies that the form of Maxwell's equation remains unchanged in an arbitrary coordinate frame, i.e., in a curved space, such that

$$\nabla' \cdot \mathbf{D}'(\mathbf{r}',t) = \rho'(\mathbf{r}',t)\,, \tag{2.7}$$

$$\nabla' \times \mathbf{E}'(\mathbf{r}',t) = -\frac{\partial \mathbf{B}'(\mathbf{r}',t)}{\partial t}\,, \tag{2.8}$$

$$\nabla' \cdot \mathbf{B}'(\mathbf{r}',t) = 0\,, \tag{2.9}$$

$$\nabla' \times \mathbf{H}'(\mathbf{r}',t) = \frac{\partial \mathbf{D}'(\mathbf{r}',t)}{\partial t} + \mathbf{J}'(\mathbf{r}',t)\,, \tag{2.10}$$

holds, where the respective quantities are now in a primed coordinate space. This implies that for any geometry, no matter how distorted, these expressions hold locally.

To understand this, let us rewrite Eqns. 2.1-2.4 in a covariant notation for compactness. For simplicity, we assume that the medium responds instantaneously, linearly but anisotropically to the electric field $\mathbf{E}(\mathbf{r},t)$ such that $\mathbf{D}(\mathbf{r},t) = \boldsymbol{\varepsilon}(\mathbf{r})\mathbf{E}(\mathbf{r},t)$ and $\mathbf{B}(\mathbf{r},t) = \boldsymbol{\mu}(\mathbf{r})\mathbf{H}(\mathbf{r},t)$. Please note that equipping Maxwell's equations with such constitutive relation in time domain is a rare exception and sensitively hinges on the assumption that the material responds instantaneously, i.e., it is assumed to be non-dispersive. A theoretically more solid approach to capture material properties in time domain is introduced later in the section and is based on response functions. The Maxwell equations can then be written as

$$\partial_i \varepsilon^{ij} E_j = \rho\,, \tag{2.11}$$

$$\epsilon^{ijk}\partial_j E_k = -\mu^{ij}\frac{\partial H_j}{\partial t}\,, \tag{2.12}$$

$$\partial_i \mu^{ij} H_j = 0\,, \tag{2.13}$$

$$\epsilon^{ijk}\partial_j H_k = \varepsilon^{ij}\frac{\partial E_j}{\partial t} + J_i\,, \tag{2.14}$$

where ϵ^{ijk} is the anti-symmetric Levi-Cevita pseudo tensor. The indices (i, j, k) each take values from 1 to 3 and repeated indices get summed over. The differential $\partial_i = \partial/\partial x_i$ represents the partial derivative with respect to the particular coordinate x_i.

Under a coordinate transformation $x \mapsto x'$, where the primed entity signifies the transformed space, electric and magnetic fields transform as [28]

$$E'_i = \mathcal{J}_{i'}^{i} E_i \,, \tag{2.15}$$

$$H'_i = \mathcal{J}_{i'}^{i} H_i \,, \tag{2.16}$$

where $\mathcal{J}_{i'}^{i}$ is the inverse of the transposed Jacobian matrix associated with the coordinate transformation given as, $\mathcal{J}_i^{i'} = \partial x_{i'}/\partial x_i$. Using the chain-rule for transforming the partial derivatives $\partial_{i'} = (\partial x_i/\partial x_{i'})\partial_i = \mathcal{J}_{i'}^{i}\partial_i$, one can substitute Eq. 2.15 and Eq. 2.16 to Eq. 2.12 to get,

$$\epsilon^{ijk}\partial_j\left(\mathcal{J}_k^{k'}E_{k'}\right) = -\mu^{ij}\frac{\partial\left(\mathcal{J}_j^{j'}H_{j'}\right)}{\partial t} \,. \tag{2.17}$$

Upon using $\epsilon^{i'j'k'}\det(\mathcal{J}_l^{l'}) = \mathcal{J}_i^{i'}\mathcal{J}_j^{j'}\mathcal{J}_k^{k'}\epsilon^{ijk}$, one can simplify this above expression further to get,

$$\epsilon^{i'j'k'}\partial_{j'}E_{k'} = -\left(\frac{\mathcal{J}_i^{i'}\mathcal{J}_j^{j'}}{\det(\mathcal{J})}\right)\mu^{ij}\frac{\partial H_{j'}}{\partial t} \,, \tag{2.18}$$

which is essentially the covariant form of Eq. 2.8, where $\mu^{i'j'} = \frac{\mathcal{J}_i^{i'}\mathcal{J}_j^{j'}}{\det(\mathcal{J})}\mu^{ij}$ is the permeability in the transformed space. Likewise, one can show this for the remaining Maxwell equations. These expressions are summarized in the same order as Eqns. 2.11-2.14 below:

Transformed space	Tranformed quantites
$\partial_{i'}\varepsilon^{i'j'}E_{j'} = \rho'$	$\rho' = \rho/\det(\mathcal{J})$
$\epsilon^{i'j'k'}\partial_{j'}E_{k'} = -\mu^{i'j'}\frac{\partial H_{j'}}{\partial t}$	$\boldsymbol{\mu}' = (\mathcal{J}\mu\mathcal{J}^T)/\det(\mathcal{J})$
$\partial_{i'}\mu^{i'j'}H_{j'} = 0$	
$\epsilon^{i'j'k'}\partial_{j'}H_{k'} = \varepsilon^{i'j'}\frac{\partial E_{j'}}{\partial t} + J_{i'}$	$\boldsymbol{\varepsilon}' = (\mathcal{J}\varepsilon\mathcal{J}^T)/\det(\mathcal{J})$, $\mathbf{J}' = \mathcal{J}\mathbf{J}/\det(\mathcal{J})$

Table 2.1: Transformed Maxwell's equations and their corresponding quantities.

As a consequence, the free-space Maxwell equations in arbitrary coordinates are equivalent to the macroscopic Maxwell's equations in Eqns. 2.1-2.4 in Cartesian space such that the information of the coordinate space is captured in the material properties $\boldsymbol{\varepsilon}'$, $\boldsymbol{\mu}'$, charge density ρ', and current density $\mathbf{J}'$. This form-invariance of Maxwell's equations is further discussed and utilized in Sec. 2.2.

Since the Maxwell's equations described above are in space-time domain, one can switch to a space-frequency domain for time-harmonic systems and under the assumption that the material responds only linearly to the electromagnegtic field. As nonlinear effects are only noticeable at field amplitudes that significantly exceed those considered in this thesis, this is a fair assumption. The Fourier transformed field, $\tilde{\mathbf{E}}(\mathbf{r},\omega)$ is related to $\mathbf{E}(\mathbf{r},t)$ as

$$\begin{aligned}\mathbf{E}(\mathbf{r},t) &= \int_{-\infty}^{+\infty} \tilde{\mathbf{E}}(\mathbf{r},\omega)e^{-\mathrm{i}\omega t}\mathrm{d}\omega \,, \\ \tilde{\mathbf{E}}(\mathbf{r},\omega) &= \frac{1}{2\pi}\int_{-\infty}^{+\infty} \mathbf{E}(\mathbf{r},t)e^{\mathrm{i}\omega t}\mathrm{d}t \,.\end{aligned} \tag{2.19}$$

The Maxwell's equations in space-frequency domain then read as

$$\nabla \cdot \tilde{\mathbf{D}}(\mathbf{r},\omega) = \tilde{\rho}(\mathbf{r},\omega) \,, \tag{2.20}$$

$$\nabla \times \tilde{\mathbf{E}}(\mathbf{r},\omega) = \mathrm{i}\omega\tilde{\mathbf{B}}(\mathbf{r}\,,\omega) \,, \tag{2.21}$$

$$\nabla \cdot \tilde{\mathbf{B}}(\mathbf{r},\omega) = 0 \,, \tag{2.22}$$

$$\nabla \times \tilde{\mathbf{H}}(\mathbf{r},\omega) = -\mathrm{i}\omega\tilde{\mathbf{D}}(\mathbf{r},\omega) + \tilde{\mathbf{J}}(\mathbf{r},\omega) \,, \tag{2.23}$$

with the constitutive relations for linear, isotropic, local, achiral, reciprocal and dispersive media written as

$$\tilde{\mathbf{D}}(\mathbf{r},\omega) = \varepsilon_0\varepsilon_r(\mathbf{r},\omega)\tilde{\mathbf{E}}(\mathbf{r},\omega) \,, \tag{2.24}$$

$$\tilde{\mathbf{B}}(\mathbf{r},\omega) = \mu_0\mu_r(\mathbf{r},\omega)\tilde{\mathbf{H}}(\mathbf{r},\omega) \,, \tag{2.25}$$

where $\varepsilon_r(\mathbf{r},\omega)$ and $\mu_r(\mathbf{r},\omega)$ are the relative permitivity and permeability, respectively. Please note, even though many assumptions were made above concerning the properties of the medium, they hold for all the materials relevant to the thesis. Assuming a non-magnetic medium ($\mu_r(\mathbf{r},\omega) = 1$), we can arrive at the wave equation by taking $\nabla\times$ of Eq. 2.20 and using the constitutive relations to give,

$$\nabla \times \nabla \times \tilde{\mathbf{E}}(\mathbf{r},\omega) - \omega^2\mu_0\varepsilon_0\mu_r(\omega)\varepsilon_r(\mathbf{r},\omega)\tilde{\mathbf{E}}(\mathbf{r},\omega) = i\omega\mu_0\mu_r(\omega)\tilde{\mathbf{J}}(\mathbf{r},\omega) \,. \tag{2.26}$$

In the absence of free electric charges and currents, the Helmholtz wave equations for a homogeneous medium ($\varepsilon(\mathbf{r},\omega) = \varepsilon(\omega)$) can be derived from Eq. 2.26. The resulting wave equations for electric and magnetic fields will be,

$$\nabla^2\tilde{\mathbf{E}}(\mathbf{r},\omega) + k^2(\omega)\tilde{\mathbf{E}}(\mathbf{r},\omega) = 0 \,, \tag{2.27}$$

$$\nabla^2\tilde{\mathbf{H}}(\mathbf{r},\omega) + k^2(\omega)\tilde{\mathbf{H}}(\mathbf{r},\omega) = 0 \,, \tag{2.28}$$

where, the wavenumber k is given as

$$k(\omega) = \omega\sqrt{\mu_0\varepsilon_0\mu_r(\omega)\varepsilon_r(\omega)} = \frac{\omega}{c}\underline{n}(\omega) \,. \tag{2.29}$$

Here, $\underline{n}(\omega) = n(\omega) + i\kappa(\omega)$ is the complex refractive index of the medium with $n(\omega)$ being the refractive index and $\kappa(\omega)$ being the extinction coefficient of the medium.

The elementary solution to Eq. 2.27 are elliptically polarized plane waves

$$\tilde{\mathbf{E}}(\mathbf{r}, \omega) = \tilde{\mathcal{E}}_1(\omega)e^{\mathrm{i}\boldsymbol{k}(\omega)\cdot\mathbf{r}} + \tilde{\mathcal{E}}_2(\omega)e^{-\mathrm{i}\boldsymbol{k}(\omega)\cdot\mathbf{r}} , \tag{2.30}$$

where $\tilde{\mathcal{E}}_1(\omega)$ and $\tilde{\mathcal{E}}_1(\omega)$ are the vectorial amplitudes and are dependent on the specific initial and boundary conditions for the system. An arbitrary solution to Maxwell's equations in the homogeneous space can then always be written as a superposition of these plane waves. For spatially inhomogenous media, unfortunately, these elementary analytical solutions are no longer possible, and numerical techniques are usually needed to solve Maxwell's equations in such scenario. The techniques used in this thesis are discussed briefly in Sec. 2.5.

Once the solution to the Maxwell equations for an arbitrary material distribution and a given illumination are determined, the energy contained in these time-harmonic fields can be calculated using Poynting's theorem while evaluating the following volume integral:

$$\frac{1}{2}\int_V \mathbf{E}(\mathbf{r}) \cdot \mathbf{J}^*(\mathbf{r})\mathrm{d}V . \tag{2.31}$$

Using Eqns. 2.21 and 2.23, this can be expanded as [27]:

$$\frac{1}{2}\int_V \mathbf{E}(\mathbf{r}) \cdot \mathbf{J}^*(\mathbf{r})\mathrm{d}V = \frac{1}{2}\int_V \mathbf{E}(\mathbf{r}) \cdot (\boldsymbol{\nabla} \times \mathbf{H}^*(\mathbf{r}) - \mathrm{i}\omega\mathbf{D}^*(\mathbf{r}))\,\mathrm{d}V \tag{2.32}$$

$$= -\frac{1}{2}\int_V \boldsymbol{\nabla} \cdot (\mathbf{E}(\mathbf{r}) \times \mathbf{H}^*(\mathbf{r}))\,\mathrm{d}V - \frac{1}{2}\int_V \mathrm{i}\omega\,(\mathbf{E}(\mathbf{r}) \cdot \mathbf{D}^*(\mathbf{r}) - \mathbf{B}(\mathbf{r}) \cdot \mathbf{H}^*(\mathbf{r}))\,\mathrm{d}V , \tag{2.33}$$

where we used the vector identity $\boldsymbol{\nabla} \cdot (\mathbf{A} \times \mathbf{B}) = \mathbf{B} \cdot (\boldsymbol{\nabla} \times \mathbf{A}) - \mathbf{A} \cdot (\boldsymbol{\nabla} \times \mathbf{B})$. The above equation can further be written as,

$$\underbrace{\frac{1}{2}\int_V \mathbf{E}(\mathbf{r}) \cdot \mathbf{J}^*(\mathbf{r})\mathrm{d}V}_{\mathrm{I}} + \underbrace{2\mathrm{i}\omega\int_V (W_e - W_m)\mathrm{d}V}_{\mathrm{II}} + \underbrace{\oint_S \mathbf{S} \cdot \hat{\mathbf{n}}\mathrm{d}A}_{\mathrm{III}} = 0 , \tag{2.34}$$

where W_e, W_m, and $\mathbf{S}$ are the electric and magnetic energy densities, and the complex Poynting vector, respectively. These are given as,

$$W_e = \frac{1}{4}\left(\mathbf{E}(\mathbf{r}) \cdot \mathbf{D}^*(\mathbf{r})\right) \qquad W_m = \frac{1}{4}\left(\mathbf{B}(\mathbf{r}) \cdot \mathbf{H}^*(\mathbf{r})\right) \qquad \mathbf{S} = \frac{1}{2}\left(\mathbf{E}(\mathbf{r}) \times \mathbf{H}^*(\mathbf{r})\right) \tag{2.35}$$

where we used Gauss's divergence theorem to transform the volume integral into a closed surface integral. Equation 2.34 is, in general, complex whose real part gives the energy conservation condition for time-harmonic fields. The real part of term I in Eq. 2.34 expresses the time-averaged rate of work done by the fields in the volume V whereas the real part of term III expresses the time-averaged flow of power into the volume V through the bounding surface **A**. Naturally, the real part of term II would only be non-zero when the volume integral is imaginary, or in other words, the system is dissipative ($\Im\{\varepsilon\} \neq 0$ or $\Im\{\mu\} \neq 0$). Assuming a non magnetically dissipative material ($\Im\{\mu_r\} = 0$), the imaginary part of term II can be simplified for a linear, isotropic and lossy media as,

$$A = \frac{1}{2}\omega \int_V \Im\left\{\mathbf{E}(\mathbf{r}) \cdot (\varepsilon_0 \varepsilon(\mathbf{r})^* \mathbf{E}^*(\mathbf{r}))\right\} \mathrm{d}V \tag{2.36}$$

$$= -\frac{1}{2}\omega\varepsilon_0 \int_V \varepsilon''(\mathbf{r}) \left|\mathbf{E}(\mathbf{r})\right|^2 \mathrm{d}V\,, \tag{2.37}$$

where $\varepsilon''(\mathbf{r})$ is the imaginary part of the permittivity. The integrand of Eq. 2.37 represents the local absorption. The global absorption is found by integrating this spatially dependent absorption across a given volume. We shall use this quantity in Chap. 3, where we calculate absorption in thin layers of textured and planar crystalline silicon that are considered to be a part of a solar cell.

2.1.2 Angular Spectrum Representation

The elementary plane wave solution for the Helmholtz equation can be used for expansion of the electromagnetic field in scattering problems. The plane wave solutions of Eqns. 2.27 and 2.28 are given by:

$$\mathbf{E}(\mathbf{r}, \omega) = \tilde{\mathbf{E}}_0(\mathbf{k}, \omega) e^{i\mathbf{k}\cdot\mathbf{r}} \tag{2.38}$$

$$\mathbf{H}(\mathbf{r}, \omega) = \tilde{\mathbf{H}}_0(\mathbf{k}, \omega) e^{i\mathbf{k}\cdot\mathbf{r}}. \tag{2.39}$$

The wave vector $\mathbf{k}$ specifies the propagation direction, and $\mathbf{E}_0(\mathbf{k}, \omega)$ and $\mathbf{H}_0(\mathbf{k}, \omega)$ specify the vectorial field amplitudes. A generalized solution of the Helmholtz equations can be obtained by using the angular spectrum representation. In such a representation, an arbitrary field can be series expanded as a linear superposition of such plane waves. Of course, since Eqns. 2.27 and 2.28 are written for a homogeneous medium, the plane wave expansion is also applicable only in a homogeneous medium. The angular spectrum representation is found to be a very convenient method to describe several scattering problems including laser beam propagation and beam focusing. In this method, the optical fields in a given plane are Fourier-expanded in terms of propagating (real-valued $\mathbf{k}$) and evanescent plane waves (complex $\mathbf{k}$) with variable amplitudes and propagation directions. Then, to desribe the propagation of that initial field, each plane wave experiences a multiplication with an exponential function whose argument is purely real for propagating waves and complex for evanescent or damped waves. And the final field distribution is merely the inverse Fourier transform. We shall use the formalism derived from this section for describing the scattered light from various geometries considered throughout the thesis and for the purpose to quantitatively understand the need for light-trapping in solar-cells.

Consider a spatially dependent and time-harmonic field with amplitude $\mathbf{E}(\mathbf{r})$. This can be a solution of a scattering problem or the illumination field at a certain distance from its source. We consider that the field propagates along $+z$-direction, and we know the field in a plane $(x, y, z = 0)$. Then, we calculate the two-dimensional Fourier transform of the field $\mathbf{E}(x, y, 0)$, similar to Eq. 2.19, but now in two-dimensional space, this will yield [29]

$$\tilde{\mathbf{E}}(k_x, k_y; 0) = \frac{1}{4\pi^2} \int_{-\infty}^{+\infty} \int_{-\infty}^{+\infty} \mathbf{E}(x, y, 0) e^{-\mathrm{i}(k_x x + k_y y)} \mathrm{d}x \mathrm{d}y \, , \tag{2.40}$$

and an inverse Fourier transform will give the field in real space:

$$\mathbf{E}(x, y, 0) = \frac{1}{4\pi^2} \int_{-\infty}^{+\infty} \int_{-\infty}^{+\infty} \tilde{\mathbf{E}}(k_x, k_y; 0) e^{\mathrm{i}(k_x x + k_y y)} \mathrm{d}k_x \mathrm{d}k_y \, . \tag{2.41}$$

Since the integrands of Eqns. 2.40 and 2.41 are vector quantities, it is implied that the Fourier integrals hold separately for each vector component. Similarly, the Fourier-transform for the fields at a distant plane for $z \neq 0$ gives

$$\mathbf{E}(x, y, z) = \int_{-\infty}^{+\infty} \int_{-\infty}^{+\infty} \tilde{\mathbf{E}}(k_x, k_y; z) e^{-\mathrm{i}(k_x x + k_y y)} \mathrm{d}k_x \mathrm{d}k_y \, , \tag{2.42}$$

Since the fields $\mathbf{E}(\mathbf{r})$ at $\mathbf{r} = (x, y, z)$ must be a solution of Eq. 2.27 for a fixed frequency ω, one can substitute Eq. 2.42 in Eq. 2.27 to obtain the following solution for a lossless medium for each plane wave components,

$$\tilde{\mathbf{E}}(k_x, k_y; z) = \tilde{\mathbf{E}}(k_x, k_y; 0) e^{\mathrm{i}k_z z} \, . \tag{2.43}$$

Here $k_z = \sqrt{k^2 - k_x^2 - k_y^2}$ is the z-component of the wave vector with wavenumber $k = n\omega/c$ and $\Im\{k_z\} \geq 0$. From Eq. 2.42, it is apparent that, as we move away from the $z = 0$ plane, each Fourier component of the field at $\mathbf{r} = (x, y, 0)$ acquires a phase factor $e^{\mathrm{i}k_z z}$. Since k_z can be real or imaginary, there are two scenarios:

$$\text{Propagating waves} \longrightarrow k_x^2 + k_y^2 \leq k^2 \, , \tag{2.44}$$

$$\text{Evanescent waves} \longrightarrow k_x^2 + k_y^2 > k^2 \, . \tag{2.45}$$

With these conditions, we can, in fact, see that the field in an arbitrary z-plane is a superposition of the propagating ($\Im\{k_z\} = 0$) and evanescent plane waves ($\Im\{k_z\} > 0$). By substituting Eq. 2.43 in Eq. 2.42, we finally get the following expression for the field in terms of its angular spectrum representation

$$\mathbf{E}(x, y, z) = \int_{-\infty}^{+\infty} \int_{-\infty}^{+\infty} \tilde{\mathbf{E}}(k_x, k_y; 0) e^{-\mathrm{i}(k_x x + k_y y + k_z z)} \mathrm{d}k_x \mathrm{d}k_y \, . \tag{2.46}$$

If the coefficients $\tilde{\mathbf{E}}(k_x, k_y; 0)$ are known, the power carried in each of the plane waves characterized by a given $k_x - k_y$ pair reads as,

$$P(k_x, k_y; 0) = \frac{n}{2Z_0} \left| \tilde{\mathbf{E}}(k_x, k_y; 0) \right|^2 \cos\theta, \tag{2.47}$$

where $Z_0 = \sqrt{\mu_0/\varepsilon_0}$ is the impedance of vacuum, n is the refractive index of the medium, and θ is the scattering angle between propagation direction $\hat{\boldsymbol{k}}$ and $\hat{z}$ such that $\cos\theta = \Re\{k_z/k\}$. The total power contained in the field can then be obtained by summing this quantity over all $\boldsymbol{k}$.

2.1.3 Fresnel equations at an interface

Until now, we considered only the electromagnetic fields in a given medium. For actual problems, the propagation of the electromagnetic fields at an interface separated by two media should also be considered. This will allow us to study the transmission and reflection of a plane wave from an interface and ultimately be a guiding tool for designing light-trapping and anti-reflection layers for solar cells. The behavior of the fields at material interfaces is obtained using Gauss' and Stokes' theorem [27]. Let us consider an interface between medium 1 and medium 2 with normal vector $\hat{\mathbf{n}}$. Then, the components of the electric and magnetic fields that are parallel to the surface are related by

$$\hat{\mathbf{n}} \times (\mathbf{E}_1 - \mathbf{E}_2) = 0 \,, \tag{2.48}$$

$$\hat{\mathbf{n}} \times (\mathbf{H}_1 - \mathbf{H}_2) = \mathbf{J} \,, \tag{2.49}$$

where $\mathbf{J}$ is the surface current density. The components of the dielectric displacement field and magnetic induction that are perpendicular to the surface are related by

$$\hat{\mathbf{n}} \cdot (\mathbf{D}_1 - \mathbf{D}_2) = \sigma \,, \tag{2.50}$$

$$\hat{\mathbf{n}} \cdot (\mathbf{B}_1 - \mathbf{B}_2) = 0 \,, \tag{2.51}$$

where σ is the surface charge density. In the absence of free charges and currents, Eqns. 2.49 and 2.51 show that the parallel components of the $\mathbf{E}$ and $\mathbf{B}$ are continuous across the interface. Also, the perpendicular components of $\mathbf{D}$ and $\mathbf{B}$ are continuous across the interface. In such a case, the perpendicular component of $\mathbf{E}$ is discontinuous across the interface. Assuming both the media to be isotropic, homogeneous, and non-magnetic, this discontinuity is given by

$$\hat{\mathbf{n}} \cdot \mathbf{E}_1 = \frac{\varepsilon_2}{\varepsilon_1} \hat{\mathbf{n}} \cdot \mathbf{E}_2 \,, \tag{2.52}$$

where ε_1 and ε_2 are the permittivities of medium 1 and medium 2, respectively. With this, one can study the behavior of a plane wave incident at an oblique angle onto a planar material interface.

Reflection and Transmission

Consider a linearly polarized plane wave impinging on a planar interface at an angle θ_i with respect to the normal. Both the medium are assumed to be isotropic, homogeneous, and non-magnetic media. This allows us to describe the fields in each medium using plane waves. Since an arbitrarily polarized plane wave can be decomposed into two orthogonal linearly polarized plane waves, we can express the incident field as a sum of field components that are parallel and perpendicular to the interface, such that $\mathbf{E}_i = \mathbf{E}_{i,\parallel} + \mathbf{E}_{i,\perp}$ with the first and second terms more commonly referred to as "transverse magnetic (TM)" mode and "transverse electric (TE)" mode, respectively. This decomposition of the electric field is illustrated in Fig. 2.1.

The magnitudes of the wave vectors in the two media are $k_i = k_r = \underline{n}_1\omega/c$ and $k_t = \underline{n}_2\omega/c$ where $\underline{n}_1 = \sqrt{\varepsilon_1}$ and $\underline{n}_2 = \sqrt{\varepsilon_2}$ are refractive indices of medium 1 and medium 2, respectively.

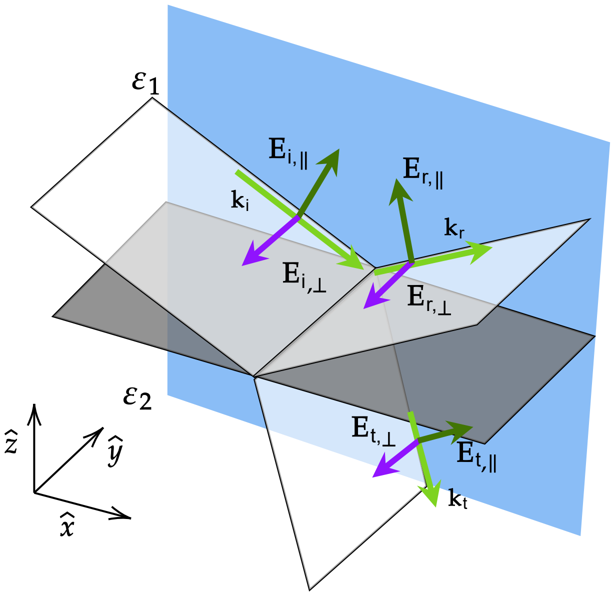

Figure 2.1: Illustration of an electromagnetic field with wave vector $\mathbf{k}_i$ incident on an interface between two media with permittivities ε_1 and ε_2. The interface (grey) lies in the x-y plane. The wave vectors $\mathbf{k}_i$, $\mathbf{k}_r$, and $\mathbf{k}_t$ (light green) all lie in the plane of incidence (blue). The parallel components $\mathbf{E}_{i,\parallel}$, $\mathbf{E}_{r,\parallel}$, and $\mathbf{E}_{t,\parallel}$ (dark green) lie in x-z plane. The perpendicular components $\mathbf{E}_{i,\perp}$, $\mathbf{E}_{r,\perp}$, and $\mathbf{E}_{t,\perp}$ (purple) lie in x-y plane.

Since the perpendicular components of the electric field is continuous across the interface, the phase factor of the incident, reflected, and transmitted plane waves have to be the same such that,

$$(\mathbf{k}_i \cdot \mathbf{r})_{z=0} = (\mathbf{k}_r \cdot \mathbf{r})_{z=0} = (\mathbf{k}_t \cdot \mathbf{r})_{z=0} \ . \tag{2.53}$$

With this relation, it can be seen that the angle of incidence θ_i and the angle of reflection θ_r are identical. Moreover, one can obtain Snell's law which relates the angle of refraction to the angle of incidence

$$\underline{n}_1 \sin\theta_i = \underline{n}_2 \sin\theta_t \ . \tag{2.54}$$

By using the continuity of parallel component of electric field $\mathbf{E}_\parallel$ and magnetic field $\mathbf{H}_\parallel$ across the interface, one can derive the following relations:

$$E_{r,\perp} = r_\mathrm{s} E_{i,\perp} \ , \quad E_{r,\parallel} = r_\mathrm{p} E_{i,\parallel} \ , \tag{2.55}$$

$$E_{t,\perp} = t_\mathrm{s} E_{i,\perp} \ , \quad E_{t,\parallel} = t_\mathrm{p} E_{i,\parallel} \ , \tag{2.56}$$

where r_s and t_s are the reflection and transmission Fresnel coefficients for the perpendicular component (TE) while r_p and t_p are the reflection and transmission coefficients for the parallel component (TM), respectively. These coefficients are given as [29],

$$r_\mathrm{s} = \frac{\underline{n}_1 \cos\theta_i - \underline{n}_2 \cos\theta_t}{\underline{n}_1 \cos\theta_i + \underline{n}_2 \cos\theta_t}\,, \quad r_\mathrm{p} = \frac{\underline{n}_2 \cos\theta_i - \underline{n}_1 \cos\theta_t}{\underline{n}_2 \cos\theta_i + \underline{n}_1 \cos\theta_t}\,, \tag{2.57}$$

$$t_\mathrm{s} = \frac{2\underline{n}_1 \cos\theta_i}{\underline{n}_1 \cos\theta_i + \underline{n}_2 \cos\theta_t}\,, \quad t_\mathrm{p} = \frac{2\underline{n}_1 \cos\theta_i}{\underline{n}_2 \cos\theta_i + \underline{n}_1 \cos\theta_t}\,, \tag{2.58}$$

where $\underline{n}_{1,2}$ are the refractive indices of medium 1 and 2, θ_i is the incident and also the back-reflected angles while θ_t is the transmitted angle with each angle measured with respect to the normal of the interface. Using these coefficients, the reflectance and transmittance for both the polarizations read as

$$R_\mathrm{s,p} = |r_\mathrm{s,p}|^2\,, \quad T_\mathrm{s,p} = \Re\left\{\frac{\underline{n}_2 \cos\theta_t}{\underline{n}_1 \cos\theta_i}\right\} |t_\mathrm{s,p}|^2\,. \tag{2.59}$$

For a non-absorbing medium, $R_\mathrm{s,p} + T_\mathrm{s,p} = 1$. By defining a medium's impedance as $Z = \sqrt{\mu/\varepsilon}$, the reflection and transmission coefficients can be obtained in terms of impedance Z_1 and Z_2 for medium 1 and medium 2, respectively. From Eqns. 2.57, 2.58, and 2.59, it can be easily seen that at normal incidence ($\theta_i = \theta_t = 0$), the back reflection from the interface can greatly be reduced when the impedance mismatch between two media is minimized i.e., when $Z_1 \approx Z_2$. For an air-silicon interface, this impedance mismatch is very large. This increases the reflectance from the device, ultimately decreasing its absorption. Therefore, it is important to reduce this impedance mismatch through various light-trapping and anti-reflection coatings is a primary subject of the thesis.

2.1.4 Duality Symmetry and the Helicity operator

In this subsection, we briefly introduce the concept of duality and helicity operator through its link to the polarization state of plane waves. These concepts play an important role in the thesis for designing anti-reflective nanostructures based on their ability to preserve helicity.

The helicity operator Λ is defined as the projection of the angular momentum operator $\mathbf{J}$ onto the direction of the linear momentum operator $\mathbf{P}$. For monochromatic but spatially dependent fields, it is the curl operator divided by the wave number:

$$\Lambda = \frac{\mathbf{J}\cdot\mathbf{P}}{|\mathbf{P}|} \equiv \frac{\nabla\times}{k}\,. \tag{2.60}$$

Electromagnetic duality can be defined as a continuous transformation rotating electric and magnetic fields onto each other [30, 31]:

$$\tilde{\mathbf{E}}_\theta(\mathbf{r},\omega) = \tilde{\mathbf{E}}(\mathbf{r},\omega)\cos\theta + Z\tilde{\mathbf{H}}(\mathbf{r},\omega)\sin\theta\,, \tag{2.61}$$

$$Z\tilde{\mathbf{H}}_\theta(\mathbf{r},\omega) = Z\tilde{\mathbf{H}}(\mathbf{r},\omega)\cos\theta - \tilde{\mathbf{E}}(\mathbf{r},\omega)\sin\theta\,, \tag{2.62}$$

where θ is an arbitrary real-valued angle, and Z is the impedance of a medium. If $Z = Z_0$ (in vacuum), Maxwell's equations are symmetric under the above transformation. This means that if the electromagnetic field ($\tilde{\mathbf{E}}(\mathbf{r}, \omega)$, $\tilde{\mathbf{H}}(\mathbf{r}, \omega)$) is a solution to Maxwell's equations, the transformed field ($\tilde{\mathbf{E}}_\theta(\mathbf{r}, \omega)$, $\tilde{\mathbf{H}}_\theta(\mathbf{r}, \omega)$) is also a solution. However, in the presence of matter, the symmetry of Maxwell's equations is broken [32]. In general, the system is dual symmetric if and only if its electric and magnetic responses to impinging radiation are equivalent (Sec. 6.11 of [27]). The helicity operator has two different eigenvalues, $\lambda \pm 1$. The associated eigenvectors, $\tilde{\mathbf{G}}_\pm(\mathbf{r}, \omega)$ are the Riemann-Silberstein vectors given as [33]:

$$\tilde{\mathbf{G}}_\pm(\mathbf{r}, \omega) = \frac{1}{\sqrt{2}} \left(\tilde{\mathbf{E}}(\mathbf{r}, \omega) \pm \mathrm{i} Z \tilde{\mathbf{H}}(\mathbf{r}, \omega) \right) . \tag{2.63}$$

These eigenvalues can be used as an index for defining the polarization state of a given field: For plane waves, the fields of pure helicity correspond to circularly polarized plane waves with right handed and left handed polarized light being eigenstates with eigenvalues $\lambda = +1$ and $\lambda = -1$, respectively. This implies, for a right circularly polarized plane wave, $\tilde{\mathbf{G}}_-(\mathbf{r}, \omega)$ is always zero and vice versa. In general, the plane wave decomposition of any field which is an eigenvector of Λ with eigenvalues ± 1 contains only right/left circularly polarized plane waves.

Helicity is the generator of duality transformations: Helicity and duality are related like angular momentum and spatial rotations or linear momentum and spatial translations. Light-matter interaction for incident radiation with pure helicity can then be understood by categorizing objects into dual symmetric objects that preserve helicity and non-dual symmetric objects that do not. For non-dual symmetric objects, the scattered light can then be described as a linear combination of the eigenstates defined in Eq. 2.63. We shall use these concepts in Chap. 4 for describing the scattered light from nanostructures arranged in periodic or tailored disordered arrangement and its consequential anti-reflective properties when integrating this arrangement to solar cells.

2.2 Fundamentals of Transformation Optics

In this section, we will introduce the theory of transformation optics and outline few important aspects of conformal coordinate transformations. We will utilize this knowledge in Chap. 3 for designing light-trapping and anti-reflection structures using transformation optics.

One of the most immediate implications of the form-invariance of Maxwell's equations summarized in Tab. 2.1 is that light propagation in a non-trivial set of coordinates can be mimicked with a spatially inhomogeneous optical media. The exact parameters of this optical media are completely specified by the coordinate transformation [34, 35]. This realization has allowed engineering of materials with very unique electromagnetic properties and applications. Examples would be negative refraction, optical cloaking, flat lenses, and many more. This section discusses the fundamental aspects of Transformation Optics (TrO) and how it can be used as a guiding tool for creating novel devices and structures. While maintaining its consistency and elegance, the general framework of TrO necessitates the materials to possess anisotropic properties, defined by permittivity and permeability. Designing such materials within this framework remains a challenging task in materials science. In this context, we shall also discuss how a reduced set of constitutive parameters can be achieved by using conformal transformation. Additionally, we will provide a brief overview of a specific conformal transformation that will be employed in subsequent chapters of this thesis.

2.2.1 Background

Considering the transformation from a Cartesian system, the anisotropic permittivity $\boldsymbol{\epsilon}'$ and permeability $\boldsymbol{\mu}'$ of the transformed space are obtained from:

$$\begin{aligned} \boldsymbol{\varepsilon}' &= \frac{\mathcal{J}\varepsilon\mathcal{J}^T}{\det(\mathcal{J})} , \\ \boldsymbol{\mu}' &= \frac{\mathcal{J}\mu\mathcal{J}^T}{\det(\mathcal{J})} , \end{aligned} \tag{2.64}$$

where ϵ and μ are the permittivity and permeability of the embedding isotropic medium in the Cartesian coordinates, respectively, while $\mathcal{J}$ is the Jacobian for the transformation. It is interesting to note that even if one starts with isotropic materials (scalar ε and μ), after the coordinate transformation, the constitutive parameters can, in general, be anisotropic. Consider the following transformation:

$$x' = \alpha x , \tag{2.65}$$

$$y' = y , \tag{2.66}$$

$$z' = z . \tag{2.67}$$

This transformation consists of stretching the space in one direction. The relative permitivitty and permeability for such a mapping when transformed from vacuum ($\varepsilon_r = \mu_r = 1$) are given by:

$$\boldsymbol{\varepsilon}' = \boldsymbol{\mu}' = \mathrm{diag}(\alpha, 1, 1) . \tag{2.68}$$

The anisotropy can then be understood by observing that the stretching of space by a factor of α solely along one direction results in scaling of the permitivitty and permeability solely along that direction and remains unchanged in the other directions. While the transformed parameters conveniently come out as diagonal matrices here, for more general problems, this is not the case.

The design process for obtaining an electromagnetic device that performs a prescribed task consists of multiple steps. First, one needs to find an appropriate coordinate mapping that realizes the desired electromagnetic functionality in transformed space: the space is transformed in such a way that the light propagates along trajectories according to a predefined path. The intended functionality is inscribed in that path. Now, the actual transformed coordinate system, of course, cannot exist in reality, but we can reinterpret the transformation in terms of a material distribution in an ordinary Cartesian space. Then, we can map the obtained coordinate transformation onto the material tensors $\boldsymbol{\varepsilon}'$ and $\boldsymbol{\mu}'$ for using it in the original space. This design process provides an unprecedented control over light-matter interactions and has been used for designing metasurface cloaks [34–38], waveguide bends [39–41], plasmonic nanoantennas [42, 43], and flattened lenses and reflectors [44–47]. For an extensive review of applicability of TrO and its future prospects, the reader is refered to [48, 49] for an overview.

2.2.2 Conformal Mapping

If we restrict ourselves to the xy-plane, and assume the un-transformed space to be isotropic, the constitutive parameters resulting from a general mapping can be determined from Eq. 2.64 for which the permitivitty tensor can be expressed as,

$$\boldsymbol{\varepsilon}' = \varepsilon \frac{\mathcal{J}\mathcal{J}^T}{\det(\mathcal{J})} = \frac{\varepsilon}{\det(\mathcal{J})} \begin{bmatrix} \partial_x x'^2 + \partial_y x'^2 & \partial_x x' \partial_x y' + \partial_y x' \partial_y y' & 0 \\ \partial_x x' \partial_x y' + \partial_y x' \partial_y y' & \partial_x y'^2 + \partial_y y'^2 & 0 \\ 0 & 0 & 1 \end{bmatrix} , \tag{2.69}$$

where $x' = x'(x, y)$ and $y' = y'(x, y)$ are the coordinates in the transformed space with $z' = z$ and the partial derivatives are with respect to the unprimed coordinates. A similar expression can be obtained for the permeability in the transformed space.

For the TrO medium to be isotropic in two-dimensions, a transformation $w : \mathbb{C} \longrightarrow \mathbb{C}$ can be chosen where the real and imaginary parts of the transformation represent the coordinates in the new space. By letting $w = f(z)$ where $w = x' + iy'$ and $z = x + iy$, and if the transformed coordinates satisfy the Cauchy Riemann conditions:

$$\partial_x x' = \partial_y y' , \qquad \partial_x y' = -\partial_y x' , \tag{2.70}$$

then the mapping is conformal. Since a Jacobian matrix can generally be written as $\mathcal{J} = \boldsymbol{U}\boldsymbol{\Lambda}$ where $\boldsymbol{U}$ is a 2×2 unitary matrix (such that $\boldsymbol{U}^T = \boldsymbol{U}^{-1}$) and $\boldsymbol{\Lambda} = \mathrm{diag}(a, b)$, satisfying Eq. 2.70 implies the matrix product $\mathcal{J}\mathcal{J}^T$ is proportional to the unitary matrix $\boldsymbol{I}$, which is only possible when $a = b$. Geometrically, this means that the transformed coordinates are stretched isotropically at any given point in space.

Figure 2.2 shows one such conformal map where a mapping from Fig. 2.2(a) to Fig. 2.2(b) locally preserves the angles between intersecting grid lines (black and green). Moreover, their aspect ratios at any given point are preserved. Both aspects imply that the transformed coordinate system remains locally orthogonal. For such a mapping, the permittivity and permeability tensors reduces to a simpler form:

$$\begin{aligned} \boldsymbol{\varepsilon}' &= \mathrm{diag}\left(1, 1, \frac{1}{\det(\mathcal{J})}\right) \varepsilon , \\ \boldsymbol{\mu}' &= \mathrm{diag}\left(1, 1, \frac{1}{\det(\mathcal{J})}\right) \mu . \end{aligned} \tag{2.71}$$

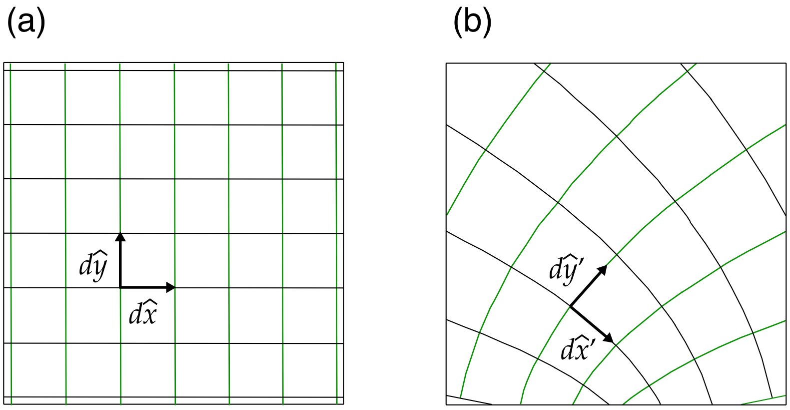

Figure 2.2: Illustration of a conformal transformation. Lines of constant x and y are shown in each domain.

Although a misnomer, devices designed this way are often called 'isotropic' and 'all-dielectric' in literature whereas the resulting medium is generally uniaxial anisotropic and inhomogeneous in nature [50]. However, if the polarization of the incident light is restricted to the 'TE'-mode and the untransformed medium is non-magnetic ($\epsilon_z, \mu_x = 1, \mu_y = 1$), the only parameter to be controlled is the refractive index, which, from Eq. 2.29, yields

$$n'(x', y') = \sqrt{\varepsilon'_z} = n_0 \left|\frac{dw}{dz}\right|^{-1}, \tag{2.72}$$

with n_0 being the refractive index of the untransformed dielectric space. The optical conformal map can thus be seen as a special case of a generalized TrO formulation wherein the information of the transformation is condensed into only one material parameter. While discovering conformal transformations for certain applications like all-dielectric cloaks [34], collimators [51], and few others is trivial, finding a suitable conformal map for obtaining an arbitrary optical functionality may not be trivial and/or feasible in many cases as there is no single straightforward algorithm for it.

One approach to make these transformations as flexible as possible consists in the application of the Schwarz-Cristoffel mapping that we discuss in the following subsection.

2.2.2.1 Schwarz-Christoffel mapping

Here we look at special kind of conformal transformations, namely Schwarz-Christoffel transformations (SCT) that allows us to conformally map two regions in a straightforward process. The intuition behind it and its variations is that the derivative of a conformal transformation $w = f(z)$ can be expressed as

$$f'(z) = C \prod_{l}^{m-1} f_l(z), \tag{2.73}$$

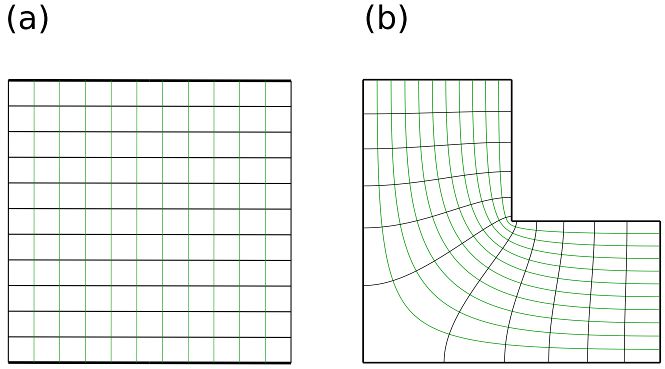

Figure 2.3: Illustration of Schwarz-Christoffel mappings from a) regular complex plane to b) 90° bend polygon and c) Upper half-space above a triangular interface. These are numerically generated using MATLAB SC Toolbox [53].

for certain canonical functions $f_l(z)$ where m specifies the number of vertices that are to be mapped. Such a function has the property that $\arg(f') = \sum \arg(f_l)$. So, if the $\arg(f_l)$ is made a step function (angle subtended between edges joining the vertices) then the resulting $\arg(f')$ is piecewise constant with discrete jumps. Geometrically, this implies that the function f maps the real axis onto a given polygon with m vertices. Using a fundamental theorem of Schwarz-Christoffel mapping, for a polygon with vertices $w_1, w_2, .., w_m$ such that $w_l = f(z_l)$ for $k = 1, 2, .., m-1$, the mapping function f has the following form [52]:

$$w = f(z) = f(z_0) + C\int_{z_0}^{z}\prod_{i=1}^{m}(\tilde{z} - z_i)^{(\phi_i/\pi)-1}\mathrm{d}\tilde{z}, \tag{2.74}$$

where ϕ_i is the angle subtended by the i$^{\text{th}}$ corner and $z_1, z_2, \ldots, z_m$ are the prevertices. The complex constants $f(z_0)$ and C are for translating and scaling the map, respectively. Equation 2.74 maps the interiors of a polygon onto the complex upper half-space. The equation can be adapted to map different regions such as the unit disk, exterior maps (mapping exterior of the polygon), piecewise analytic boundaries, and more. The desired mapping is then obtained by finding the prevertices for the given polygon through a parameter problem [52]. While the solution to this problem can be explicit and analytic for selected cases, for a majority of practical problems, there exists no analytical solution for the prevertices. For such cases, the parameter problem is solved through computational methods [53]. Figure 2.3 shows the transformed grid generated using SCT. The regular Cartesian space in subfigure (a) is mapped to a bent polygon in subfigure (b) and to the upper half-space above a textured interface in subfigure (c). Note that for both cases, the grid lines curve such that the angles between them are locally preserved due to the conformality of the map.

By taking advantage of this technique, several TrO devices have been proposed such as flat lenses, wide-angle flat reflectors, phase modulators, waveguide bends, directional antennas and many more [47, 54, 55]. Such devices would significantly facilitate their prospective fabrication. In contrast, conventional TrO maps, which are non-conformal, would be rather infeasible as they would often be anisotropic with extreme material parameters. In the context of solar cells, we will use the presented approach in Chap. 3 to map the half-space above the light-absorbing layer of our solar cell which contains the nanotexture (similar to Fig 2.3) to a planar interface without the texture.

2.3 Fundamentals of Solar cells

This section covers the fundamental aspects of solar cells and shall motivate the need for light-trapping and light-management strategies to enhance their performance. This section starts by discussing the working principle of a standard solar cell. Additionally, key quantitative measures are introduced for quantifying the optical efficiency of the overall device. These quantities are later used to understand light-trapping and light-management.

2.3.1 Working principle

A solar cell is a semiconductor device that essentially converts the impinging photons into electron-hole pairs. To excite the electron-hole pair by absorption of the photon, the photons must have a threshold energy $\hbar\omega = E_G$ where E_G is the band-gap energy of the semiconductor, and ω is the frequency of the incident photon. The photons with an energy greater than the band-gap, excites the negatively charged electrons into the conduction band of the semiconductor (nearly empty before excitation) from the valence band (nearly filled before excitation), leaving the positively charged voids (holes) behind. The electron-hole pair drift into different regions of the semiconductor. As a result, an electric potential difference builds up within the cell which, in return, generates a current in the final device. Photons with energy less than the bandgap are either reflected or transmitted by the semiconductor (ignoring weak absorption from phonons, impurities and free charge carriers) [56].

A standard solar cell consists of three functional elements: First, an absorbing medium with a *p*-*n* junction or a similar charge separation and extraction mechanism. Second, an anti-reflective structure on the front-interface (facing the incoming light). Third, two metallic contacts on each side of the solar cell for extracting the current. Figure 2.4(a) shows a typical geometry of such a solar cell highlighting these elements. Throughout the thesis, the absorber used for the solar cells is made from silicon. In that absorbing layer, the electron-hole pair generation takes place. The anti-reflective layer (shown in yellow) can be an optical element, like a metasurface, a planar anti-reflection coating or a textured absorbing medium itself. Its purpose is to minimize reflection from the front interface of the solar cell so that most of the incident light is incoupled to the absorbing medium underneath. While acting as an electrical interface, the back contact (shown in blue) can also serve the purpose of a reflector. With that, the back contact can prevent the light outcoupling through the backside. This suppression of the outcoupling ensures a longer optical path length of light in the absorbing medium, and therefore, a larger probability of light getting absorbed. Finding a suitable configuration of these interfaces (antireflection layer and back reflector) is discussed in Sec. 2.3.2.

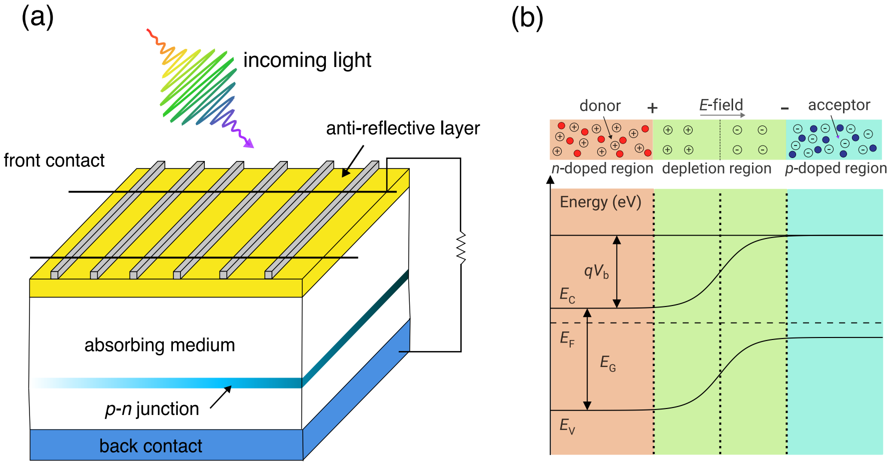

Figure 2.4: a) Geometry of a standard solar cell. The absorbing medium is sandwiched between the back and the front contact and contains a *p*-*n* junction for separating the electron-hole pairs generated from impinging photons. b) Schematic of a *p*-*n* junction shown in (a) and its energy band diagram in equilibrium as a function of space. The red and blue circles are the electrons and holes that drift and diffuse to the front and back contacts. E_C and E_V are the conduction and valence bands, E_F corresponds to the Fermi level, $E_G = E_C - E_V$ is the band gap of the semiconductor, and qV_b is a potential barrier with q and V_b being the elementary charge and the built-in potential, respectively.

The electron-hole pair generated in the absorbing medium eventually recombines and the electron returns to its initial energy state. This recombination can be either non-radiative (energy released as a phonon or transferred to another electron/hole) or radiative (photon emission). For crystalline silicon (c-Si), the dominating mechanism is the non-radiative Auger recombination where the energy and momentum is transferred to an other electron or hole [56]. Additionally, recombination can also occur at the surface of the absorbing medium. At these surface, the presence of dangling bonds or defect states can trap and recombine the charge carriers, reducing their lifetime, and affecting the overall efficiency of the semiconductor device. This is particularly crucial for textured absorbing layers where the fabrication process itself and the increase in the surface area from the texture increases the total number of defect sites [12].

Since the recombination of the charge carriers is inevitable, the absorbing medium must contain a semi-permeable membrane that separates the electron-hole pair and prevents their immediate recombination. This way, the electrons will diffuse only through one side of the membrane and the holes through the other. Typically, these membranes are formed by introducing a *p*-*n* junction in the absorbing medium. The formation of the *p*-*n* junction and the energy band diagram in its spatial region at equilibrium (no illumination) is shown in Fig. 2.4(b). Such a junction is formed by putting together *n*-type semiconductors (electrons as majority charge carriers) and *p*-type semiconductors (holes

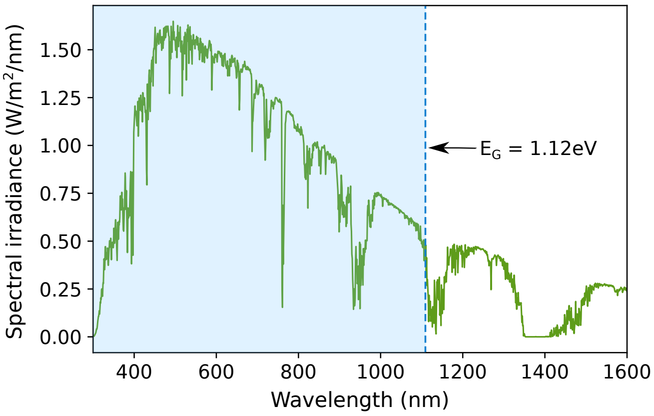

Figure 2.5: Solar spectral irradiance AM 1.5G as a function of the wavelength. The shaded region shows the spectral region of interest for a single junction silicon-based solar cells bounded by the band gap energy of silicon. The data is taken from [57].

as majority charge carriers). The n-type semiconductors are created by doping an intrinsic semiconductor with electron donor atoms, like Phosphorus (shown by positive charged circles in Fig. 2.4(b)). In contrast, the p-type semiconductors are created by doping the intrinsic semiconductor with electron acceptor atoms, like Boron or Gallium (shown by negatively charged circles in Fig. 2.4(b)). The electrons diffuse from the n-type to the p-type region across the junction whereas the holes diffuse from the p-type to the n-type region. Due to this diffusion of charge carriers, the junction is depleted of those carriers. What is left are fixed positively charged donor ions in the n-type region and fixed negatively charged acceptor ions in the p-type region. Due to the charges around this depletion region, an electric field is developed such that it opposes the movement of the diffusing charge carriers across the junction. This electric field gives rise to an electrostatic potential difference qV_b across the depletion region. Upon illumination by a photon with energy greater than E_G, the concentration of minority charge carriers in n-type and p-type regions (electrons for p-type and holes for n-type) increases with increasing photon flux. These minority charge carriers diffuse across the depletion layer and become majority carriers, thereby contributing to an electrical current.

A key criteria for the choice of the absorbing medium of a solar cell is the spectral irradiance $SI(\lambda)$ of the illumination, i.e, the solar spectrum. Figure 2.5 shows the solar irradiance spectrum AM 1.5G that is attenuated by the Earth's atmosphere [57]. It corresponds to the spectral irradiance at $1/\cos(\theta = 48.2°)$ where θ is the angle between the sun's position and the zenith (when sun is directly overhead). Since the peak of the spectral intensity is around 500 nm, the choice of the absorbing medium must be such that its absorption is considerable in this spectral region. Given the solar spectrum, the choice of silicon as a semiconductor material is justified by the shaded region in Fig. 2.5 where the photon energies greater than the band gap of silicon $E_G = 1.12$ eV are shown by the dashed line, which is approximately $\lambda_g = hc/E_G = 1108$ nm. However, due to silicon being an indirect band gap semiconductor, the cut off is not that abrupt, and a very small portion of light can still be absorbed by a fairly thick silicon wafer.

To quantify the optical quality and efficiency of the solar cell device, we use the photo-current density which is given as

$$J_{\mathrm{ph}} = e \int \varphi(\lambda) A(\lambda) \eta_{\mathrm{IQE}}(\lambda) \mathrm{d}\lambda \,, \tag{2.75}$$

where $A(\lambda)$ is the absorbance in the semiconductor, $\eta_{\mathrm{IQE}}(\lambda)$ is the internal quantum efficiency of the device which is the fraction of absorbed photons in the cell that generates an electron-hole pair, and $\varphi(\lambda)$ is the spectral photon flux that is related to the spectral irradiance as $\varphi(\lambda) = SI(\lambda)/(hc/\lambda)$. It is common to use the photo-current density as a figure of merit instead of photo-current directly. That serves the purpose to remove the dependence of the surface area of the final solar cell. A similar figure of merit can be obtained for evaluating the current density lost due to optical reflections from the front interface of the solar cell. That reflection loss current density is given as

$$J_{\mathrm{R}} = e \int \varphi(\lambda) R(\lambda) \eta_{\mathrm{IQE}} \mathrm{d}\lambda \,, \tag{2.76}$$

where $R(\lambda)$ is the reflectance from the front-side of the solar cell. Being spectrally averaged quantities, we use J_{ph} and J_R throughout the thesis as useful metrics for quantifying the anti-reflection and light trapping capabilities of the solar cell by evaluating them at a short and long wavelength range separately.

2.3.2 Light-trapping

From the photo-current and current-loss densities expressed in Eqns. 2.75 and 2.76, it is evident that for an optimal device, the absorbance in the semiconductor should be maximized whereas the reflectance from the front interface should be minimized. On the one hand, for maximizing the absorbance, it is necessary to suppress the reflection thereby improving light in-coupling in the device. On the other hand, a mere suppression of the back reflection does not guarantee a higher absorbance. This is because off-axis scattered photons inside the absorbing medium will have a longer optical path than the photons scattered along the axis of illumination and is, therefore, more likely to generate an electron-hole pair. Thus, it is equally necessary to increase the optical path length several times than the actual thickness of the absorbing layer to prevent the photons from leaving the solar cell without generating an electron-hole pair. The former condition is met by having anti-reflective features (for example, a coating) and the later by having light-trapping and light-management features (for example, a grating) in the solar cell.

The starting point for developing an anti-reflection strategy for silicon solar cells is realising that the impedance mismatch between air $Z_1 = \sqrt{\mu_0/\varepsilon_0}$ and c-Si $Z_2 = \sqrt{\mu_0/\varepsilon_{\mathrm{cSi}}}$ is fairly large at optical frequencies. Expressing Eq. 2.57 in terms of the impedances then conveys that the large impedance mismatch will result in a large back reflection. A standard approach is to apply a planar anti-reflective coating (ARC) over the front interface of c-Si with its index n_{ARC} at an operational wavelength λ_0 given by [58]:

$$n_{\mathrm{ARC}} = \sqrt{n_1 n_2}, \quad \lambda_0 = 4 n_{\mathrm{ARC}} t_{\mathrm{ARC}} \,, \tag{2.77}$$

where n_1 and n_2 are the refractive indices of air and c-Si, respectively, and t_{ARC} is the optimal thickness of such an anti-reflective coating. It can be seen that the refractive index of the ARC is the geometrical mean of the refractive indices of the two media. By stacking more of such layers, one could monotonically decrease the refractive index along the direction of illumination such that the reflection is suppressed not just for a single wavelength but a broadband spectral range. Several gradient index profiles have been proposed for such broadband reflection suppression [25, 59, 60]. However, due to light reciprocity, such planarized anti-reflection coatings would also increase the portion of outcoupled light which has not been absorbed from the first double-pass through the absorber layer (light reflected from the back interface). This can be avoided by having light-trapping features in the system that change the propagation of light inside the absorber. Ideally, not just the optical path should be increased but also a total internal reflection for the light after being reflected from the back interface should be achieved. This will ensure multiple passes of light through the cell thereby giving high absorbance even for a thin solar cell. To understand this, assume $I_0(\lambda)$ to be the incoupled light into the absorbing medium from the front-interface. The intensity of light propagating along the z-axis through an absorptive medium at lengths much longer than the wavelength is described using the Beer-Lambert law as

$$I(z, \lambda) = I_0(\lambda) e^{-\alpha(\lambda) z} \,, \tag{2.78}$$

where $\alpha(\lambda) = 4\pi\kappa(\lambda)/\lambda$ is the absorption coefficient of the material with its refractive index $\underline{n}(\omega) = n(\omega) + i\kappa(\omega)$ specified in Eq. 2.29. The fraction of light absorbed in the material is then

$$I_{\mathrm{abs}}(z, \lambda) = I_0(\lambda) \left(1 - e^{-\alpha(\lambda) z}\right) \,. \tag{2.79}$$

For a plane wave with wave vector $\mathbf{k}$ and traveling at an oblique angle, the absorbed light is then dependent on the angle the wave vector makes with the z-axis. Since we know from Sec. 2.1.2 that the fields can be expanded as a linear superposition of plane waves with variable amplitude and propagation direction, the absorbance in the medium can more generally be written as,

$$I_{\mathrm{abs}}(\lambda) = \int_{-\infty}^{+\infty} \int_{-\infty}^{+\infty} \tilde{\mathbf{I}}_0(k_x, k_y, \lambda) \left(1 - e^{-\alpha(\lambda) d / \cos\theta(k_x, k_y)}\right) \mathrm{d}k_x \mathrm{d}k_y, \tag{2.80}$$

where $\cos\theta(k_x, k_y) = \Re\{\sqrt{k - k_x^2 - k_y^2}/k\}$ expresses the angle of propagation of the plane waves with wavelength $\lambda = 2\pi/k$ relative to the z-axis, and $d = z/\cos\theta$ is the distance propagated inside the material of thickness d. It can then be easily seen that modes with $\theta \neq 0$ travel a path that is $1/\cos\theta$ times longer than the thickness of the material. It is therefore desirable to scatter the light at oblique angles into the absorbing medium thus giving a light-trapping behaviour. The need for light trapping in silicon solar cells is even more apparent for wavelength beyond 600 nm where the absorption coefficient $\alpha(\lambda)$ is fairly small and, from Eq. 2.80, therefore needs to be compensated by a much longer optical path length.

When considering absorption in the active layer of a solar cell, it is also crucial to consider the thickness of this region. As evident in Eq. 2.80 and Eq. 2.37, decreasing the thickness or the volume of the active layer will trivially decrease the absorption. This implies that there is a higher probability of photons escaping before being fully absorbed. While this effect does not play a major role for wafer-based silicon solar cells that are hundreds of microns thick, for thin film solar cells with thickness $t < 50$ µm, the limited volume to absorb the sunlight must be compensated by increasing the optical path length within the active layer. Therefore, for thin solar cells, optimizing light-trapping and light-management strategies is essential to yield a higher energy conversion efficiency.

Common light-trapping and light-management strategies for silicon solar cells include textured interfaces, resonant scatterers, mirrors as a back-reflector, and/or a combination of all. The efficiency of these methods are compared against the ideal Lambertian scatterer that uniformly scatters the incident illumination of any angular distribution, into an angular distribution that has a $\cos\theta$ dependency. The maximum achievable path length enhancement β from such a scatterer in the weakly absorbing limit is shown to be $\beta = 4n^2$ where n is the refractive index of the absorbing medium [11]. The design and specific forms of light trapping structures, periodic and disordered are a primary subject of this thesis and are discussed in detail in the further chapters.

2.4 Characteristics of disorder

A primary goal of this thesis is understanding and tailoring the scattering properties of disordered media when integrated onto a standard solar cell for enhancing its optical performance. To fully appreciate the details of disordered media and to be able to discuss their properties, it is necessary to introduce key concepts that quantitatively describe the nature of the disorder in these systems and how it can be tailored at will for a desired optical response. In the first subsection, we describe for that purpose the spatial features of a randomly rough interface. This is used in Chap. 3 for designing a textured interface of the absorbing layer of the solar cell. The second subsection discusses positional type of disorder and its statistics. The spatial point patterns characterized with this disorder are used in Chap. 4 and Chap. 5 for placing scattering elements at these locations on top of the planarized solar cell.

2.4.1 Surface Roughness

As described previously, it is important to fully characterize the spatial features of the disordered surface roughness for a textured solar cell as it will give spectral control over the scattering response of the system and, ultimately, yield a broadband absorption enhancement. The randomly rough surface textures are characterized by their statistical properties, which include the continuous height distribution and height correlation functions. The height distribution determines the spread of the texture heights above or below a mean level. This height distribution is often a Gaussian, which, unlike a random uniform distribution, has a specific root-mean-squared value (RMS) height profile. For a one-dimensional texture, this is given by:

$$\sigma = \sqrt{\frac{1}{L}\int_L h^2(x)dx}\,, \tag{2.81}$$

where the height profile spans the spatial extent L. The RMS roughness σ gives an insight on how strongly corrugated a texture is vertically. However, the horizontal separation between these spatial features cannot be captured in such a metric since it does not correlate the height at any given point to the height at neighbouring points. Such a correlation can be expressed using a height-height correlation function given as

$$W(s) = \frac{\int_L [h(x) - h(x+s)]^2 dx}{\int_L h(x)h(x)dx}\,. \tag{2.82}$$

For disordered rough surfaces, $W(s)$ typically increases strongly for small distances and then saturates at longer distances. The distance beyond which it saturates is called the correlation length ζ.

In order to design a surface texture for coupling light with wave vector $\boldsymbol{k}$, it is important to consider these features in the Fourier space instead. A quantity in the Fourier space, called Power Spectral Density (PSD), can be defined as

$$\tilde{P}(q) = \frac{1}{L}\left|\int_L h(x)e^{-\mathrm{i}qx}dx\right|^2, \tag{2.83}$$

where q is the reciprocal lattice vector of the one-dimensional height profile. For each q, $\tilde{P}(q)$ contains the amplitude of the Fourier component of the height profile. For every non-zero amplitude, a finite lateral momentum can potentially be transferred to a plane wave and scatter it at an oblique angle. To actually get the fraction of light that is coupled to this reciprocal lattice vector, one has to rigorously solve Maxwell's equations numerically to obtain the scattered fields from such a textured interface in the Fourier space.

If we choose the correlation function to be of the form $W(s) = e^{-s^2/\zeta^2}$, one can obtain the PSD, which is essentially the Fourier transform of $W(s)$

$$\tilde{P}(q) = \sqrt{\pi}\zeta e^{-\zeta^2 q^2/4}. \tag{2.84}$$

Fixing this quantity, one can obtain a disordered textured profile with a prescribed σ and ζ by multiplying it with normally distributed random numbers and then taking an inverse Fourier transform to get the real-space coordinates of the profile. Mathematically, this is expressed as [61],

$$h(x) = \sigma\sqrt{\frac{2}{L}}\sum_{m=1}^{\infty}\tilde{P}\left(mq_0\right)\left[\alpha_{2m-1}\sin(mq_0x) + \alpha_{2m}\cos(mq_0x)\right], \tag{2.85}$$

where α is a normally distributed random number. Through such a parameterization of the texture profile, it is apparent that if $\tilde{P}(q)$ is non-zero for large q, the texture profile will be very rough and will statistically feature very high spatial frequencies details. In contrast, if $\tilde{P}(q)$ is zero for large q, the texture profile will be rather smooth and statistically feature only low spatial frequency details. It is to be noted that while the quantities described here are only for a one-dimensional profile, they can be scaled to a two-dimensional surface roughness without loss of generality.

2.4.2 Particle statistics and characterization

In this subsection, we investigate disordered systems that are categorized not by continuous variation of the height profiles, but rather by discrete point-objects that are spatially distributed in a given volume. The point patterns then represent the positions in space where the optical scatterers are to be placed in a system. It is then important to quantitatively study the distributions of the point patterns, their corresponding features in the reciprocal space, and potentially find a suitable spatial distribution that tailors the desired optical response. Here, we define quantities that characterize only a single microstate (one realization of the point pattern) and not a macrostate (ensemble average of multiple realizations).

Consider a system of N identical point particles with random coordinates $\mathbf{R}^N \equiv \mathbf{R}_1, \mathbf{R}_2, \ldots, \mathbf{R}_N$ in a volume V. We can define a single-particle density function (also called local number density) at position $\mathbf{r}$ as,

$$\rho(\mathbf{r}) = \sum_{i=1}^{N} \delta(\mathbf{r} - \mathbf{R}_i) , \tag{2.86}$$

where $\delta(\mathbf{r})$ is the Dirac-Delta function. Likewise, one can a define an n-particle density function $\rho_N^{(n)}(\mathbf{r}^n)$ which essentially expresses the likelihood of finding a specific configuration of n particles at the set of coordinates $\mathbf{r}^n \equiv \mathbf{r}_1, \mathbf{r}_2, \ldots, \mathbf{r}_n$ per combined volume element $d\mathbf{r}^n = d\mathbf{r}_1 d\mathbf{r}_2 \ldots d\mathbf{r}_n$. In other words, $\rho_N^{(n)}(\mathbf{r}^n) d\mathbf{r}^N$ is proportional to the probability of finding any n particles ($n \leq N$) with configuration $\mathbf{r}^n \equiv \mathbf{r}_1, \mathbf{r}_2, \ldots, \mathbf{r}_n$ in the volume element $d\mathbf{r}^n$. Based on this definition and Eq. 2.86, it is given as [62],

$$\rho_N^{(n)}(\mathbf{r}^n) = \rho_N^{(n)}(\mathbf{r}_1, \mathbf{r}_2, \ldots, \mathbf{r}_n) = \sum_{\substack{i,j,k,\ldots,s=1 \\ i \neq j \neq k \neq s}} \delta(\mathbf{r}_1 - \mathbf{R}_i) \ldots \delta(\mathbf{r}_s - \mathbf{R}_s) , \tag{2.87}$$

as well as the n-particle correlation function, which for a homogeneous system is given as

$$g_N^{(n)}(\mathbf{r}^n) = \frac{\rho_N^{(n)}(\mathbf{r}^n)}{\rho^n} . \tag{2.88}$$

Since the absolute positions of the particles is irrelevant for homogeneous systems, it is worthwhile to consider a pair correlation function $g_2(\mathbf{r}_1, \mathbf{r}_2)$ that describes the conditional probability of finding a particle at position $\mathbf{r}_2$ given a particle located at $\mathbf{r}_1$. This is given as

$$g_2(\mathbf{r}_2 - \mathbf{r}_1) = \frac{1}{V}\int_V g_N^{(2)}(\mathbf{r}_1, \mathbf{r}_2) d\mathbf{r}_1 = \frac{1}{V}\sum_{i=1}^{N}\sum_{\substack{j=1 \\ j\neq i}} \delta(\mathbf{r} - [\mathbf{R}_j - \mathbf{R}_i]) \,. \tag{2.89}$$

The structure factor $S(\boldsymbol{q})$ can be defined using this pair correlation function and is essentially its Fourier transformation [63]

$$\tilde{S}(\boldsymbol{q}) = 1 + \rho \int_{\mathbb{R}^D} [g(\mathbf{r}) - 1] e^{-\mathrm{i}\boldsymbol{q}\cdot\mathbf{r}} \mathrm{d}\mathbf{r} \,, \tag{2.90}$$

$$g(\mathbf{r}) = g_2(\mathbf{r}) = 1 + \frac{1}{(2\pi)^D \rho} \int_{\mathbb{R}^D} \left[\tilde{S}(\boldsymbol{q}) - 1\right] e^{\mathrm{i}\boldsymbol{q}\cdot\mathbf{r}} \mathrm{d}\boldsymbol{q} \,, \tag{2.91}$$

where the quantities are scaled in order to keep them unitless and square-integrable. An alternative and more intuitive definition of $\tilde{S}(\boldsymbol{q})$ can be obtained by introducing the complex collective density variable $\tilde{\rho}(\boldsymbol{q})$, which is simply the Fourier transform of the local number density from Eq. 2.86:

$$\tilde{\rho}(\boldsymbol{q}) = \sum_{i=1}^{N} e^{-\mathrm{i}\boldsymbol{q}\cdot\mathbf{R}_i} \,, \tag{2.92}$$

which obeys the Hermitian symmetry $\tilde{\rho}(-\boldsymbol{q}) = \overline{\tilde{\rho}(\boldsymbol{q})}$. This quantity enables us to determine the scattering-intensity function that is similar to the PSD defined for the textured interface in Eq. 2.83 and is defined as

$$\tilde{S}(\boldsymbol{q}) = \frac{\tilde{\rho}(\boldsymbol{q})\overline{\tilde{\rho}(\boldsymbol{q})}}{N} \,, \tag{2.93}$$

$$= \frac{1}{N}\left|\sum_{i}^{N} e^{-\mathrm{i}\boldsymbol{q}\cdot R_i}\right|^2 \,, \tag{2.94}$$

which is a non-negative real function with inversion-symmetry $\tilde{S}(\boldsymbol{q}) = \tilde{S}(-\boldsymbol{q})$ with bounds $0 \leq \tilde{S}(\boldsymbol{q}) \leq N$ for $q \neq 0$ such that $\tilde{S}(\mathbf{0}) = N$. At this level, the vector $\boldsymbol{q}$ indicates some spatial frequency. Later, when we consider the scattering of light at the metasurface and assume the lowest order Born approximation, the vector $\boldsymbol{q}$ is called the scattering vector since it connects the wave vectors of the incident and the scattered field as $\boldsymbol{q} = \mathbf{k}_{\text{scat}} - \mathbf{k}_{\text{inc}}$. Figure 2.6 illustrates the angular-averaged structure factor obtained using Eq. 2.94 for four particle distributions. The color of each particle distribution corresponds to its structure factor shown with the same color. The particle density is kept constant for each system. This is done to have comparable features for these systems in the reciprocal space. The blue color shows a periodic square lattice of lattice constant a with a well-defined sharp peak in the structure factor at $q = 2\pi/a$. The orange color shows a perturbed square lattice where a uniform and uncorrelated perturbation is given to each particle of the system shown in blue. The disorder in this system is then responsible for the noise observed in its

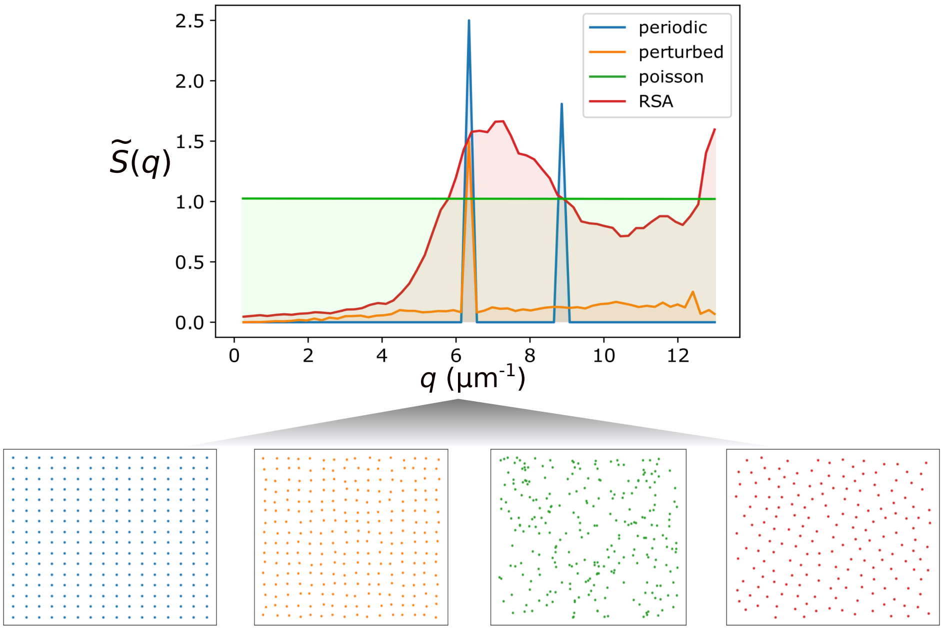

Figure 2.6: Illustration of four generic disordered particle arrangements and their corresponding angular averaged structure factor $\tilde{S}(q)$. The point distributions shown are in real space while the angular-average quantity shown is in reciprocal space.

structure factor. The green color corresponds to a typical Poissonian disordered system where the position of each particle is uncorrelated. The structure factor for such a system is unity at all length-scales for $N \rightarrow \infty$. The red color features a particle distribution obtained using a Random Sequential Adsorption (RSA) process where the particles are spatially distributed in a manner that is governed by their interaction potential. Such systems and their representative features are discussed in detail in Chap. 4 and Chap. 5.

Collective coordinate method

Similar to the process of generating textured interfaces from a desired Power Spectral Density $\tilde{P}(q)$ as described in Sec. 2.4.1, it is also possible to generate a point pattern for the optical scatterers based on a given structure factor $\tilde{S}(\boldsymbol{q})$. The Collective Coordinate Method (CCM) tackles this problem by seeking a finite number of particle coordinates contained in a finite-sized simulation domain with periodic boundaries such that the corresponding structure factor takes a desired form. While such an approach is unnecessary for disordered configurations that are only perturbative in nature (like perturbed or defect lattices), non-intuitive disordered configurations with a prescribed structure factor can readily be obtained using this technique through an optimization process [64]. Because the objective here is to prescribe a $\tilde{S}(\boldsymbol{q})$ for an optimal arrangement of a many-particle disordered configuration, this problem can be regarded as an inverse problem. Its counterpart in real space, where the pair correlation function is tailored for a many-particle system, has gained wider attention in the recent years [65, 66]. The direct computation of the structure factor with Eq. 2.94 from the positions of the particles allows continuously differentiable analytic expressions that are desirable for large-scale gradient-based optimization methods like Broyden-Fletcher-Goldfarb-Shanno algorithm and its memory limited variant [67, 68]. Since the disordered systems considered typically have hundreds to thousands particles, utilizing the gradient information to determine a search direction for optimization is a much more efficient way for searching the parameter space. For the structure factor defined in Eq. 2.94, we can write its derivative for a given microstate (single realization) with respect to the particle coordinates as:

$$\frac{d\tilde{S}(\boldsymbol{q})}{d\mathbf{R}_i} = \frac{1}{N}\left(\overline{\tilde{\rho}(\boldsymbol{q})}\frac{d\tilde{\rho}(\boldsymbol{q})}{d\mathbf{R}_i} + \tilde{\rho}(\boldsymbol{q})\frac{d\overline{\tilde{\rho}(\boldsymbol{q})}}{d\mathbf{R}_i}\right) \tag{2.95}$$

$$= -\frac{2\boldsymbol{q}}{N}\left(\frac{\tilde{\rho}(\boldsymbol{q})e^{\mathrm{i}\boldsymbol{q}\cdot\mathbf{R}_i} + \overline{\tilde{\rho}(\boldsymbol{q})e^{\mathrm{i}\boldsymbol{q}\cdot\mathbf{R}_i}}}{2i}\right) \tag{2.96}$$

$$= -\frac{2\boldsymbol{q}}{N}\Im\{\tilde{\rho}(\boldsymbol{q})e^{\mathrm{i}\boldsymbol{q}\cdot\mathbf{R}_i}\}\,. \tag{2.97}$$

We consider these N identical point particles inside a two-dimensional box of volume V to be interacting through a pairwise additive potentials $v(\mathbf{r})$ that is bounded and integrable such that its Fourier transform $\tilde{v}(\boldsymbol{q})$ exists. An objective function of the form $\Phi = \Phi_s + \Phi_g$ can be written such that,

$$\Phi_s(\mathbf{R}^N) = \sum_{\boldsymbol{q}} \tilde{v}(\boldsymbol{q})\left[\tilde{S}(\boldsymbol{q}) - \tilde{S}_0(\boldsymbol{q})\right]^2\,, \tag{2.98}$$

$$\Phi_g(\mathbf{R}^N) = \sum_{\mathbf{r}} w(\mathbf{r})\left[g(\mathbf{r}) - g_0(\mathbf{r})\right]^2\,, \tag{2.99}$$

where minimization of $\Phi_s(\mathbf{R}^N)$ and $\Phi_g(\mathbf{R}^N)$ would enforce that the optimal configuration $\mathbf{R}^N_{\text{opt}} \equiv \mathbf{R}_{1,\text{opt}}, \mathbf{R}_{2,\text{opt}}, \ldots, \mathbf{R}_{N,\text{opt}}$ has the target structure factor $\tilde{S}_0(\boldsymbol{q})$ and a target pair correlation $g_0(\mathbf{r})$ in regions where $\tilde{v}(\boldsymbol{q})$ and $w(\mathbf{r})$ are non-zero. The physical reason for an additive term Φ_g in the objective function can be understood if a particle distribution is needed which not only has a desired structure factor but also has no aggregating or overlapping particles. This information lies in the pair correlation function and can be enforced by setting $g_0(\mathbf{r}) = 0$ and $w(\mathbf{r}) = \max(0, 1 - |\mathbf{r}|/R_0)$ to maintain a minimum distance R_0 between the particles throughout the optimization. Given Φ_s and Φ_g are scalar functions, the derivative of the overall objective function Φ with respect to the particle positions can then be written as

$$\frac{d\Phi}{d\mathbf{R}^N} = -\frac{4}{N}\Im\left\{\sum_{\boldsymbol{q}} \boldsymbol{q}\tilde{F}(\boldsymbol{q})\tilde{\rho}(\boldsymbol{q})e^{\mathrm{i}\boldsymbol{q}\cdot\mathbf{R}_i}\right\}\,, \tag{2.100}$$

where the function $\tilde{F}(\boldsymbol{q})$ is given by [69]:

$$\tilde{F}(\boldsymbol{q}) = \tilde{v}(\boldsymbol{q})\left[\tilde{S}(\boldsymbol{q}) - \tilde{S}_0(\boldsymbol{q})\right] + \frac{1}{(2\pi)^D\rho}\int_{\mathbb{R}^D} w(\mathbf{r})\left[g(\mathbf{r}) - g_0(\mathbf{r})\right] e^{\mathrm{i}\boldsymbol{q}\cdot\mathbf{r}}d\mathbf{r}\,. \tag{2.101}$$

Here $g(\mathbf{r})$ is computed with the discrete Fourier transformation using Eq. 2.91. These gradients can be passed to the gradient optimizer for determining the search direction in the parameter space. With the algorithm just presented, it is possible to identify particles distributions that show particularly interesting statistical and optical properties. We shall exploit this method in Chap. 4 and Chap. 5 for designing a disordered metasurface for a solar cell.

Stealthy Hyperuniformity and ground states

Considering the same system of N identical point particles in a volume V interacting through a pairwise additive potentials $v(\mathbf{r})$, a special case can be achieved by disregarding the target structure factor $\tilde{S}_0(\boldsymbol{q})$ and considering an overall potential energy for these particles similar to Φ:

$$U(\mathbf{R}^N) = \frac{1}{2V} \sum_{\boldsymbol{q}} \tilde{v}(\boldsymbol{q}) [\tilde{\rho}(\boldsymbol{q}) \tilde{\rho}(-\boldsymbol{q}) - N] \,, \tag{2.102}$$

$$= \frac{1}{2V} \sum_{\boldsymbol{q}} \tilde{v}(\boldsymbol{q}) [\tilde{S}(\boldsymbol{q}) - \tilde{S}(\mathbf{0})] \,, \tag{2.103}$$

where $\tilde{\rho}(\boldsymbol{q})$ is the complex collective density variable defined for the point distribution in Eq. 2.92. It can be seen that if $\tilde{v}(\boldsymbol{q})$ is non-zero in the interval $0 \leq |\boldsymbol{q}| \leq |\boldsymbol{Q}|$, by minimizing U in this region, the particles can be arranged in a disordered manner such that $\tilde{S}(\boldsymbol{q})$ is driven to its minimum value of zero (except at $\tilde{S}(\mathbf{0}) = N$). In such a case where U becomes zero due to the structure factor being zero, the disordered system achieves its ground state or global energy minimum. Such disordered ground-state configurations are referred to as "Stealthy Hyperuniform systems" because the scattering pattern is zero in this region thus implying that the system will completely suppress single scattering of incident radiation for the given wave vectors and are therefore transparent at the corresponding wavelengths [70, 71].

Hyperuniformity

A less stringent constraint of $\tilde{S}(\boldsymbol{q}) = 0$ in a finite region around $\boldsymbol{q} = \mathbf{0}$ can also be obtained by a particle configuration such that the structure factor instead vanishes for smaller $\boldsymbol{q}$,

$$\lim_{|q| \to 0} S(\boldsymbol{q}) = 0 \,. \tag{2.104}$$

In terms of its real space characteristics, the mean-squared number of particle fluctuation $\sigma_N^2(R)$ in a window of size R increases less rapidly than R^d where d is the space dimension, thus exhibiting uniformity in its particle distribution at large length scales. For the pertinent two-dimensional patterns and an arbitrary domain shape, this generalizes to a condition in the asymptotic limit towards very large surfaces [71]:

$$\lim_{R \to \infty} \frac{\sigma_N^2(R)}{R^2} = 0 \,. \tag{2.105}$$

Such configurations are called 'Hyperuniform states' as such systems do not possess infinite-wavelength fluctuations. Clearly, points arranged on a regular periodic lattice trivially meet this criteria and are, therefore, hyperuniform. The particle number fluctuations of regular periodic lattice are concentrated only near the window boundary thus only having a surface-area scaling $\sigma_N^2(R) \propto R^{d-1}$. In fact, it can be shown that for any statistically homogeneous and isotropic point pattern, $\sigma_N^2(R)$ cannot grow more slowly than the surface of the window [72]. Disordered configurations less trivially can also meet this criteria and can possess near surface-area scaling as perfect crystals. These systems along with its 'stealthy' counterpart can easily be generated using the CCM. The novelty of such particle distributions along with their unique scattering properties, particularly in the context of light-trapping in solar cells, are a major subject of this thesis and are discussed in detail in Chap. 4.

2.5 Numerical methods

Throughout the thesis, we investigate light-trapping structures that have critical features comparable or smaller than the incident wavelength and whose scattering response is not necessarily analytic. For such cases, Maxwell's equations need to be numerically solved in its full glory to understand the light propagation through the considered composite system. In this section, we describe the finite-difference frequency-domain (FDFD) and finite-difference time-domain (FDTD) methods for obtaining the solutions to the Maxwell's equations in both time and frequency domain. Both methods will be used in later chapters of the thesis.

2.5.1 Finite-difference frequency-domain method

The finite-difference frequency-domain (FDFD) method is a simple yet powerful technique for numerically solving Maxwell's equations in frequency-domain on a discrete spatial grid. This grid is based on Yee's cell that was originally developed for its time-domain counterpart [73]. The Yee's grid allows to approximate the continuous derivatives of the electric and magnetic fields by two-point central differences that are second-order accurate.

From the wave equation expressed in Eq. 2.26, one can obtain the electric field at discrete points in space for a user-specified frequency. This is done by realising that Eq. 2.26 is essentially of the form $\boldsymbol{Ax} = \boldsymbol{b}$ where $\boldsymbol{A} \in \mathbb{R}^{n\times n}$ is the system matrix such that $\boldsymbol{A} = \boldsymbol{\nabla} \times \boldsymbol{\nabla} \times -\omega^2\mu_0\varepsilon_0\mu_r(\omega)\varepsilon_r(\mathbf{r},\omega)$, $\boldsymbol{b} \in \mathbb{R}^n$ is the solution field vector such that $\boldsymbol{x} = \tilde{\mathbf{E}}(\mathbf{r},\omega)$ and $\boldsymbol{b} \in \mathbb{R}^n$ are the sources such that $\boldsymbol{b} = i\omega\mu_0\mu_r(\omega)\tilde{\mathbf{J}}(\mathbf{r},\omega)$. Equation 2.26 is solved using a direct solver like LU or Cholesky decomposition, iterative (Richardson or Jacobi methods) or through least-squares method for ill-conditioned matrices. We use a custom-built two-dimensional FDFD code for simulating the optical response from a thin-film solar when modified with a textured interface or an inhomogeneous material designed using Transformation Optics. Through this, we determined the scattered field as well as the absorbed energy in the semiconductor layer for each frequency of interest.

2.5.2 Finite-difference time-domain method

For most applications, the finite-difference time-domain (FDTD) method serves as the most widely used technique for numerically solving Maxwell's equations. The field solutions are obtained in space that on a discrete grid, compatible to its frequency domain counterpart. However, the fields are also discretized in the time domain here. This way, the differential equations for the electric and magnetic fields are transformed into algebraic equations using finite-differences such that the fields are evolved in time using discrete time steps. For this, the electromagnetic field components are staggered at different spatial and temporal locations in a unit-cell of the Yee grid [73]. The electric field components are spatially placed along the edges of such a cell while the orthogonal magnetic field components are placed at the centers of the cell faces. A leapfrog updating scheme in the time-domain evolves the field components for each discrete time step [74].

The simulations using the FDTD method in this thesis were done using the open-source software Meep [75]. The main motivation for using FDTD came from simulating large-scale disordered systems where the information of long-range interactions need to be effectively captured. A computational tool like FDTD is then useful as it captures the system's spectral response to a Gaussian pulse illumination in a single simulation. The scattered and transmitted fields recorded in the time-domain are converted to frequency-domain through a discrete Fourier transformation to get the desired spectral response of the composite system. Moreover, the computation is memory efficient and can easily be parallelized, making it an ideal tool for large scale optical simulations. This is in contrast to other frequency-domain methods like FDFD or Finite Element Method (FEM), where such a system must be simulation each time for a different frequency.

3 Light trapping in solar cells: A transformation optics approach

This chapter describes how transformation optics (TrO) can be used in designing light trapping structures for thin-film solar cells. The design strategy for such structures draws inspiration from solar cells with textured interfaces with a directly patterned absorbing layer. We show that it is possible to conformally map the nanopatterned texture onto a planar equivalent and use the TrO to obtain a planar, inhomogeneous, dielectric-only material whose optical functionality is comparable to its textured counterpart. Thanks to the planar interface, the resulting solar cell is expected to have much improved electrical performance. After introduction in Sec. 3.1, Sec. 3.2 describes geometrical details of the simulation setup for the light trapping structures considered here. Section. 3.3, investigates the use of Schwarz-Christoffel mappings defined in Sec. 2.2.2 for obtaining an inhomogeneous dielectric-only material from a given textured profile. These structures are put on top of a thin flim solar cell, and the optical properties of the periodic and disordered structures are discussed in Sec. 3.4 and Sec. 3.5 in comparison to their textured counterpart. Section 3.6 discusses the effect of an additional optical interface in the system by treating the interface incoherently and accounting for the multiple reflections from it. The effect of limiting the refractive index bounds for the inhomogeneous material and its impact on the optical properties of the overall system is finally explored in Sec. 3.7. The contents of this chapter is mainly based on [P1].

3.1 Introduction

Achieving high-efficiency solar cells relies heavily on employing effective light trapping techniques. This becomes especially critical when dealing with solar cells that are less than 100 µm thick, as a thin absorber alone cannot efficiently capture incident solar radiation, as previously explained in Sec. 2.3.2. For thin c-Si solar cells with thicknesses less than 50 µm, researchers have proposed light trapping designs aimed at improving light incoupling and enhancing light scattering within the absorber layer. These designs involve periodic or disordered nanostructures [16, 76–82], or the enhancement of resonant coupling to guided modes [83–85]. Most of these approaches require direct nanostructuring of the front and/or back interfaces of the absorbing layer. However, a drawback of nanostructuring is that it unavoidably increases the interface area, leading to a higher density of electronic defect sites per unit area. Additionally, the texturing process itself often introduces a significant number of additional defect sites [12]. Consequently, surface recombination of minority charge carriers increases, and the anticipated enhancement in electron-hole pair generation due to increased absorption from texturing is hindered by poor electrical performance [12, 86–88]. To provide an alternative solution to this issue, this work focuses on preserving the electrical performance of the unpatterned solar cell while achieving superior optical response through the application of principles from TrO described in Sec. 2.2. The core concept behind this proposed approach involves incorporating a nanotextured pattern on the light-absorbing layer, which enhances light trapping. Subsequently, this nanotextured interface is mapped onto a planar interface while simultaneously transforming the dielectric space above it.

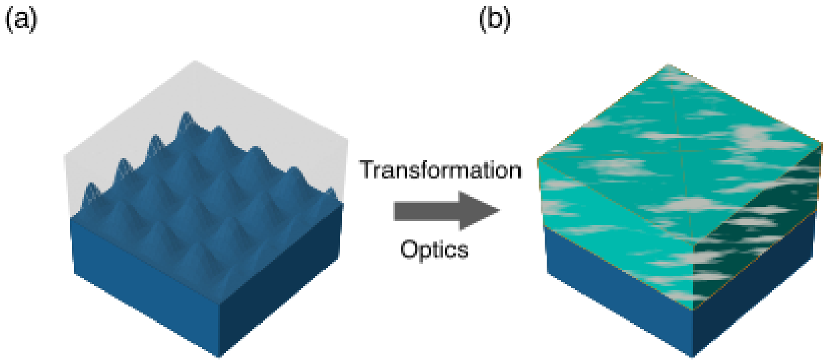

Figure 3.1: Schematic diagram of the proposed idea for mapping (a) a nanostructured surface to (b) an optically equivalent planar layer but with an inhomogeneous refractive index. Adapted from Ref. [P1] with permission from © Optica Publishing Group.

Figure 3.1 illustrates this concept, where the upper half-space of a nanostructured interface (shown on the left with a grey region) is mapped to a planar layer with an inhomogeneous (but smoothly varying) refractive index distribution (shown on the right with color gradient), which is directly applied on top of an unpatterned planar solar cell. The resulting structure is expected to have similar optical properties when compared to the nanostructured interface, but now on top of the light-absorbing layer with planar interfaces. This renders the final device superior concerning its electrical properties.

In the context of solar cells, TrO has found application in cloaking the electrical contact fingers on a solar cell [89, 90]. Furthermore, TrO has been employed to achieve the complete elimination of Fresnel reflection, a technique demonstrated in the context of light-emitting diodes (LEDs). Due to light reciprocity, this approach has the potential to also enhance light incoupling into solar cells [91]. However, it is important to note that while such a device acts as a perfect out-coupler, it does not take full advantage of the absorption that can occur over multiple passes of light. Consequently, it may not be the most optimal choice for thin solar cells. With our proposed approach for light trapping and light management in solar cells, we introduce a novel application for TrO. We first discuss the specifics of the structures that were developed and assess their functionality within a standard solar cell system. Initially, we consider modulated interfaces to illustrate our design approach, and later, we examine selected nanotextured interfaces. To validate the effectiveness of these devices, we conduct comprehensive full-wave optical simulations and compare their performance to reference structures that include the actual nanotextured interface, as well as other reference structures designed for light management. This comparative analysis allows us to gauge the improvements achieved through our approach.

3.2 Cell design and simulation

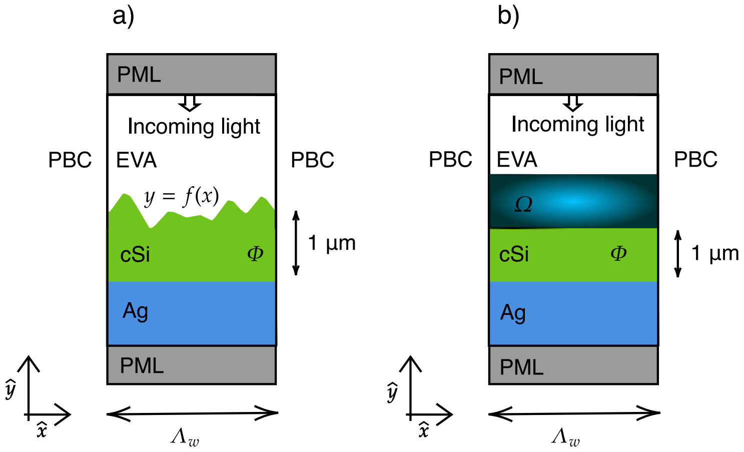

Figure 3.2: Illustration of the computation setup. (a) Textured absorbing layer with perfectly matched layers (PML) and periodic boundary conditions. (b) Desired geometry with inhomogeneous, non-absorbing design domain Ω obtained by mapping Γ to Ω.

To analyze the light trapping characteristics of the nanostructured and transformed systems to be obtained from TrO, we consider a simplified solar cell configuration consisting of a 1 µm thick c-Si layer equipped with a silver (Ag) back-reflector. Figure 3.2(a) shows the actual reference structure and Fig. 3.2(b) its planarized counterpart obtained using our proposed approach. We have chosen a 1 µm thick c-Si cell for our study to enable a more comprehensive examination of absorption enhancement due to the light trapping effect of the textured interface. For significantly thicker solar cells, the impact of light trapping tends to be less pronounced. The presence of a metal back-reflector serves the purpose of reflecting light that the c-Si layer has not absorbed during a single pass. The dispersive permittivities of these materials are taken from literature [92, 93].

The space above the light absorber is considered semi-infinite and filled with ethylene-vinyl acetate (EVA) thus indicating a standard encapsulated solar cell configuration. To perform simulations, we employ an in-house Finite-Difference Frequency-Domain (FDFD) code for TE polarization at normal incidence, with a spatial resolution of 4 nm. We apply periodic boundary conditions along the transverse direction and perfectly matched layers (PML) along the longitudinal direction to effectively model the behavior of light in this solar cell structure.

Using TrO, the inhomogeneous refractive index is determined for the design region Ω placed above the planar c-Si layer. The spatially dependent electric field distribution from the simulation is used for calculating the global absorption in c-Si using Eq. 2.37. This is done by integrating the local absorption across the spatial extent of the absorbing layer (textured or planar) for each wavelength of interest. This is given by

$$A_{\text{total}}(\lambda) = \frac{\omega}{2}\epsilon_0 \Im(\epsilon(\lambda)) \int_{\Phi} |E_z(\mathbf{r},\lambda)|^2 \, \mathrm{d}V \,, \tag{3.1}$$

where $\omega = \frac{2\pi c}{\lambda}$ is the frequency of incident light. This absorption is calculated from $\lambda_1 = 300$ nm to $\lambda_2 = 1100$ nm in steps of 2 nm for periodic structures and 10 nm for disordered structures. The spectral region chosen here is justified in Sec. 2.3 as the solar irradiance is highest here. For different textures in consideration, the volume of the absorbing layer is always kept constant to eliminate any trivial absorption gain.

3.3 Schwarz-Christoffel mapping for light trapping structures

Section 2.2.2 showed that to obtain an isotropic medium from a coordinate transformation, the coordinate transformations must be conformal. We introduced Schwarz-Christoffel (SC) transformations as a method to generate conformal maps in a straightforward algorithmic manner. Our goal is to use SC transformation for mapping the semi-infinite half-space above the nanostructured light-absorbing layer of the solar cell to a planar interface. Since many variants of the basic SC map are possible, we restrict ourselves to ones that map the complex upper half-space H^+, here on referred to as "physical space", to the interiors of a polygon W, here on referred to as "virtual space".

The virtual space W is the region defined by a collection of complex vertices $w_1, w_2, \ldots, w_n$. The pre-images of these vertices, or the prevertices, given by $z_1, z_2, \ldots, z_n$ are defined in the physical space where such that $z = f^{-1}(w)$. In our context, the complex vertices in the virtual space are specified by the textured interface. For a one-dimensional textured profile in the xy-plane, the real and imaginary parts of these complex vertices would simply the x and y coordinates, respectively. For this work, we therefore only consider one-dimensional textures and their corresponding transformations.

Since we aim to map the space above the textured interface, it is essential to have one of the vertices w_j to be at infinity. For this open polygon W to map to the upper half-space H^+, this implies that it's prevertex $z_j = f^{-1}(w_j)$ must also be at infinity. By choosing the entire upper half-space as the target, the prevertices z_i in the physical domain would be real. This is crucial for our problem as this would ultimately impose the inhomogeneous refractive index arriving from the SC transformation to be planarized for putting on top of an unpatterned absorbing layer. The resulting SC transformation then also ensures that the optical path length between two arbitrarily chosen points z_1 and z_2 in the physical space is equal to the optical path length between points $f(z_1)$ and $f(z_2)$ in the virtual space above the textured interface [47].

To account for the periodicity of the texture, we scale the prevertices of a periodic unit cell Λ_w in the virtual space using the complex constant C from Eq. 2.74. This scaling ensures that these prevertices effectively map to the same length of a periodic unit cell in the physical space, denoted as Λ_z (the region obtained as a result of mapping the virtual space). By doing so, we preserve the periodicity of the structure, ensuring that identical diffractive features in both structures. These mappings are numerically generated using the MATLAB SC Toolbox [53]. Since the software package used does not directly support periodic boundary conditions, we employ a workaround. We transform a larger super-periodic structure consisting of multiple unit cells. Subsequently, we apply the scaling of the SC map over this larger structure to maintain a similar level of periodicity. Finally, for optical simulations, we only consider the central spatial domain of this super-periodic structure, applying periodic boundary conditions. To assess the accuracy of this scaling procedure, we introduce a normalized error function that depends on the number of periodic unit cells N. This error function is defined as:

$$\delta(N) = \frac{|\Lambda_z - \Lambda_w|}{\Lambda_w} \; \forall \, z \in \Omega \mid f(z) \in \Gamma, \tag{3.2}$$

where Ω is the design region in physical space and Γ is the region in the virtual space. For our analysis, values that satisfy the equation $\log_{10}(\delta) \leq -2$ obtained for $N \geq 15$ for periodic structures and $N \geq 7$ for disordered structures were found to be sufficient to avoid edge-effects from the maps while still retaining the accuracy of the obtained maps [52].

It is crucial to emphasize that our approach does not aim to map the entire space (above and below the textured interface) but specifically focuses on the region above the textured interface. For mapping both the upper and the lower half-space of the interface, the coordinate transformation must fully describe the interaction of the electromagnetic fields at the interface of two media for all the wavelengths. In simple words, the coordinate transformation must account for the scattering due to the interface, something that is non-trivial for a corrugated interface, let alone be conformal. Consequently, the transformed structure will not precisely replicate the optical response of the original one. However, by preserving the optical path length in the virtual space and its corresponding points in physical space, we obtain a spatially inhomogeneous material distribution in physical space that yields similar diffractive features as those associated with the original textured interface. In light of these considerations, we prefer to describe our approach as "transformation optics-inspired" within the context of light trapping. The structures resulting from this approach continue to fulfill their intended purpose within our discussion.

For TE polarization, the material in the Cartesian space are assumed to be non-magnetic ($\epsilon_z, \mu_x = 1, \mu_y = 1$). Therefore, the only parameter getting influenced by the SC-map is the is the refractive index ($\mu = 1$ and $n = \sqrt{\epsilon_z}$). For a mapping defined from the space above the corrugated texture to the upper half-space (planar geometry), the refractive index needed in the physical space is:

$$n'(x', y') = n_0 \left| \frac{dw}{dz} \right| , \tag{3.3}$$

with n_0, the refractive index of the untransformed dielectric half-space [44]. For our purpose, n_0 is chosen to be the refractive index of Ethyl-vinyl Acetate (EVA), which is the common encapsulant for the solar cell when building a solar module. For simplicity, EVA is taken to be non-dispersive in the wavelength range of interest with value $n_0 = 1.5$. This way, we restrict ourselves to only dielectric materials for the designed structure.

It may be surprising that Eq. 3.3 looks different than Eq. 2.72 obtained in Sec. 2.2. This is because the medium in Eq. 2.72 is defined in the virtual space whereas Eq. 3.3 defines the medium in the physical space. We chose the later for our study since the goal is to have a medium that is ultimately planar. In the following subsections, we numerically generate such structures for a periodic texture. At a later stage, we extend our analysis to encompass arbitrary profiles resembling textured interfaces. However, the methodology employed to study these intricate textures will closely parallel that used for the periodic interface.

3.3.1 Periodic texture

To demonstrate the applicability of our approach, we initially examine a sinusoidal interface between a c-Si layer and a dielectric half-space (EVA). In Fig. 3.3(a), we show the mapping in the virtual space (w-space). In this mapping, the upper half of the complex plane is transformed into the open polygon defined by the space above the sinusoidal

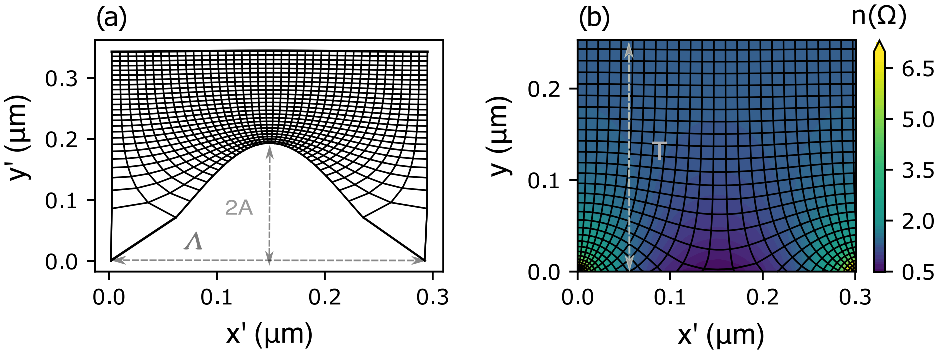

Figure 3.3: (a) Spatial grid for the virtual space (w-space) generated by mapping the complex upper half-space onto an open polygon with a sinusoidal texture with lattice period $\Lambda_w = 0.3$ µm and a height of $H = 2A = 0.2$ µm. (b) Refractive index and its overlaid spatial grid in the physical space (z-space). The overlaid grid is obtained using inverse transformation. The domain is longitudinally extended till $T = 0.25$ µm. Adapted from Ref. [P1] with permission from © Optica Publishing Group.

texture. The texture has a lattice period of $\Lambda_w = 0.3$ µm and a height of $H = 2A = 0.2$ µm, where A represents the modulation amplitude. The desired refractive index distribution in the physical space for our planar system is then obtained using Eq. 3.3 and shown in Fig. 3.3(b). The curved grid lines within this sub-figure illustrate the mapping in the physical space. This mapping results from an inverse transformation that maps an overlaid Cartesian grid situated above the textured interface (a region containing homogeneous material) to the complex upper half-space depicted in this sub-figure of the physical space.

The SC mapping applies to the entire upper half-space. However, for computational purposes, we must consider a finite domain characterized by a sufficient longitudinal length denoted as T. In this domain, the refractive index distribution must transform. The spatial extent is carefully chosen so that the refractive index at the terminating interface, which interfaces with the surroundings, closely matches the refractive index of the untransformed homogeneous EVA layer. For our designed sinusoidal texture, this longitudinal length is constrained to $T = 0.25$ µm, and is adjusted depending on the properties of the texture under consideration.

Although the derived refractive index in the physical space spans a range of $\mathrm{n}(\Omega) = [0.5, 81]$, for practical feasibility, this range is truncated to the limits $\mathrm{n}(\Omega) = [1, 3.5]$. It is important to note that the lower limit is allowed to be less than the refractive index of the EVA layer. This choice is influenced by the available dielectric materials and the finite parameter range they offer. This restricted range for the inhomogeneous refractive index distribution is maintained consistently throughout the work. The curved grid lines in the z-space from inverse transformation and its resulting refractive index distribution, as shown in Fig. 3.3(b), can intuitively be understood as:

- Dilation in space as a result of 'flattening' of the central bump. This gives rise to the central region ($x = 0.15$ µm) having sub-unity refractive indices.
- Consequential compression of space in the surrounding region of the dilated space to maintain conformality of the map. This leads to peripheral regions ($x = 0$ µm and $x = 0.3$ µm) having very high refractive index.

3.3.2 Disordered case

Building upon the approach employed for the sinusoidal texture, we now explore a disordered texture designed to yield a strongly scattering response and a broader enhancement in absorption. This disordered texture is characterized by its root mean square (RMS) roughness σ, and a lateral correlation length ζ.

Figure 3.4 shows a textured interface with correlation length $\zeta = 0.15$ µm and RMS height $\sigma = 0.2$ µm in the top figure. We chose the texture profile to be described using Eq. 2.85 due to its differentiability at any point on the profile. Such a condition ensures the disordered texture profile $h(x)$ to be continuous and smooth varying, as opposed to discontinuous and needle-like features. The resulting conformal maps would not have extremely large

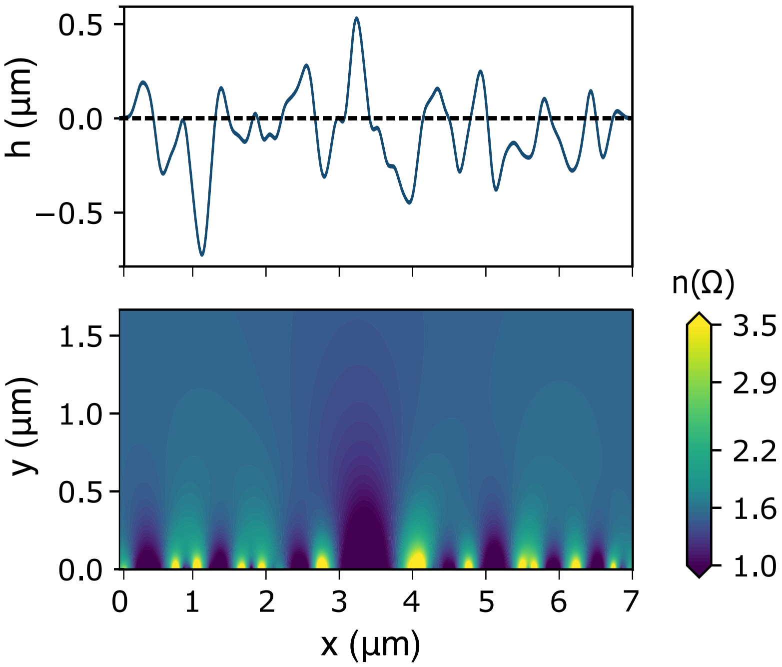

Figure 3.4: Textured interface with correlation length $\zeta = 0.15$ µm and RMS height $\sigma = 0.2$ µm and its resulting refractive index distribution in physical space after transformation. Adapted from Ref. [P1] with permission from © Optica Publishing Group.

derivatives ultimately, avoiding extreme values of refractive index in the physical space.

The derived refractive index distribution in the physical space for such a disordered texture is shown in Fig. 3.4 as the bottom figure. By direct comparison of the texture and the corresponding $n(\Omega)$, it can be seen that $n(\Omega)$ contains high refractive index regions at the same locations where $h(x) < 0$ µm. Likewise, $n(\Omega)$ contains low refractive index regions at same locations where $h(x) > 0$ µm. This observation is similar to the one described for the sinusoidal texture. Moreover, the height and width of such regions in $n(\Omega)$ can be directly compared to the height and width of the texture at that lateral location. This way, the information contained in the disorder can be fully characterized by such a refractive index distribution in the physical space.

For optical simulations with periodic boundaries, we consider a super-periodic structure for the textured interface characterized by a spatial extent denoted as Λ. In this structure, modulations appear at spatial frequencies that are integer multiples of $k_0 = 2\pi/\Lambda$. The spatial extent of one lattice period of the textured interface is taken to be in the range of 12 µm and 15 µm. Choosing such a large lattice period in comparison to the typical correlation lengths in the range 0.05 µm $\leq \zeta \leq 0.3$ µm helps to mitigate potential artifacts arising from periodicity and ensures statistically stable results. Moreover, utilizing sufficiently large simulation domains allows us to use fewer periodic elements for the SC maps, thus reducing the computational overhead associated with transforming a super-periodic structure. To maintain proper periodicity in the simulation, the disordered texture is truncated within the simulation domain by applying a tapered cosine window function, as described in [94]:

$$w(x) = \begin{cases} \frac{1}{2}\left\{1 + \cos\left(\frac{2\pi}{r}(x - r/2)\right)\right\}\,, & 0 \le x < \frac{r}{2} \\ 1\,, & \frac{r}{2} \le x < 1 - \frac{r}{2} \\ \frac{1}{2}\left\{1 + \cos\left(\frac{2\pi}{r}(x - 1 + r/2)\right)\right\}\,. & 1 - \frac{r}{2} \le x \le 1 \end{cases} \tag{3.4}$$

Here, x ranges from 0 to 1, and r represents the shape factor of the window. This shape factor r determines the fraction of the window that falls within the tapered-cosine segment. In our simulations, we opted for a moderate value of $r = 0.2$. This choice allows us to preserve the characteristic disorder properties while avoiding the introduction of spurious resonant modes that can occur when using sharp tapering.

3.4 Optical response of the structures

3.4.1 Periodic

We consider a sinusoidally textured interface characterized by a lattice period of $\Lambda = 0.3$ µm and height $H = 2A = 0.2$ µm where A represents the modulation amplitude. After evaluating various modulation amplitudes, this particular lattice period was deemed optimal for maximizing the photocurrent J_{ph}. Figure 3.5(a) shows the numerically simulated absorption in the c-Si layer for three main structures: the textured interface, its counterpart obtained using TrO, and a reference structure featuring a planar interface but with a linear graded-index anti-reflective (AR) coating with a thickness of $T = 1$ µm. The thickness of this AR coating is deliberately set to be relatively large to ensure broadband anti-reflection. To facilitate a meaningful comparison with the TrO structure, the refractive index of this coating is kept in the range $[1.5, 3.5]$, ensuring impedance matching with the EVA layer. For completeness, we also show the spectrum of an unpatterned planar c-Si thin-film.

In the absence of any texture or inhomogeneous index layers (such as TrO or the gradient AR coating), the unpatterned c-Si absorbing layer acts as a Fabry-Perot cavity, obeying the corresponding resonance peaks in its absorbance spectrum. However, with the introduction of texturing or inhomogeneous layers, the short and long-wavelength ranges exhibit higher absorption compared to the planar structure.

For shorter wavelengths, where c-Si strongly absorbs light, the photons are absorbed before reaching the metal back contact. The enhanced in-coupling of light in this regime results in significant absorption enhancements. Notably, in this range, the gradient AR coating outperforms the sinusoidal texture in terms of in-coupling light effectively. Conversely, for wavelengths longer than 500 nm where 1 µm thick c-Si is weakly absorbing, the primary objective is to excite higher diffraction orders as they correspond to longer light path lengths within the absorbing material. In this scenario, the AR coating falls short

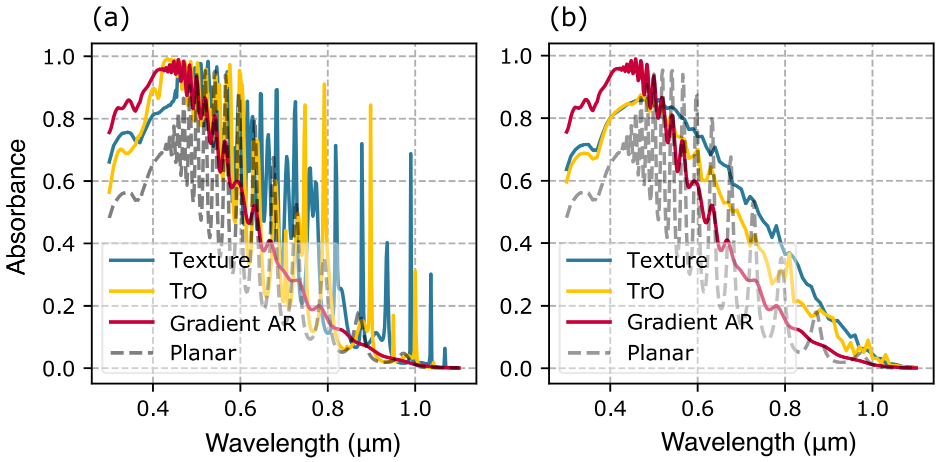

Figure 3.5: Absorption spectrum obtained using a periodic and disordered texture (blue) and its planar counterpart (yellow) derived using SC mapping are plotted. As reference spectra, the absorption of a planar c-Si wafer (grey) and a planar interface with additional linear graded index AR layer (red) are illustrated. (a) Sinusoidal texture with height $H = 2A = 0.2$ µm and lattice period $\Lambda = 0.3$ µm. (b) Disordered texture with RMS roughness $\sigma = 0.2$ µm and correlation length $\zeta = 0.15$ µm.

in efficiently scattering light into these diffraction orders, unlike the sinusoidal texture [95].

The TrO structure, as shown in Fig. 3.3(b), offers a favorable compromise between these two scenarios. It combines anti-reflective properties and light-scattering capabilities effectively. The TrO structure exhibits an anti-reflective effect for the wavelength range 0.3−0.4 µm due to its smooth variation in refractive index along both lateral and longitudinal directions. The scattering properties of the TrO structure are particularly notable in the weakly absorbing wavelength range spanning 0.45 − 0.6 µm. Here, the refractive index variation in the lateral direction facilitates the excitation of higher diffraction orders. However, for wavelengths longer than 0.6 − 1.1 µm, the lateral features in the TrO structure become less relevant to the incident light, effectively rendering it as an averaged medium. This behavior reduces the impedance mismatch between the EVA and the Silicon layer in this wavelength range.

3.4.2 Disordered structure

Figure 3.5(b) shows the absorption spectrum obtained for a planar c-Si structure employing the inhomogeneous layer derived from the SC mapping. This spectrum is compared to the absorption spectrum of the corresponding disordered texture, characterized by an RMS roughness of 0.2 µm and a correlation length of 0.15 µm. The selection of this correlation length was based on optimization, aiming to maximize the photocurrent while keeping the RMS roughness fixed. The absorption spectra presented in Fig. 3.5(b) for both geometries are averaged over the absorption spectra obtained from three surface realizations, each possessing nominally identical properties. This averaging helps provide a more representative and statistically reliable absorption profile for the respective structures.

Similar to the discussion for periodic structures, the gradient AR coating demonstrates superior performance over the disordered texture at shorter wavelengths, primarily due to its effective light in-coupling capabilities. However, for wavelengths longer than 500 nm, we observe the advantages of the disorder as it provides additional scattering channels, resulting in a more broadband absorption enhancement compared to the gradient AR coating and the periodic structure. The TrO structure derived from the disordered texture continues to strike a balance between the gradient AR coating and the texture, outperforming its periodic counterpart in this context. However, it is worth noting that the absorption spectrum for the TrO structure, as indicated by the orange curve in Fig. 3.5(b), exhibits less smearing of Fabry-Perot oscillation peaks compared to its disordered counterpart. This suggests that the TrO structure cannot fully exploit the broad Fourier spectrum offered by the disorder, likely due to some of the finer details of the disorder being partially washed out by the refractive index capping, as discussed earlier.

3.5 Photocurrent of the obtained devices

We calculate the photocurrent J_{ph} for each solar cell geometry using Eq. 2.75. For the global absorption calculated from simulations, and assuming the internal quantum efficiency $\eta_{\mathrm{IQE}} = 1$, the photocurrent current is given as

$$J_{\mathrm{ph}} = e \int_{\lambda_1}^{\lambda_2} \varphi(\lambda) A_{\mathrm{total}}(\lambda) \mathrm{d}\lambda \,, \tag{3.5}$$

where $\varphi(\lambda)$ is the AM1.5G solar irradiation spectrum. For simplicity, the internal quantum efficiency η_{IQE} is taken to be 1.

3.5.1 Periodic

Using Eq. 3.5, J_{ph} is calculated for the structures discussed above. The photocurrent is evaluated in the short (300-500 nm) and long (500-1100 nm) wavelength range and summarized in Table 3.1. We also add the total photocurrent resulting thereof for convenience to the table.

As discussed in Sec. 3.4.1, the AR action observed in both the textured structure and the TrO structure becomes apparent when examining their similar J_{ph} for 300-500 nm wavelength range. The gradient AR coating outperforms both of these structures in the 300-500 nm wavelength range, thus exhibiting a higher J_{ph}. This advantage, however, comes at a cost when considering the longer wavelength range of 500-1100 nm, where the importance of scattering into multiple channels becomes more pronounced.

J_{ph} (mA/cm^2)	Texture	TrO	Gradient AR	Planar
300-500 nm	5.48	5.67	5.87	4.29
500-1100 nm	14.10	12.13	10.31	9.14
300-1100 nm	19.58	17.80	16.18	13.43

Table 3.1: Comparison of photocurrent for sinusoidal texture of height $H = 0.2$ µm and lattice period $\Lambda = 0.3$ µm, TrO geometry and planar references. Each row corresponds to the photocurrent evaluated in a different spectral region.

J_{ph} (mA/cm^2)	Texture	TrO	Gradient AR	Planar
300-500 nm	5.02	4.97	5.87	4.29
500-1100 nm	16.02	13.69	10.31	9.14
300-1100 nm	21.04	18.66	16.18	13.43

Table 3.2: Comparison of photocurrent for a disordered texture of RMS roughness $\sigma = 0.2$ µm and correlation length $\zeta = 0.15$ µm, TrO geometry and planar references. Each row corresponds to the photocurrent evaluated in a different spectral region.

3.5.2 Disordered

Table 3.2 summarizes J_{ph} for the textured structure with fixed RMS roughness $\sigma = 0.2$ µm and correlation length $\zeta = 0.15$ µm in comparison with the other references. In line with the discussion in Section 3.5.1, it is evident that the TrO structure represents a decent trade-off between the textured interface and the gradient AR layer. It yields comparable J_{ph} values for the short wavelength range while achieving large J_{ph} values in comparison to the gradient AR layer for the longer wavelength range.

To fully understand the influence of spatial features on the resulting TrO structures and its optical performance, we generate texture profiles with varying RMS heights and correlation lengths. Their corresponding maps are generated and optically simulated using the same procedure highlighted above. Figures 3.6(a) and (b) show the averaged J_{ph} for the TrO and its textured counterpart as a function correlation length ζ and RMS roughness σ, respectively.

Figures 3.6(a) and (b) suggest that the TrO model can capture the stochastic nature of the disordered texture in its index distribution. While the TrO geometry follows a similar trend for J_{ph} as the texture, the discrepancy between the two geometries tends to increase on average for sharper features. This observation is not surprising, as sharper features in the texture correspond to more extreme refractive indices in the physical domain obtained from the SC map.

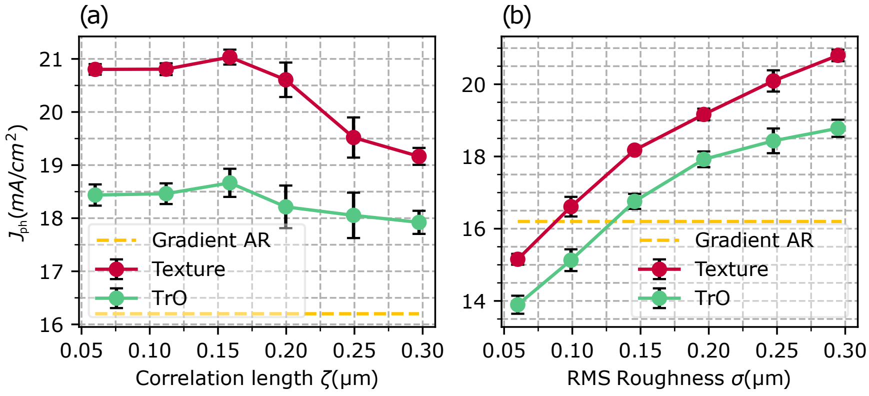

Figure 3.6: Comparison study of J_{ph} as a function of the correlation length and RMS height for a disordered structure. (a) RMS roughness $\sigma = 0.2$ μm. (b) Correlation length $\zeta = 0.3$ μm. The errorbars indicate the standard deviation of J_{ph} from the conducted trials.

As discussed earlier in Sec. 2.4.1, for shorter correlation lengths (here $\zeta < 0.15$ μm) while keeping a fixed RMS roughness ($\sigma = 0.2$ μm), the features of the texture become very sharp. In such scenarios, the incident light cannot spatially resolve either the texture or the spatial features in the inhomogeneous TrO layer. Consequently, the contribution to high J_{ph} values, as indicated in Fig. 3.6(a), primarily arises from the anti-reflective effects provided by these structures [76]. Additionally, due to the sharp features over small lateral lengths, the SC maps now, on average, encompass stronger derivatives in the physical space. This crucial information about the texture properties may end up being ignored in the simulation due to refractive index capping. This explains the larger discrepancy in the TrO geometry compared to the texture, even though the texture itself may not be optimal in these cases.

The discrepancy in J_{ph} between the texture and the TrO structure is further examined in Fig. 3.6(b), where the correlation length is fixed at a value which yields the minimum difference in J_{ph} between the two geometries ($\zeta = 0.3$ μm), but the RMS roughness of the texture is varied. For larger RMS roughness ($\sigma > 0.15$ μm), a saturation of the J_{ph} curves is observed. This saturation is due to optimal coupling to the diffraction pathways offered by both the texture and the TrO structure under consideration. Additionally, as the RMS roughness increases, more compression in the physical space is required to preserve the optical path length. This stronger compression, in turn, leads to a more extreme refractive index distribution. However, due to the effects of refractive index capping, this extreme distribution is not fully realized in the simulation. Consequently, a larger discrepancy between the texture and the TrO structure is observed for cases with higher RMS roughness.

Figure 3.7 summarizes the normalized photocurrent of nanostructures considered. The photocurrent J_{ph} is evaluated for the entire spectral range. These results are shown in comparison to the Lambertian limit for a one-dimensional textured interface for 1 μm thick c-Si layer. This limit is calculated using $A(\lambda) = \alpha(\lambda)L/(\alpha(\lambda)L + 1/Z(\lambda))$ where $Z(\lambda) = n(\lambda)\pi$ is the two-dimensional bulk limit for the enhancement factor and L is the absorber thickness 1 µm [11, 77, 95]. The normalization factor is considered to be J_{ph} obtained by an unpatterned 1 µm thick c-Si with a Ag back reflector.

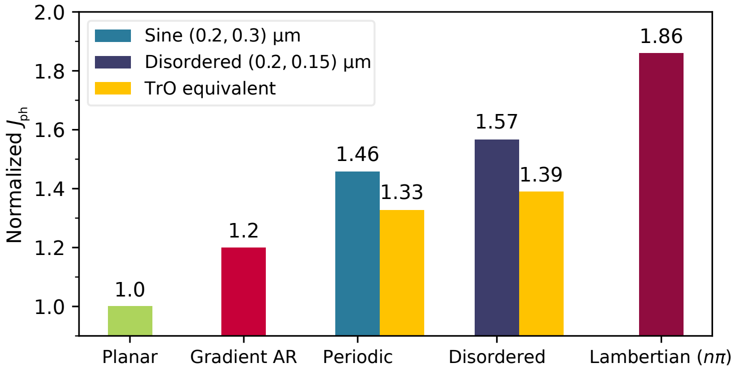

Figure 3.7: Comparison of J_{ph} for different geometries considered in the work. The normalized J_{ph} is calculated with respect to the 1 µm thick c-Si flat interface with Ag back-reflector: $J_{\mathrm{ph}} = 13.43\ \mathrm{mA/cm^2}$.

The best results are reported with the disordered structure, which outperforms the sinusoidal periodic texture with similar height profiles. This trend is also notably seen in the TrO counterpart of the disordered structure. Furthermore, the absorption in the c-Si layer for both cases approaches the theoretical limit proposed by a Lambertian scatterer in two dimensions.

To understand the benefits of our proposed structures, we can qualitatively estimate the detrimental impact of nanostructuring by considering the effective front surface recombination velocity, which is directly related to the surface enlargement factor γ. This factor represents the increase in the surface area of the absorbing layer due to nanostructuring [12]. Since our simulations are two-dimensional, we rather speak of the factor by which the length of the interface increases due to the texturing. For a texture with a profile $h = f(x)$ and a periodicity Λ for the unpatterned cell, the length enlargement factor E can be calculated as

$$E = \frac{1}{\Lambda}\int_0^{\Lambda} \sqrt{1 + \left(\frac{dh}{dx}\right)^2}\,\mathrm{d}x\,. \tag{3.6}$$

For the disordered structure with $\sigma = 0.2$ µm and $\zeta = 0.15$ µm, we find $E \approx 1.9$. This implies that for the given textured interface, just the length enlargement due to texturing will almost double the surface recombination velocity compared to the planar cell. In this scenario, the alternative TrO approach becomes beneficial, as the improved electrical performance from using the planar active layer can outweigh its slightly inferior optical performance compared to its textured counterpart.

3.6 Incoherent treatment of the Air-EVA interface

In this section, we explore the impact of including the Air-EVA interface in our optical simulations. The EVA encapsulant layer for the solar cells is typically around 400 µm thick. This poses a challenge for coherent light propagation and therefore requires an incoherent treatment. To address this, we maintain our simulation setup but account for the reflection from the Air-EVA interface *a posteriori* [96].

In practical terms, we need to consider each individual scattering path, referred to as diffraction orders, determined by the spatial frequencies of our interfaces. We analyze the response while gradually considering more back-reflections of light at the Air-EVA interface, which we term round-trip orders. We track the amplitude contained within each diffraction order in a sequence of increasing round trips within the EVA. This process applies to each temporal frequency individually. Initially, we consider normally incident light onto the structure, with the upper half-space filled with EVA. The amplitude of the field is corrected for an initial reflection at the Air-EVA interface, representing the zeroth interaction of light with this interface. Some of this light is absorbed by the active region, while the rest is reflected into discrete diffraction orders. Each of these diffraction orders is subsequently back-reflected onto the solar cell from the Air-EVA interface, constituting the first interaction of light with this interface. This back-reflected light serves as an incident field onto the active layer. We calculate absorption within the active layer and the distribution of back-reflected light, closing the iterative loop.

Expressing this mathematically, the contribution of the j^{th} round-trip order to the global absorbance for a fixed wavelength is computed as follows:

$$A^{j} = \boldsymbol{I}^{j}_{\mathrm{down}} \cdot \boldsymbol{A}\,, \tag{3.7}$$

where the j^{th} order corresponds to the j^{th} interaction of the light with the Air-EVA interface. $\boldsymbol{I}^{j}_{\mathrm{down}}$ is the intensity distribution incident on the structure and is given by:

$$\boldsymbol{I}^{j}_{\mathrm{down}} = \boldsymbol{I}^{j}_{\mathrm{up}} \odot \boldsymbol{R}_{a}\,, \tag{3.8}$$

where $\odot$ denotes the element-wise multiplication of the reflectivity R_{a} for the EVA-air interface for each diffraction order and intensity distribution $\boldsymbol{I}^{j}_{\mathrm{up}}$ in the j^{th} round-trip order correction of the reflected light from the structure. This quantity is calculated using a scattering matrix which relates the light incident on the structure to the light reflected from it and is given by:

$$\boldsymbol{I}^{j}_{\mathrm{up}} = \mathcal{S}\boldsymbol{I}^{j}_{\mathrm{down}}\,, \tag{3.9}$$

where the elements of this matrix are

$$\mathcal{S}_{\mathrm{ba}} = |E^{\mathrm{EVA}}_{\mathrm{ba}}|^{2}\frac{\cos\theta_{b}}{\cos\theta_{a}}\,. \tag{3.10}$$

Each coefficient of this matrix relates the b^{th} diffraction order in the reflected spectra to the a^{th} diffraction order in the incident field. The absorbance in the active layer till the n^{th}

round-trip order correction is then:

$$A^{\mathrm{n}}(\lambda) = \sum_{j=1}^{n} A^{\mathrm{j}} \, . \tag{3.11}$$

This process was iteratively carried out until the $A^{\mathrm{n}}(\lambda)$ converges to a value A_0 such that $A_0/A^{n-1} < 10^{-4}$. Note that the expressions above are only for a fixed wavelength. Therefore, this process is repeated for each wavelength of interest. Figure 3.8 shows the absorbance in the active c-Si layer in comparison to the results without the Air-EVA interface. Periodic and disordered textures and their corresponding TrO structures with refractive index bound of [1-3.5] were considered for this study. Figures 3.8(a) and (b) highlight the significance of correcting for the Air-EVA interface when estimating absorbance in the active layer, particularly in a realistic environment. The absorbance calculations that do not account for the Air-EVA interface underestimates the actual absorption in the active layer by a small amount. The correction factor plays a crucial role in rectifying this underestimation, especially for shorter wavelengths, where higher-order back-reflections become more pronounced.

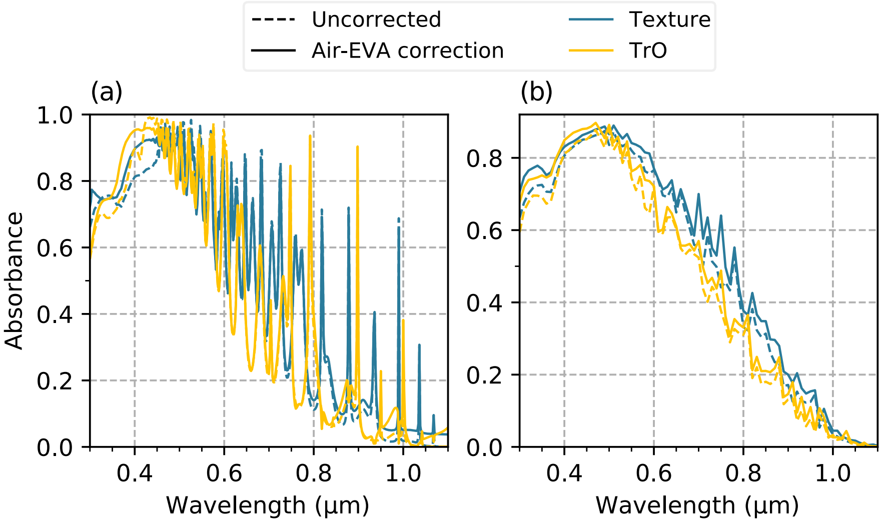

Figure 3.8: Global absorption spectrum obtained after considering reflection from Air-EVA interface for (a) sinusoidal texture of height $H = 2A = 0.2$ µm and lattice period $\Lambda = 0.3$ µm and (b) for the disordered texture of RMS roughness $\sigma = 0.2$ µm and correlation length $\zeta = 0.15$ µm. Adapted from Ref. [P1] with permission from © Optica Publishing Group.

In the case of periodic structures with a lattice period of $\Lambda_w = 0.3$ µm, only the zeroth diffraction order exists for wavelengths longer than 450 nm. Therefore, the first-order reflection correction suffices for the analysis. However, for disordered structures, characterized by larger periodicities, a significant portion of scattered light experiences higher-order diffraction. This fraction of light reflects from the Air-EVA interface and then illuminates the interface again, mainly remaining unabsorbed for wavelengths longer than 600 nm due to the thin active layer in our study. Consequently, the first-order correction becomes inaccurate for these structures. Therefore, a scattering matrix approach is essential for accurately modeling disordered structures in such scenarios.

J_{ph} (mA/cm^2)	Periodic		Disordered	
	Texture	TrO	Texture	TrO
300-500 nm	5.64	5.73	5.18	5.21
500-1100 nm	14.41	12.52	17.35	14.73
300-1100 nm	20.05	18.25	22.53	19.94

Table 3.3: Comparison of J_{ph} for periodic and disordered structures after accounting for escape losses from Air-EVA interface.

Table 3.3 provides a summary of the photocurrent J_{ph} after accounting for the Air-EVA interface. In the case of the periodic texture and its TrO counterpart, the most significant increase in overall photocurrent occurs for wavelengths shorter than 450 nm. On the other hand, for the disordered structure and its TrO counterpart, the increase in photocurrent is notable across a broader wavelength range, including longer wavelengths. These results indicate that the reflection correction has a notable impact on both the textured interface and its subsequent TrO structure. Such a reflection correction also affects both the geometries equally. While this is obvious in a certain sense since the TrO structure was designed to exactly have similar diffractive features, it further reinforces the idea of utilizing transformation optics concepts for mapping textured interfaces and their subsequent properties.

3.7 Effect of limiting the refractive index bound

In this section, we elaborate on the impact of choosing the upper limit for the refractive index of the TrO structure. While the previous choice of the upper bound was made to ensure better impedance matching with the bottom c-Si layer, it is important to explore the consequences of setting a lower upper bound on the refractive index for experimental feasibility.

Figure 3.9 illustrates the effect of restricting the permissible refractive index range in the TrO model for both periodic and disordered interfaces, as compared to the original refractive index range of 1 to 3.5. To provide a fair comparison, we also include a gradient AR coating, but now with a refractive index range between 1.5 and 2.5. Not surprisingly, choosing a lower upper-limit for the refractive index affects the impedance matching condition, particularly for wavelengths shorter than 500 nm, resulting in reduced absorption, as depicted in Fig. 3.9. However, the impact of opting for a smaller refractive index range is less significant for longer wavelengths, where the effective index experienced by light

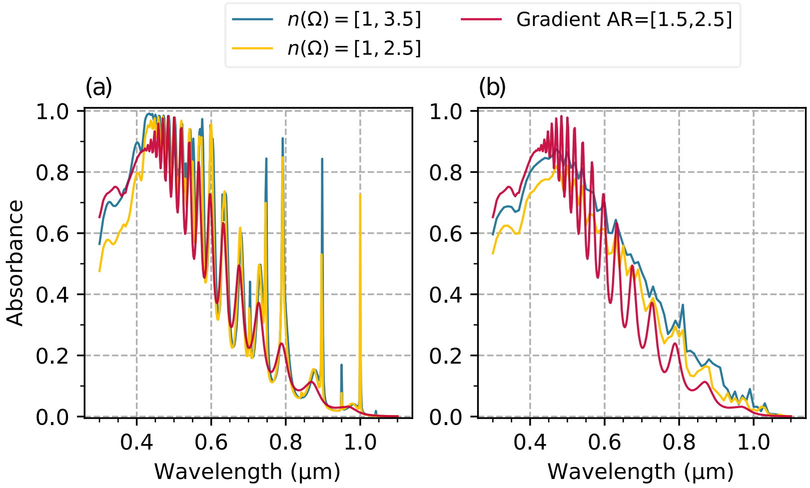

Figure 3.9: Absorption spectrum obtained for TrO structures with different permissible refractive index ranges for (a) Periodic structure mapped from a sinusoidal texture with height $H = 2A = 0.2$ μm and lattice period $\Lambda = 0.3$ μm (b) Disordered structure mapped from a disordered interface of RMS roughness $\sigma = 0.2$ μm and correlation length 0.15 μm.

does not change substantially.

Table 3.4 provides a summary of the photocurrent obtained for both shorter and longer wavelength ranges for these structures. These results are compared to a gradient AR coating with a refractive index range of [1.5, 2.5]. For the periodic structure, a smaller refractive index range does not substantially degrade its overall optical response. However, for the disordered structure, this degradation is more noticeable for shorter wavelengths. However, in both cases, they outperform the gradient AR layer for wavelengths longer than 500 nm, where, as discussed earlier, diffractive effects become significant. These results suggest that while the absolute improvement may be somewhat compromised when using a smaller refractive index range, the relative improvement over the gradient AR strategy with a similar refractive index upper bound continues to remain significant.

J_{ph} (mA/cm^2)	Periodic $n(\Omega)$		Disordered $n(\Omega)$		Gradient AR	
	[1,2.5]	[1,3.5]	[1,2.5]	[1,3.5]	[1.5,2.5]	[1.5,3.5]
300-500 nm	5.35	5.67	4.55	5.21	5.38	5.87
500-1100 nm	11.30	12.13	11.94	13.69	10.05	10.31
300-1100 nm	16.65	17.80	16.49	18.66	15.43	16.18

Table 3.4: Comparison of J_{ph} for periodic and disordered TrO structures for refractive index bound $n(\Omega) = [1, 2.5]$ and $n(\Omega) = [1, 3.5]$. Results are compared with Gradient AR coating of range [1.5,2.5] and [1.5,3.5].

3.8 Summary

In this chapter, we explored the application of transformation optics to design inhomogeneous refractive index structures for light trapping in planar thin-film solar cells. Our results demonstrate that by carefully selecting the properties of the texture, its equivalent planar inhomogeneous structure can notably enhance the absorbance in the planar c-Si thin-film layer, approaching the performance of the textured c-Si counterpart while also outperforming a broadband gradient anti-reflective (AR) coating with a similar refractive index range.

To experimentally realize the refractive index distribution shown in Fig. 3.4, a possible fabrication routine can be to first use self-organized colloidal nanolithography for depositing high refractive index nanostructures in a disordered manner. Then, through atomic-layer deposition techniques, conformally deposit ultrathin layers of dielectric materials over this disordered arrangement of nanostructures. However, the design strategy, and more importantly, finding the optimal design parameters, for such a structure must come by fully respecting the experimental methods in the process, something that is outside the scope of transformation optics. To fully appreciate the design strategy outlined here, we first explore the optical properties of the high refractive index disordered nanostructures in Chap. 4. More specifically, we study how one can use reciprocal space optimization procedure to come up with disordered configurations that are endowed with unique optical properties. Additionally, we also discuss how the very same optimization can also help in obtaining statistically stable simulation objects that can replace computationally expensive ensemble averages. The knowledge from Chap. 4 will then be utilized in Chap. 5 for designing structures similar to the ones presented in this chapter but with a design parameterization that fully respects the fabrication constraints.

4 Modelling optical properties of correlated disordered systems and overcoming simulation challenges

In this chapter, we will describe how positional disorder in a system can be tailored to give unique optical properties. The strategy for obtaining disordered configurations with a prescribed optical response in the single-scattering regime comes from a reciprocal-space optimization, the collective coordinate method (CCM), as described in Sec. 2.4.2. After an introduction, Sec. 4.2 discusses the optimization strategy for generating disordered hyperuniform particle distributions where the single-scattering response is suppressed at large length scales. The generated particle distributions are then used for designing a disordered metasurface which is integrated into a planar solar cell. The simulation setup and the key optical parameters used are described in Sec. 4.3. The merits of using such disordered hyperuniform distributions, particularly in the context of solar cells, are highlighted in Sec. 4.4. In that section, the optical properties of a disordered metasurface integrated into a solar cell are discussed. Section 4.5 explores the idea of using the CCM for realizing small-scaled particle distributions that mimic the scattering response of large-scaled particle distributions. The content of this chapter is mainly based on [P2]. Special thanks to Yannick Augenstein from TFP, KIT for performing a large-scale FDTD simulation of a sample that was used as a target for our analysis, and to Linus Schulte for generating and interpreting a set of results obtained from small-scale FDTD simulations. We also extend our thanks to Dr. Peter Piechulla for providing the preliminary scripts of the CCM and Random Sequential Adsorption (RSA).

4.1 Introduction

Tailored disorder has recently emerged as a promising paradigm in the field of photonics, offering versatile opportunities to manipulate various optical properties. Exploiting the rich design space afforded by the structural and material characteristics of disordered systems, researchers have harnessed this concept for creating tunable metasurfaces [97, 98], wavefront shaping [99, 100], light-localization [101–103], optical circuits [104], and many more [62, 105, 106]. Additionally, by carefully engineering the positional correlations of nanostructures within disordered arrangements, enhanced absorption, and light-trapping effects have been demonstrated [107–110].

The specific setup under investigation comprises an array of sub-micron-sized titanium dioxide (TiO_2) nanodisks arranged with correlated positional disorder on a planar silicon substrate. These sub-micron disks, given an appropriately tailored height and diameter, exhibit exceptional scattering characteristics [111]. They can leverage a generalized form of the Kerker effect, achieving complete suppression of backscattering for cylindrically symmetric, helicity-preserving particles, provided a sufficiently high degree of rotational symmetry in the scattering array is maintained [112, 113]. These TiO_2 nanodisks have demonstrated remarkable effectiveness in various periodic lattice configurations, enabling the complete suppression of off-axis reflection for wavelengths exceeding the grating pitch of the array [113, 114]. While these arrangements offer outstanding scattering capabilities, the complexity of realizing periodic structures experimentally and concerns related to industrial scalability are inherent challenges.

A promising alternative involves fine-tuning the spatial correlation to suppress long-range density fluctuations by arranging nanodisks in a disordered hyperuniform pattern, effectively suppressing diffused light scattering. Due to the system's continuous rotational symmetry, specular light scattering can also be suppressed in the long-wavelength limit when illuminated with circularly polarized light at normal incidence, aligning with the aforementioned zero-specular-backscattering condition based on helicity [115]. This property results in exceptional anti-reflective characteristics, as previously documented [116]. However, full-wave simulations for such systems remains a bottleneck. Due to the significance of long-range order in such particle assemblies, samples considered for simulations should have a spatial extent on the order of 10 μm or larger. Additionally, the spatial resolution of the simulation domain must be sufficiently high to accurately represent sub-micron-sized particles. Consequently, a systematic numerical exploration of these nanodisk-metasurfaces with correlated disorder, when integrated with a stratified layer setup, has remained largely unexplored.

To respond to such challenges, this work uses the collective coordinate method (CCM), previously described in Sec. 2.4, to generate hyperuniform particle configurations. The CCM is frequently used for obtaining large-scale disordered particle arrangements with prescribed scattering features [117–120]. We first demonstrate this method to generate unique disordered configurations. Particularly, we focus on stealthy hyperuniform systems that completely suppress diffused scattering in the single-scattering regime beyond a certain length scale. With the help of full-wave numerical solutions, we show that the complete suppression of diffused scattering in such systems fully justifies the importance of hyperuniformity in disordered metasurfaces used for solar cells.

We also exploit the CCM to realize small-scale disordered samples that match a target structure factor obtained from a large-scale sample up to a reasonable degree of accuracy while also obeying constraints like non-overlapping particles and periodic boundaries. The result is a comparably smaller sample, more feasible to simulate numerically using FDTD (described in Sec. 2.5) that continues to incorporate the long-range scattering information. Therefore, the question we address is how representative CCM-generated particle arrangements are in emulating a large-sample target optical response in comparison to an ensemble-averaged response of several smaller-domain samples.

4.2 Disordered hyperuniform systems and collective coordinate method

This section discusses the properties of hyperuniform correlated disordered systems and how they can be generated via the CCM. At first, we introduce a modified version of our algorithm for this method. The particle distribution is obtained by tiny collective displacements of each particle in each iteration until a desired objective is reached. At a later stage, the particle positions derived from the process will be used to design metasurfaces with a prescribed functionality.

4.2.1 Modified CCM algorithm

Consider a particle distribution $\mathbf{R}^N \equiv \mathbf{R}_1, \mathbf{R}_2, .., \mathbf{R}_N$ contained in a domain $\mathcal{V}$ of size $L \times L$. The objective function $\Phi(\mathbf{R}^N)$ defined using a sum of Eq. 2.98 and Eq. 2.99 is then minimized using a gradient-based optimization with gradients given by Eq. 2.100. We enforce periodic boundaries to the domain since the spatial extent of such a particle arrangement is finite but the length correlations among the particles must also be obeyed beyond this domain. For this, region $\mathcal{V}$ is tesselated in the xy-plane to have its copies from adjacent unit-cells as its neighboring particles. We use this tesselated distribution to evaluate $\Phi_g(\mathbf{R}^N)$.

For our purpose, we use the term $\Phi_g(\mathbf{R}^N)$ in the objective function to avoid overlapping particles in the system. This is because, for realistic scenarios where the disordered arrangement of particles is often obtained from a self-assembly process, the particles aggregate (forming dimers, trimers, etc) but never overlap. The overlapping constraint is imposed through the pair-correlation function. This is done by realizing that, for non-overlapping particles, the pair-correlation function is strictly zero at distances smaller than the size of the particles contained within $\mathcal{V}$ as well as on its boundaries $\partial\mathcal{V}$. For cylindrically symmetric particles, this implies $g(\mathbf{r}) = 0$ for $|\mathbf{r}| < r_0$.

The objective function is evaluated for each iteration, and the optimization terminates when the final particle distribution gives the desired pair-correlation statistics. Since tesselating the unit-cell will inevitably give overlapping particles if the optimal particle arrangements are found outside the unit-cell, the variables of the optimization are also bounded to be inside $\mathcal{V}$.

4.2.2 Hyperuniform distributions

We demonstrate the applicability of the optimization procedure described in Sec. 4.2.1 for generating particle distributions with hyperuniform disorder.

Figure 4.1 illustrates three stealthy hyperuniform systems contained in a box of size $\mathcal{V} = 8 \times 8$ µm^2. Figure 4.1(a) is a standard infinite square lattice while Figs. 4.1(b) and (c)

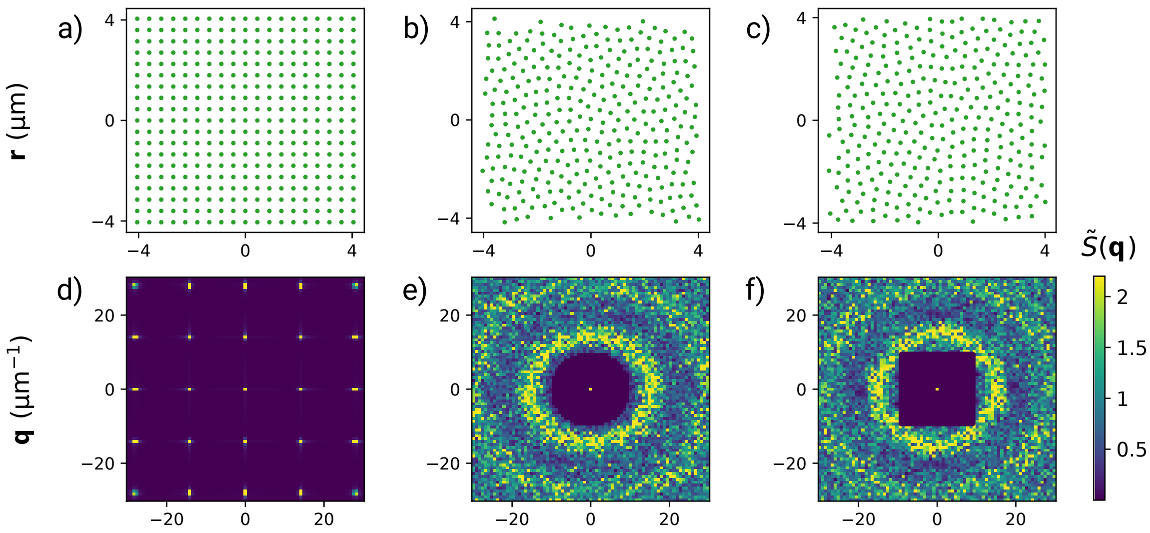

Figure 4.1: Illustration of three hyperuniform systems. All distribution have the same particle density $\rho = 4.5\ \mu\text{m}^{-2}$ and radius $r = 0.175\ \mu\text{m}$. (a) Square lattice with lattice vector $\boldsymbol{\Lambda} = [0.47, 0.47]\ \mu\text{m}$. (b) Stealthy isotropic hyperuniform disorder ($\tilde{S}(\boldsymbol{q}) = 0$ for $|\boldsymbol{q}| < q_c$). (c) Stealthy anisotropic hyperuniform disorder ($\tilde{S}(\boldsymbol{q}) = 0$ for $q_x = q_y < q_c$). (d), (e), and (f) are the corresponding structure factor in 2D for the particle distributions in (a), (b), and (c), respectively. Here, $q_c = 10\ \mu\text{m}^{-1}$. The structure factor shown for the disordered samples are ensemble-averaged over 5 realizations.

are stealthy disordered configurations generated using the modified version of the CCM. For comparing similar features, we fix the particle density to be $\rho = 4.5\ \mu\text{m}^{-2}$ for each case. This way, the square lattice has a pitch $\Lambda = 1/\sqrt{\rho} = 0.47\ \mu\text{m}$ while the other two have a mean inter-particle distance $\bar{d} = 1/\sqrt{\rho} = 0.47\ \mu\text{m}$.

The structure factor $\tilde{S}(\boldsymbol{q})$ for each case is shown Figs. 4.1(d)-(f). The structure factor is calculated using Eq. 2.94. For the periodic case, the sharp features in the reciprocal space are characteristic of Bragg scattering occurring at $\boldsymbol{q} = 2\pi/\boldsymbol{\Lambda}$ where $\boldsymbol{\Lambda} = [\Lambda_x, \Lambda_y]$ is the lattice vector. For the disordered samples, the structure factor is obtained from an ensemble-average given as

$$\langle \tilde{S}(\boldsymbol{q}) \rangle = \frac{1}{M} \sum_{i=1}^{M} \tilde{S}_i(\boldsymbol{q}) \,, \tag{4.1}$$

where M is the number of sample realizations considered for the ensemble-average. For this case, we choose $M = 5$. The scattering patterns in Fig. 4.1(e) and Fig. 4.1(f) are obtained by tailoring the Fourier transform of the pairwise additive potential $v(\mathbf{r})$ defined in Eq. 2.98 and Eq. 2.99. This way, a prescribed response in the reciprocal space is obtained which can be isotropic, like in Fig. 4.1(e), or anisotropic, like in Fig. 4.1(f). The reason for the anisotropy in Fig. 4.1(f) is that, the $\tilde{S}(\boldsymbol{q})$ is only identical along $\hat{\boldsymbol{q}}_x$ or $\hat{\boldsymbol{q}}_y$ direction, but not continuously in a circular disc. It is surprising to see that while the particle distributions of the disordered case look quite identical, their structure factor, and thus their large-scale density fluctuations, are dramatically different. This is because of the human tendency to focus only on the structural similarities at a short length scales. Thus, such systems are often said to have a "hidden" order on large length scales [71].

It can be seen from Figs. 4.1(d), (e), and (f) that the periodic and the disordered samples are stealthy hyperuniform as the structure factor is strictly zero for a subset of wave vectors. For both disordered cases, the system behaves like a perfect crystal (infinite periodic lattice) in a way that it suppresses single scattering of incident radiation at infinite wavelengths. But, like a liquid or a gas, the disordered samples have no Bragg peaks. These features are characteristic of a disordered hyperuniform distribution. Due to the complete suppression of scattering for a range of wave vectors, such correlated disordered distributions have been used to design materials that possess complete photonic band gaps. The size of the band gap for such materials is comparable to those in photonic crystals [103, 120].

Stealthy hyperuniform patterns are parameterized by q_c, or equivalently χ which specifies the fraction of wavenumbers within the Brillouin zone that are strictly set to zero. In other words, k_c decides the number of constrained and unconstrained wave vectors during the optimization process. The parameter χ for the stealthy hyperuniform distributions can then be defined as [71]:

$$\chi = \frac{M(q)}{2(N-1)}\,, \tag{4.2}$$

where $M(q)$ is the number of independently constrained wave vectors, and N is the total number of particles. Since the simulation domain is finite, for a domain of size $\mathcal{V} = L \times L$, this sets a limit to the sampling frequency in the reciprocal space, such that $dq = 2\pi/L$. The number of independently constrained wave vectors is then directly dependent on the spatial extent of the sample. For sufficiently small χ, the particle distributions are highly degenerate and strongly disordered. This is because, for small χ, the system is free of any constraints with $\chi = 0$ being the extreme case where the system is structurally like a non-interacting classical ideal gas [121]. As χ increases, the critical wavenumber q_c, and thus the degree of hyperuniformity increases. For $\chi > 0.58$, the particle distributions make a crystalline transition and start to develop local periodic clusters in the system [64]. For the critical value $\chi_c \approx 0.77$, the system develops long-range translational order [122]. For our analysis, we generate stealthy disordered states with $\chi = 0.55$ and $q_c = 10.2\ \mu\text{m}^{-1}$.

The robustness of our algorithm can be better appreciated by considering a case where it is desired to arbitrarily fix particle positions during the optimization. This can be trivially done by setting $d\Phi/dR_m = 0$ for $m < N$ particles. This way, one can sequentially tailor each species of particles inside the system to have a prescribed structure factor. One such example is illustrated in Fig. 4.2.

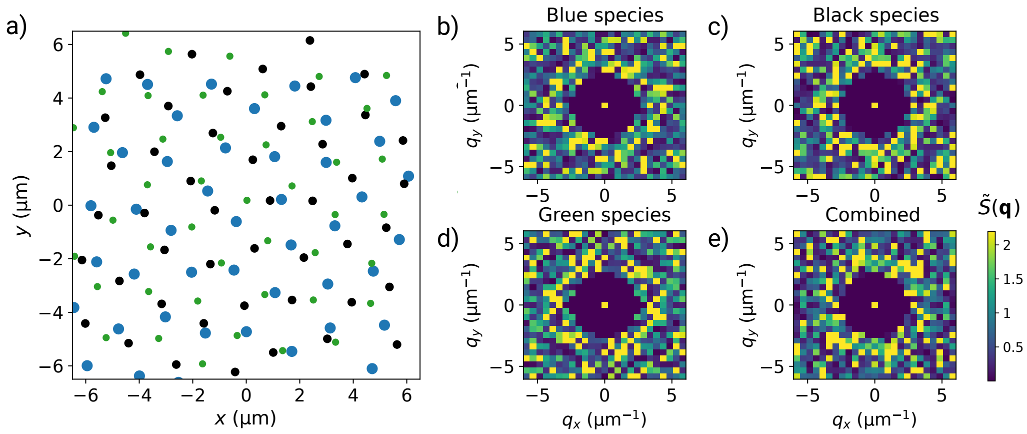

Figure 4.2: Illustration of a multihyperuniform system. (a) Particle distribution of the system. Each colored marker represents a different species in the system with the size of the marker signifying its corresponding diameter (to scale). By imposing similar constraints as above, the combined system contains no overlapping particles.

The particle distribution shown in Fig. 4.2(a) consists of three species: Blue, Black, and Green, each having a different diameter. The optimization then runs thrice with each run optimizing the particle distribution of the current species while keeping the other fixed. In this case, each species is made to have stealthy hyperuniform characteristics. As a consequence, it is observed that not only do individual species satisfy this criterion, but collectively, the entire particle distribution is seen to have a stealthy hyperuniform behavior, hence the "multihyperuniform" nature. This is evident in $\tilde{S}(\boldsymbol{q})$ shown in Figs. 4.2(b) - (e). Though not stealthy, similar particle distributions are observed in the avian eye and are responsible for giving spectacular color resolution. There, the cone photoreceptors consist of five different cell types that are individually hyperuniform while the entire collection also being hyperuniform [123].

4.2.3 Near hyperuniformity

Since hyperuniformity is an infinite-wavelength property and the numerical simulations and the fabricated samples of such systems are finite-sized, it is useful to describe a metric that classifies the hyperuniformity of the system and specifies a criteria for "effective" or "near" hyperuniformity. A useful metric described as

$$H = \frac{\tilde{S}(\boldsymbol{q} \to 0)}{\tilde{S}(\boldsymbol{k}_{\mathrm{peak}})}\,, \tag{4.3}$$

has been proposed to roughly classify the hyperuniformity of the finite systems [71, 124]. Such a metric is intuitive as it compares the first dominant peak value of the structure factor $\tilde{S}(\boldsymbol{k}_{\mathrm{peak}})$ to the estimated value at the origin. While such a value must be of the order 10^{-4} for effectively hyperuniform systems, for nearly hyperuniform systems, this value is relaxed to be approximately 10^{-2} [125].

Nearly hyperuniform distributions are generated in this thesis using a modified Random Sequential Adsorption (RSA) method. This process is known to accurately predict observable patterns achievable through a specific experimental approach [23]. The experimental approach involves immersing a weakly positively charged substrate into a colloid dispersion of weakly negatively charged nanoparticles. Electrostatic forces, including attraction between the substrate and nanoparticles, and repulsion among the nanoparticles, drive the formation of a correlated disorder particle pattern. The metasurfaces we shall consider later in this chapter can be derived from the deposited nanoparticles in a dedicated experimental procedure [126]. Due to the inherent statistical constraints of this process, the resulting patterns exhibit high isotropy and near-hyperuniformity at large length scales.

Numerical simulations of this process involve predicting point configurations for particle centers through a Monte Carlo-style algorithm that generates correlated disorder point patterns in a manner akin to the real-world process [23]. In this simulation, random positions within a specified sample area are sequentially selected one by one from a uniform probability distribution. However, before incorporating any point into the pattern, a sticking probability for its position is computed. Similar to its real-world electrostatic counterpart, the underlying probability density depends solely on the distance to neighboring particles that have already been placed. For any new point, the probability of its integration into the sample is modeled using a half-Gaussian distribution:

$$p_{\mathrm{stick},i} = \prod_j \begin{cases} \exp\left(-\frac{(d_{i,j}-\bar{d})^2}{2\sigma^2}\right) & d_{i,j} \leq \bar{d} \\ 1 & d_{i,j} > \bar{d}\,. \end{cases} \tag{4.4}$$

In this context, $d_{i,j}$ represents the distance between two particles, while the desired mean particle distance $\bar{d}$ and variance σ define the Gaussian distribution. The mean distance in such a particle arrangement is directly related to the per-area particle density ρ_p of the sample, with $\bar{d} = 1/\sqrt{\rho_p}$. The generation algorithm is provided with a target particle density ρ_p and an appropriate σ value. It then proceeds to add points to the pattern iteratively until the desired density is achieved. For this work, a constant value of $\sigma = 0.05$ µm was chosen, striking a reasonable balance between sample generation runtime and pattern uniformity. Due to the probabilistic nature of this process, the pair-correlation function of the system fixes the structure factor of the resulting particle distribution. This is shown in Sec. 2.4.2 in Fig. 2.6 with the red curve. Consequently, this makes the CCM redundant for generating such patterns. However, as we shall see in Sec. 4.5, when considering small and few-particle systems of such a point-process, it is still possible to benefit from an optimization where the objective is to match the structure factor of a large many-particle system of the same point-process.

Given the particle distributions obtained using the above considerations, we shall design a disordered metasurface for a planar solar cell in the following section. It shall also describe the optical parameters that are used for assessing the performance of these structures.

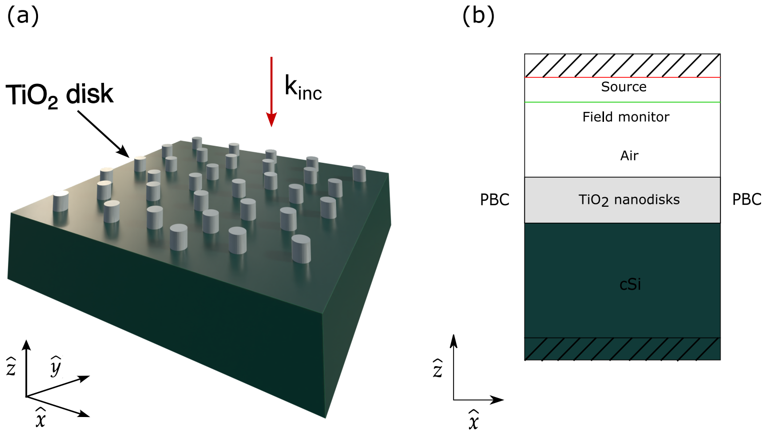

Figure 4.3: Schematic of the conceptional solar cell setup considered in the simulation throughout this work. A cSi substrate is considered onto which TiO$_2$ nanodisks are placed. The illumination is a plane wave of circular polarization and negative helicity at normal incidence.

4.3 Unit-cell design and simulation setup

The point-distributions obtained from the CCM are used as centers for placing identical nanodisks at the corresponding locations. This is integrated into a planar solar cell, and the optical response of such a system is obtained from an FDTD simulation as implemented in Meep [75]. To accurately capture the system's long-range characteristics in numerical simulations, employing a computational technique such as the Finite-Difference Time-Domain (FDTD) method proves invaluable. This method enables the comprehensive assessment of the system's spectral response when subjected to Gaussian pulse illumination, all within a single simulation. Additionally, FDTD computations are memory-efficient and amenable to parallelization across multiple processing cores, rendering them highly suitable for simulating large systems.

The resulting geometry of the setup is depicted in Fig. 4.3. A cSi substrate is employed, and the upper half-space is filled with air. The layer of TiO$_2$ nanodisks is directly placed at the air-cSi interface. Dispersive material properties for both materials used in the simulations are extracted from existing literature sources [92, 127]. Given that the primary focus of this thesis is on the anti-reflective and light-trapping properties of the nanodisk metasurface and the associated statistical fluctuations resulting from the spatial arrangement of the disks, we simplify the model by not considering reflections from the bottom interface back into the simulation domain. This simplification assumes a semi-infinite lower half-space of cSi.

A right-handed circularly-polarized plane wave (that is, with negative helicity) propagating in the negative z-direction is used for illumination. It should be noted that such strictly polarized illumination is not identical to the unpolarized light from solar irradiation, which is composed of an equal share of both positive and negative helicity. However, the response of the investigated systems does not depend on the incident helicity. The same results would be obtained for illumination with positive helicity. The obtained results are, therefore, representative of real-world irradiation.

4.3.1 Optical parameters

To understand and tailor the scattering properties of a disordered hyperuniform particle distribution in a full-wave simulation, and beyond the single-scattering regime, we measure the spatial distribution of the reflected field in the FDTD simulation. The recorded reflected power in the air half-space $\mathbf{E}_R(\mathbf{r}, t)$ is first Fourier-transformed into frequency-domain to obtain $\widetilde{\mathbf{E}}_R(\mathbf{r}, \omega)$ which is then Fourier-transformed in spatial-frequency domain to get $\widetilde{\mathbf{E}}_R(\mathbf{k}, \omega)$. The reflectance is calculated using this quantity normalized with the predetermined power of the incident field. This is given as:

$$R(\omega) = \frac{\sum_{k_x,k_y} \left|\widetilde{\mathbf{E}}_R(k_x, k_y, \omega)\right|^2 \cdot \cos\left(\theta(k_x, k_y, k_z)\right)}{\left|\widetilde{\mathbf{E}}_{\text{inc}}(\omega)\right|^2}. \tag{4.5}$$

Using $\omega = 2\pi c/\lambda$, the reflectance, can then be expressed in terms of the wavelenth, as $R(\lambda)$. This reflectance can be split into its specular and diffuse components. For a normal illumination, specular reflection is the share of light that is back-reflected at $k_x, k_y = 0$. That is, all the reflected light propagating in positive z-direction. This is already captured in the preceding equations by making $\theta = 0$ whereas all the portion of the scattered light outside this region at all angles other than zero is the diffused reflection.

Similar to this directional breakdown of the reflection, a distinction between positive and negative helicity components can be made. As we will explain in Sec. 4.4, some of the backscattering suppressing properties of correlated disorder stems from its ability to preserve the helicity of the incident light for long wavelengths while having an effectively continuous rotational symmetry around the incident axis [126]. Therefore, it is of interest to examine the components of reflected light with positive and negative helicity independently. The decomposition into positive and negative helicity components is most easily done by expressing the fields in the helicity basis:

$$\mathbf{E}_{\pm}(\omega) = \widetilde{\mathbf{E}}(\omega, \mathbf{k}) \cdot \hat{\mathbf{e}}_{\pm}(\mathbf{k}) \,, \tag{4.6}$$

where the helicity basis vectors are composed by the $\hat{\mathbf{s}}$ and $\hat{\mathbf{p}}$ polarization vectors:

$$\hat{\mathbf{e}}_{\pm}(\mathbf{k}) = \frac{1}{\sqrt{2}}\left[\hat{\mathbf{s}}(\mathbf{k}) \pm \hat{\mathbf{p}}(\mathbf{k})\right]. \tag{4.7}$$

The obtained fields $\mathbf{E}_{\pm}(\omega)$ can now be used to compute the positive and negative helicity fractions $P_{\pm}$ of the reflected power [30].

4.3.2 Parameter search for an optimal geometry

The parameters defining the geometry of the disordered metasurface that are investigated throughout this chapter, and also in Chap. 5, are obtained from periodic simulations wherein the height h, diameter d, and lattice constant Λ of the TiO_2 nanodisks array are optimized. The objective of the optimization is to minimize the reflection loss across the spectral range of 320 nm−1100 nm. As explained in Sec. 2.3, this spectral region is crucial for a solar cell due to the high solar irradiance here. For the disordered simulations, the lattice constant is replaced with the mean interparticle distance (correlation length) while the remaining quantities are kept unchanged. This way, the insight into the optimal parameter space for the disordered hyperuniform system stem from its stealthy hyperuniform, but periodic, counterpart. Given the set of these parameters $\mathbf{Q} = [h, d, \Lambda]$, the optimization problem can be written as:

$$\min_{\mathbf{Q}} J_{\mathrm{R}}(\mathbf{Q}) = \int_{\lambda_0}^{\lambda_f} \Phi_{\mathrm{AM1.5G}}(\lambda)\, R(\mathbf{Q},\lambda)\, \mathrm{IQE}(\lambda)\, \mathrm{d}\lambda, \tag{4.8}$$

where $R(\mathbf{Q}, \lambda)$ is the reflection spectrum obtained for the given set of parameters $\mathbf{Q}$ and $J_{\mathrm{R}}(\mathbf{Q})$ is simply the current loss as given in Eq. 2.76. These parameters are then fed to a hyperparameter optimization for minimizing $J_{\mathrm{R}}(\mathbf{Q})$. It is worth mentioning that these hyperparameters are different than our geometrical parameters. The hyperparameters are variables that control the learning process of the optimization model. In simpler terms, they dictate how optimizer learns an underlying relation between the input parameters, in our case $\mathbf{Q}$, and the predictions, in our case J_{R}. Since these hyperparameters are problem-specific, they must be tuned for the optimization model to yield optimal results that minimizes the loss function. A typical hyperparameter optimization then involves tuning the hyperparameters based on the value of the objective function returned for a parameter-set. The optimizer assess the performance of the hyperparameters to determine the parameter-set for the next trial. In this work, the Optuna optimization algorithm was employed [128]. The optimal parameters of the system in the periodic arrangement were found to be $h = 160$ nm, $d = 350$ nm, and $\Lambda = 500$ nm. The current-loss for these optimal parameters was found to be 1.80 $\mathrm{mA/cm^2}$. To avoid repetition, we present a comprehensive discussion of the results for this periodic optimization in Chapter 5. At this point, it suffices to use the parameters obtained from this optimization when discussing the results for its disordered counterpart. Nonetheless, for those interested, please refer to Fig. 5.5 (represented by dashed linestyles) for this data.

4.4 Optical properties of the disordered hyperuniform metasurface

This section utilizes the geometry of the solar cell defined in Sec. 4.3 for studying the optical properties of the disordered hyperuniform metasurface using FDTD simulations. Even though all later simulations are full-wave optical simulations, the consideration of the structure factor as the prime quantity to be tailored can be explained when considering the scattering of light at the metasurface in the lowest order Born-approximation [126].

The lowest order Born-approximation describes the scattering response of an array of identical particles with only two quantities. First, the form factor $\tilde{f}(\boldsymbol{q})$, which describes the scattering response of a single, isolated particle. Second, the structure factor $\tilde{S}(\boldsymbol{q})$, which describes the spatial correlations between the particles. The former can be determined either by simulations or even analytically for spherical particles, while the latter can be determined by using Eq. 2.94. Until now, the vector $\boldsymbol{q}$ specified the spatial frequency of the setup. From here on, we consider the scattering of light from the metasurface. The vector $\boldsymbol{q}$ is then called the scattering vector since it connects the wave vectors of the incident and the scattered field as $\boldsymbol{q} = \mathbf{k}_{\text{scat}} - \mathbf{k}_{\text{inc}}$.

As briefly outlined in Sec. 4.1, the design of our proposed metasurface draws inspiration from previous work [113, 126]. In these studies, the anti-reflective properties of nanodisk metasurfaces were tailored with consideration of the helicity of backscattered light. Preserving the helicity of the incident light, combined with discrete rotational symmetry $C_{n>2}$ within the scattering system along the illumination axis, ensures zero specular backscattering within the sub-wavelength regime [115]. Thus, adjusting the aspect ratio of these cylindrically symmetric nanodisks and arranging them in square or hexagonal lattices establishes sufficient conditions for helicity preservation across a relatively broad spectral range. Remarkably, this effect can also be achieved in disordered systems with a careful design, leading to an effective continuous rotational symmetry ($C_{n\to\infty}$) in the long-wavelength limit. In our investigation here, we study this property of a disordered hyperuniform system. For a thorough comparison, we compare the results from a periodic arrangement of nanodisks with the stealthy hyperuniform disordered nanodisk array as well as the nearly hyperuniform RSA disordered nanodisk array. We analyze the mean reflectances of their corresponding systems by separating them into their positive and negative helicity components, as detailed in Sec. 4.3.1.

Figure 4.4 shows the reflectance obtained for solar cells with metasurfaces of three types: infinitely periodic square lattice (represented by dashed orange line), stealthy disordered hyperuniform disorder (represented by solid blue line) generated by CCM, and lastly, nearly hyperuniform RSA distribution (represented by solid green line). The height, diameter and lattice constant are chosen to be $h = 160$ nm, $d = 350$ nm, and $\Lambda = 450$ nm.

In the case of disorder, the lattice constant is replaced by the mean-interparticle distance denoted as $\bar{d}$. Unlike the infinitely periodic square lattice, the disordered arrangements are finite and are generated for a sample of size $8 \times 8\ \mu\text{m}^2$. This corresponds to having approximately 18 mean-interparticle distances across the simulation domain (roughly 315 particles). The reflectance values shown for the disordered systems are averaged over five different sample realizations for a robust statistical analysis.

The total reflectance in Fig. 4.4(a) for each of the three case is suppressed for a broadband spectral range. To understand this behaviour, we look at the angular-averaged structure factor for these samples in the inset figure of Fig. 4.4(a). For the stealthy disordered sample

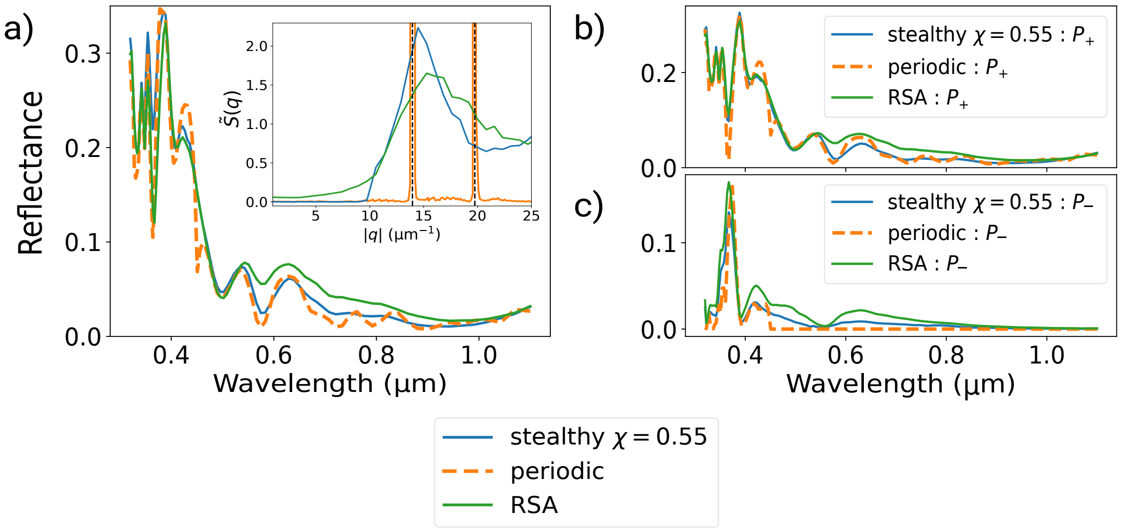

Figure 4.4: (a) Total reflectance of TiO_2 nanodisks arranged in periodic square lattice (dashed orange), stealthy hyperuniform disordered (blue), and nearly hyperuniform RSA type (green) setup. The inset in (a) is the angular-averaged structure factor for the same samples. The total reflectance is helicity-decomposed into (b) Positive helicity component P^{+}, and (c) Negative helicity component P^{-} for each of the samples.

(blue solid line), the structure factor is strictly zero for $|\boldsymbol{q}| < 10.2\ \mu\text{m}^{-1}$. In contrast, the structure factor for the RSA disordered sample (green solid line) smoothly approaches zero for $|\boldsymbol{q}| \rightarrow 0$. The cut-off of $q_c = 10.2\ \mu\text{m}^{-1}$ for the stealthy disordered case was chosen so that scattering of light for wavelength $\lambda > 2\pi/q_c \approx 610$ nm is restricted to only the specular part (in the single-scattering limit). For the reciprocal space resolution of $dq = 2\pi/L$, the hyperuniformity metric is then $\chi = 0.55$. The particle distribution for the stealthy disordered sample and its ensemble-averaged $\tilde{S}(\boldsymbol{q})$ is shown in Figs. 4.1(b) and (e). The inset figure also shows the angular-averaged structure factor for a square lattice. Like the stealthy disordered case, $\tilde{S}(q)$ is gapped for the square lattice, but unlike the former, possesses long-range order as shown by the sharp Bragg peaks at $q_0 = 2\pi/\Lambda$. Therefore, it can be concluded that the total reflection for each case is suppressed beyond $\lambda > 610$ nm due to the structure factor approaching zero [P3].

The decomposition of reflectance spectra from Fig. 4.4(a) into their helicity components, P_+ and P_- are shown in Figs. 4.4(b) and (c), respectively. It is apparent from these results that the positive (P_+) component, where helicity was flipped, contributes the largest share to the overall reflectance beyond the wavelength corresponding to the lattice constant or the mean inter-particle distance, that is $\lambda_c > 450$ nm. This is due to the suppressed diffuse reflection in this spectral region and the nanodisk arrangement approaching an overall $C_{n\rightarrow\infty}$ symmetry as a result of the long-range uniformity of point distributions.

J_R (mA/cm^2)	Periodic	Stealthy ($\chi = 0.55$)	RSA
$J_{\mathrm{R},P+}$	1.82	1.81	2.33
$J_{\mathrm{R},P-}$	0.11	0.30	0.58
Total reflectance	1.93	2.11	2.91

Table 4.1: Current-loss J_R evaluated for each sample and decomposed into its helicity components.

The trends observed for each sample in Fig. 4.4 are summarized in Tab. 4.1 as a measure of lost photocurrent, quantified using Eq. 2.76. Additionally, this quantity is further decomposed into its helicity components, represented as $J_{\mathrm{R},P+}$ and $J_{\mathrm{R},P-}$, and evaluated based on the spectra shown in Figs. 4.4(b) and (c), respectively. Upon analyzing Fig. 4.4 and Tab. 4.1, it becomes evident that the stealthy disordered sample clearly outperforms the RSA sample, close to the infinitely periodic square lattice limit. For the stealthy disordered sample, the majority of the deviation in reflectance from the square lattice is primarily attributed to the same helicity component, P_-, while the flipped helicity component, P_+, closely resembles that of the square lattice. In contrast, the RSA sample exhibits a more pronounced deviation from the stealthy disordered case, particularly noticeable beyond λ_c. This observation aligns with the fact that, for longer wavelengths, the stealthy disordered system entirely suppresses single scattering, whereas the RSA system only approximates this condition. The nearly hyperuniform nature of the RSA samples allows a small portion of diffused light to still be scattered. As this diffused light is not aligned with the axis of illumination, it contributes to increased reflection in the same helicity component, P_-.

Although the stealthy particle arrangement offers remarkable scattering properties, closely resembling those of periodic structures, its practical implementation poses challenges similar to periodic arrangements. This complexity in realizing such particle configurations experimentally raises concerns related to industrial scalability. However, it is crucial to highlight that the RSA samples result from a self-assembly fabrication process, making them a viable choice for large-scale production in a cost-effective manner [129]. Given this consideration, it is noteworthy that despite being only nearly hyperuniform, the RSA sample provides a compelling alternative to the stealthy hyperuniform systems, whether periodic or disordered, particularly in the context of anti-reflection and light-trapping for solar cells. As a result, for the remaining part of this thesis, our focus shifts to nearly hyperuniform systems characterized by RSA-type disorder.

In the next section, we investigate the impact of using a simulation domain for the disordered RSA samples that is much smaller than 8×8 μm^2 considered in this chapter. Then, the question we ask ourselves is how representative is the optical response of such small spatial domain sample, and how can CCM be helpful in improving the statistical stability of the results.

4.5 Collective Coordinate Method for generating smaller sized samples

Until now, the size of the samples has been considerably larger than the mean interparticle distances. This deliberate choice ensured that the optical response was adequately averaged over numerous particle configurations within each sample. However, it is worth noting that conducting a single FDTD simulation for a disordered metasurface in a solar cell setup of this scale required roughly 5 hours of computational run-time, even when parallelized across multiple cores. And this does not take into account the additional effort needed to obtain an ensemble-averaged response or performing various parametric runs for different geometric properties. Consequently, the computational analysis of such large-scale disordered systems remains a significant challenge due to their long-range scattering responses. To address this challenge, we explore the Collective Coordinate Method (CCM) to obtain smaller, optimized super-cells that are suitable for computational analysis while still faithfully representing the spatial correlation characteristics of the larger system.

To test the viability of these optimized particle distributions as reliable and self-consistent simulation objects, it is crucial to demonstrate that their simulated optical properties converge towards the results expected from larger samples containing hundreds of particles, which aligns with more realistic experimental scenarios. Also, in the case of relatively smaller-sized particle patterns, where particle placement follows the same probability distribution as in larger samples, it is customary to perform ensemble averaging over these smaller-sized samples [130]. Our primary objective is, therefore, to assess the reliability of the optical response obtained from these CCM-optimized samples. This assessment involves comparing them with ensemble-averaged unoptimized samples, and large-scale samples that preserve long-range information, and are generated using probabilistic methods like the Random Sequential Adsorption (RSA) process. Please note, while the method described here effectively captures the long-range response of a nearly-hyperuniform structure within a small sample, this work focuses solely on the application of CCM optimization in the context of solar cell simulations. However, it is worth emphasizing that the approach presented here is not conceptually limited to this specific application. Further investigations and applications beyond the scope of solar cells are strongly encouraged.

4.5.1 Optimization problem

The goal of introducing long-range order of a probabilistic point-distribution $\mathcal{R}^N \equiv \mathcal{R}_1, \mathcal{R}_2, \ldots, \mathcal{R}_N$ into smaller sample domains is essentially to find a set of particle positions $\mathbf{R}^M \equiv \mathbf{R}_1, \mathbf{R}_2, \ldots, \mathbf{R}_M$ that demonstrate similar reciprocal-space properties as the target large-domain sample. This objective function is defined as follows:

$$\Phi(\mathbf{R}^M) = \sum_{q\in\Omega} \left[\tilde{S}(\boldsymbol{q}) - \tilde{S}_{\text{target}}(\boldsymbol{q})\right]^2 + \Phi_g(\mathbf{R}^M)\,, \tag{4.9}$$

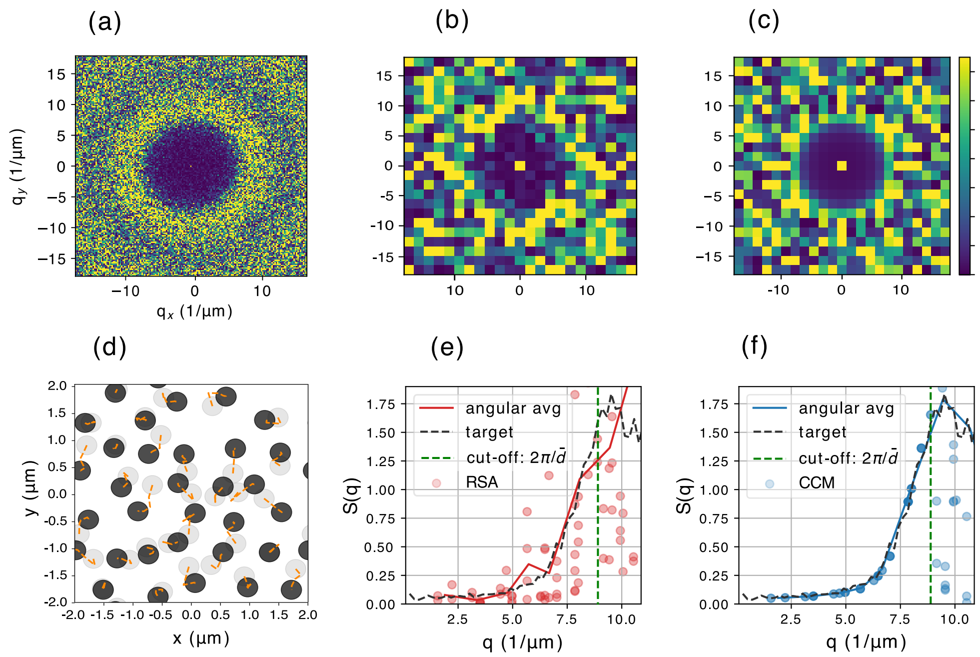

Figure 4.5: (a) $\tilde{S}_{\text{target}}(\boldsymbol{q})$ with $\rho_p = 2\ \mu\text{m}^{-2}$ and $r = 175$ nm. (b)-(c) $\tilde{S}(\boldsymbol{q})$ before (b) and after (c) CCM-optimization of the RSA sample. (d) Representative image of a $4 \times 4\ \mu\text{m}^2$ particle distribution re-arranged using the CCM-optimization. Light-gray circles show the initial RSA disk positions, while the black circles show the final pattern. Orange lines indicate the path traced by each disk during multiple iterations of optimization and periodization. (e)-(f) Angular-averaged structure factor in comparison to that of the large target sample. Adapted from Ref. [P2] with permission from © Optica Publishing Group.

where $\tilde{S}_{\text{target}}(\boldsymbol{q})$, the structure factor of the large target sample, is computed using:

$$\tilde{S}_{\text{target}}(\boldsymbol{q}) = \frac{1}{N} \left| \sum_{i}^{N} e^{-\mathrm{i}\boldsymbol{q}\cdot\mathcal{R}_i} \right|^2 . \tag{4.10}$$

The optimization region is defined as $\Omega = [0, 2\pi/\bar{d}]$. The function Φ_g is given by Eq. 2.99, and it serves the purpose of preventing particle overlap within the simulation domain $\mathcal{V}$ and on the periodic boundaries $\partial\mathcal{V}$. This approach ensures that the correlation length of the small domain pattern extends beyond its spatial boundaries, making it representative of the large-scale sample. The samples obtained from such an optimization are here onwards referred to as ‘CCM-optimized samples’.

The target particle distribution $\mathcal{R}^N$ and its corresponding structure factor $\tilde{S}_{\text{target}}$ that we are interested in, comes from a large-scale RSA point distribution. The method for generating such a particle distribution is explained in Sec. 4.2.3. The reason for choosing RSA point distribution is because, as seen in Sec. 4.4, this offers a good alternative to the stealthy hyperuniform systems (periodic or stealthy disordered) in the context of solar cells. Moreover, being a process that is representative of a self-organizing fabrication process, the resulting metasurface can be realized in a cost-effective manner with standard equipments [129]. Because the optimized samples should resemble the optical properties of such large-scale experimental samples, they must incorporate a sufficient amount of long-range information. To achieve this, a 15 × 15 μm^2 sample with the desired particle density and disk diameter is generated and used as a reference for the smaller samples. This approach allows the introduction of information about the long-range spatial correlation in the statistical properties of the pattern to a much smaller sample.

Other than comparing the optical properties of the CCM-samples with the large-scale target sample, it is also necessary to compare it to a small scale RSA sample. For this, many unique point distributions using the RSA algorithm are generated for full-wave numerical simulations. They are hereafter referred to as “RSA samples.” The ensemble-averaged simulation results derived from these smaller-sized samples are then compared to the results from a single simulation of a large sample.

It is important to note that while periodic structures are stealthy hyperuniform, the structures under consideration here do not inherit their long-range response from the periodic boundaries. This is because imposing periodic boundaries for a sample with a spatial extent of L allows us to probe the target structure factor at wave-vectors corresponding to the Bragg peaks of the periodic arrangement (i.e., at multiples of $q = 2\pi/L$). Structure factors for wave-vectors between these discrete points do not need to be resolved, as a sampling rate of $L/2\pi$ in reciprocal space is sufficient to capture all the spatial information contained within a spatial extent of L. Therefore, as long as this sampling rate is adequate to resolve all the characteristic features of the target sample, the periodic boundaries will not affect the preservation of the long-range response.

The re-shuffling of particles resulting from the optimization procedure is depicted in Fig. 4.5(d), along with the trajectory followed by each point during the optimization process. The target structure factor, obtained from a large sample used for optimization, is presented in Fig. 4.5(a). It is important to note that the traced paths (indicated in orange) are not straight lines but exhibit erratic changes in direction. This behavior is a consequence of the periodization and the rejection of solutions involving overlapping particles.

Figures 4.5(b) and (c) show the structure factor of the sample before and after the optimization process, while Figs. 4.5(e) and (f) present their corresponding angular-averaged characteristics. Notably, the scattering response after optimization in the $q_x q_y$-plane is highly isotropic, as evident from the scattered points in Figs. 4.5(e) and (f). These points are binned based on their corresponding $|q|$ for each (q_x, q_y). Figures 4.5(e) and (f) reveal very low $\tilde{S}(\boldsymbol{q})$ values achieved for small wave vectors in both the RSA and CCM optimized samples, with $\tilde{S}(\boldsymbol{q})$ approaching zero as $q \to 0$. The CCM optimized samples exhibit less noise in this limit. The features observed for the CCM pattern are indicative of nearly-hyperuniform arrangements, affirming the benefits of the optimization. Further insights can be gained by analyzing the angular-averaged structure factor for the CCM and RSA

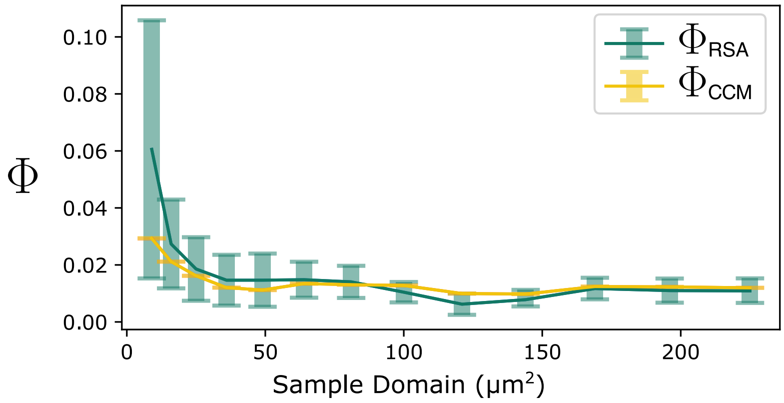

Figure 4.6: Objective function Φ as a function of increasing sample area for $\rho_p = 2\ \mu\mathrm{m}^{-2}$ and radius $r = 175$ nm. The error bars show the standard deviation from 10 samples.

samples in comparison to the target sample, considering varying spatial extents of the sample L. This analysis can be facilitated using an objective function defined as:

$$\Phi = \sum_{q \in \Omega'} \left[\tilde{S}(q) - \tilde{S}_{\mathrm{target}}(q) \right]^2 \tag{4.11}$$

where $\tilde{S}(q)$ and $\tilde{S}_{\mathrm{target}}(q)$ are now the angular-averaged quantities obtained from their respective 2D counterparts and $\Omega' = [q_i, q_f]$. The bounds, $q_i = 2\pi/(3\ \mu\mathrm{m})$ and $q_f = 2\pi/\bar{d}$ for the summation are fixed for varying domain size so as to always calculate a fixed energy in the reciprocal space. A value of $\Phi_s \longrightarrow 0$ then implies the angular-averaged structure factor agreeing well with the target.

Figure 4.6 illustrates the ensemble-averaged Φ_s as a function of the spatial area of the sample, given the particle density of $\rho_p = 2\ \mu\mathrm{m}^{-2}$ and a radius of $r = 175$ nm for 10 samples of each disorder type. Notably, the CCM optimization for large samples containing several hundred particles was made feasible solely due to the differentiability of our algorithm. It is evident that both the RSA and CCM samples provide accurate predictions of the target for various sample sizes. However, the RSA samples exhibit a relatively high standard deviation for smaller samples, which gradually decreases with increasing area. This behavior arises because the presence of hundreds of particles in the sample already constitutes an averaged response. Conversely, samples with optimized structure factors exhibit significantly lower standard deviation across multiple samples for all domain sizes.

The initial particle arrangement for the optimization is chosen as an RSA-type pattern in this case but is not limited to it. The approach is equally applicable to arbitrary initialization choices, as discussed in detail in Sec. 4.5.2. The primary criterion for the optimization is that the structure factor of a large target sample can be probed with a smaller sampling frequency (i.e., a smaller sample) without compromising the characteristic scattering features from the target. This is possible as long as $\tilde{S}(\boldsymbol{q} \longrightarrow 0)$ does not diverge. It is evident

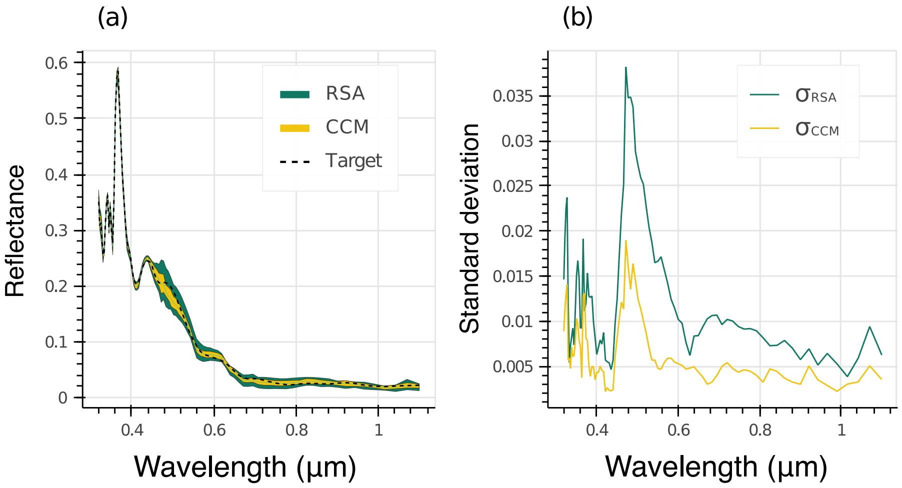

Figure 4.7: a) Mean reflectance of 2×2 μm^2, $\rho_p = 4\ \mu m^{-2}$ RSA and CCM-optimized patterns, averaged over ten samples each. The error bands are shown with 2σ standard deviation. The black curve is the reflectance obtained from a $15 \times 15\ \mu m^2$ RSA target sample for reference. b) Standard deviations of both sample types. Adapted from Ref. [P2] with permission from © Optica Publishing Group.

that such an optimization strategy may find applications in other types of correlated disorders and could be a subject of further research. In the next subsection, we study the optical properties of these structures with FDTD simulations.

4.5.2 Reflectance

Total, diffuse and specular reflection of a $2 \times 2\ \mu m^2$ cell

The initial set of simulations was conducted using a domain size of $2 \times 2\ \mu m^2$ with the geometrical parameters, $h = 160$ nm, $d = 350$ nm, and $\bar{d} = 500$ nm (i.e., particle density $\rho_p = 4\ \mu m^{-2}$). These are obtained from the hyperparameter optimization of an infinite square lattice geometry, described in Sec. 4.3.2. The resulting reflectance curves represent a typical silicon solar cell incorporating the nearly-hyperuniform TiO_2 nanodisk metasurface [126]. Selecting such a small sample size was deliberate for this preliminary investigation, as it provides insights into the level of variation in the anti-reflective capability arising from fluctuations in the particle arrangement's statistics. In reciprocal space, this corresponds to a spatial frequency of $2\pi/(2\ \mu m)$, which is considerably smaller compared to the characteristic spatial frequency associated with the typical nearest-neighbor distance: $2\pi/\bar{d} = 12.566\ \mu m^{-1}$ for a particle density of $4\ \mu m^{-2}$. Under these conditions, the sample contains a sufficient number of particles to yield a response somewhat representative of a target structure, while still being sparse enough to benefit from the optimization of its scattering response.

Figures 4.7(a) and 4.7(b) depict the mean spectral reflectances and standard deviations for the specified geometrical parameters, respectively. The responses from both the RSA and CCM-optimized structures were averaged over ten samples each. Additionally, the reflectance of the larger 15 × 15 µm^2 target sample is provided for reference. This larger sample size was chosen to ensure a reasonable number of particles in the sample, approximately 900, allowing for effective averaging over numerous potential particle configurations. Furthermore, this size limit was determined based on the practical constraints of simulating a 15 × 15 µm^2 sample using the available computational resources and FDTD simulation methodology.

The TiO_2 nanodisk layer with its tailored disorder arrangement demonstrates its effectiveness in light management by offering broadband reflectance suppression, particularly at longer wavelengths. This is not surprising since Sec. 4.4 already justified the use of hyperuniform structures for solar cells. In this long-wavelength spectral region, the Born approximation provides insight into the reduced total reflection (specular and diffused) resulting from the diminishing target structure factor, $\tilde{S}(\boldsymbol{q})$. The relatively high reflectance observed at shorter wavelengths, which includes the prominent peak at $\lambda_0 = 380$ nm, primarily arises from the high refractive index of cSi in this range. This high refractive index discrepancy between cSi and TiO_2 at shorter wavelengths leads to a significant impedance mismatch, causing increased reflection. In the visible spectrum, where the wavelength range approximately corresponds to the mean inter-particle distance $\bar{d} = 500$ nm, the elevated reflectance can be attributed to enhanced diffused reflection, which is expected due to the large values of $\tilde{S}(\boldsymbol{q})$ in this wavelength range. In contrast, at longer wavelengths, light interacts with the nanodisk metasurface as if it were an effective medium, resulting in both suppressed diffused and specular reflection.

The averages of both the CCM-optimized and RSA samples closely match the response of the 15 × 15 µm^2 target sample on all of the optical features meantioned above. Therefore, averaging the results over multiple realizations of the same disordered samples effectively reproduces the response obtained from a single large-scale simulation. However, a critical observation in the context of this study is the substantial difference in the reflection standard deviation between the RSA and CCM-optimized samples across the entire spectral range. This distinction is illustrated in the filled region in Fig. 4.7(a) and is more detailed in Fig. 4.7(b). The significantly larger standard deviation observed in the RSA samples from 450 nm to 700 nm is primarily due to the randomness in the individual particle arrangements within the ensemble. This effect is mostly pronounced around $\lambda \approx \bar{d} = 500$ nm, where the particle arrays are maximally diffracting. Scattering at wavelengths shorter than the mean inter-particle distance $\bar{d}$ is primarily influenced by the form factor of the individual disks rather than the arrangement statistics, resulting in minimal fluctuations for both sample sets. Similarly, for wavelengths longer than the particle diameter and mean inter-particle distance, the TiO_2 structures behave like a weakly-diffracting effective material layer. In this regime, the system relies less on the actual particle distribution within the sample and more on the samples having the same particle density, resulting in a low standard deviation. Qualitatively, CCM-optimized samples demonstrate statistical stability within the specified spectral range, even when describing the disordered interface

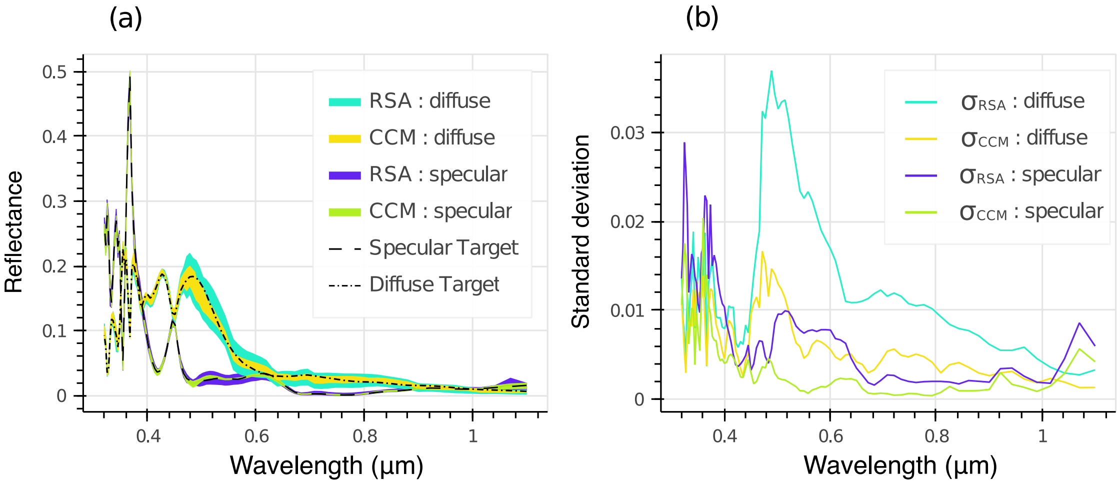

Figure 4.8: a) Decomposition of reflectance into specular and diffused components for 2×2 µm^2, $\rho_p = 4$ µm^{-2} samples. Error bands show 2σ standard deviation. Black markers display the respective reflectance shares obtained from a 15×15 µm^2 RSA sample for reference. b) Absolute standard deviations of the individual components shown in detail.

with only a few particles.

Figure 4.8(a) shows the total reflectance decomposition from Fig. 4.7 into its specular and diffuse components for both sample types, with their respective standard deviation shown as error bands. Similar to the case above, all values are averaged over ten samples each. The corresponding standard deviations can be seen in detail in Fig. 4.8(b).

The mean values of individual components for both sample types closely match the response of the larger 15×15 µm^2 sample. Notably, the most significant source of statistical deviation is observed in the diffused component for both sample types. This outcome is expected since different particle arrangements primarily affect the coupling of light into multiple diffraction channels. Conversely, particle density predominantly influences the specular component for all samples in the set.

Figure 4.8(b) clearly shows the low standard deviation in the diffused and specular components for CCM-optimized samples across the entire spectral range. This result can be understood by examining the structure factor presented in Fig. 4.5. As the optimized samples are all tailored to the same angular-independent target structure factor $\tilde{S}_{\text{target}}(\boldsymbol{q})$, they exhibit similar isotropic behavior for the scattered power (both diffused and specular) in reciprocal space for wave-vectors $k < 2\pi/(500\text{ nm})$. This uniformity in the reciprocal space properties contributes to the low standard deviation observed in both the diffused and specular components across the spectral range.

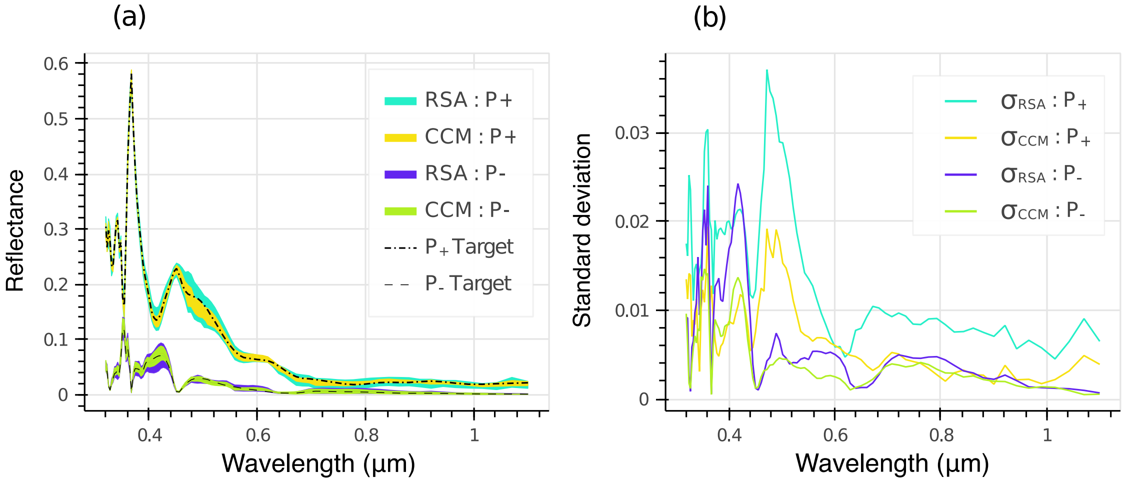

Figure 4.9: a) Total reflectance for 2 × 2 µm^2, ρ_p = 4 µm^{-2} samples broken down into their positive and negative helicity components. Error bands show 2σ standard deviation. Black markers display the respective reflectance shares obtained from a 15 × 15 µm^2 RSA sample for reference. b) Absolute standard deviations of the individual components in detail.

Decomposition into helicity components

As discussed in Sec. 4.4, the choice of hyperuniform disorder for the metasurface is strongly motivated by the effective continuous rotational symmetry ($C_{n\rightarrow\infty}$) and the suppressed scattering in the long-wavelength limit. From the helicity-preservation perspective, these properties then ensured zero specular backscattering in the range where the system is mostly sub-wavelength [P3, 30]. It is then worthwhile to see if the CCM-generated samples actually possess the same helicity-preserving properties compared to the large-scale RSA sample.

The decomposition of reflectance spectra from Fig. 4.7 into their helicity components is shown in Fig. 4.9(a). Similar to the results reported in Fig. 4.4, the positive (P_+) component, where helicity was flipped, contributes the largest share to the total reflectance for $\lambda > \bar{d} = 500$ nm. This is due to the suppressed diffuse reflection in this spectral region and the nanodisk arrangement approaching an overall $C_{n\rightarrow\infty}$ symmetry as a result of the long-range uniformity of both CCM-optimized and RSA samples. Figure 4.9(b) provides a more detailed view of the associated standard deviations for both RSA and CCM-optimized samples. As illustrated in Fig. 4.8(b), individual samples within both sample types primarily differ in their diffusive characteristics while maintaining their specular, long-range features. This suggests that both sample types are equally effective in achieving suppressed backscattering for wavelengths significantly longer than the mean inter-particle distance $\bar{d}$ = 500 nm due to the similar standard deviation in the unchanged helicity component P_- (indicated by the purple and green curves). The observed fluctuations are predominantly present in the opposite component P_+ (shown by blue and yellow curves). Consequently, a significantly smaller standard deviation in the P_+ component is noted for the CCM-optimized ensemble in the visible spectrum for wavelengths greater than $\bar{d} = 500$ nm. This reduced standard deviation in the P_+ component correlates with the similarly decreased standard deviation in the diffuse reflectance within this spectral range.

Choice of initialization

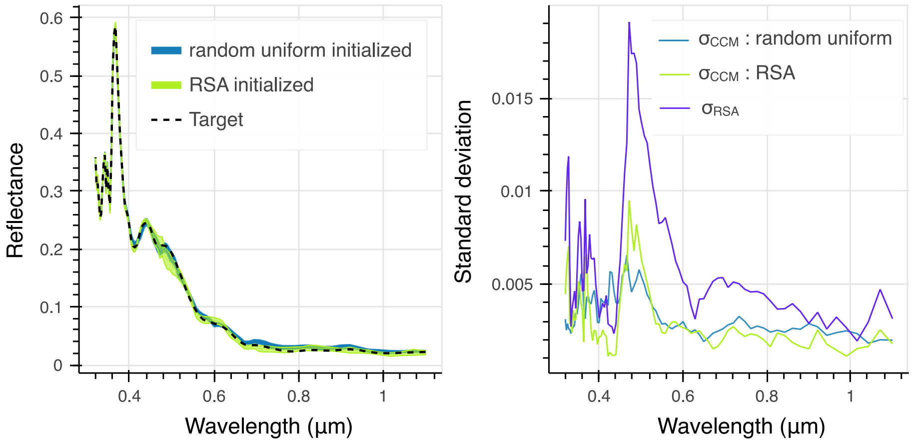

Figure 4.10: a) Mean reflectance of 2×2 µm^2, $\rho_p = 4$ µm^{-2} CCM-optimized patterns obtained from different initialization averaged over ten samples each. Error bands are shown with 2σ standard deviation. The black curve is the reflectance obtained from a 15×15 µm^2 RSA sample for reference. b) Standard deviations of both sample types shown in detail.

As mentioned in Sec. 4.5.1, the initialization for the optimization was chosen to already by a small scale RSA pattern. However, it must be noted that the optimization and its results are not influenced by the specific choice of the initialization. This is because there exists no unique solution for this many-particle minimization problem and each derived arrangement obeying the pair-correlation constraints would anyhow possess similar optical properties. To illustrate this, Fig. 4.10 compares the reflectance obtained from CCM-optimized samples with two completely different initialized particle patterns. The figure demonstrates that the predicted mean reflectance is comparable to the result from the larger 15×15 µm^2 sample, and the standard deviations for different initializations are quite similar across the spectral region of interest. This indicates the robustness of the method and its ability to reliably predict optical properties.

4.5.3 Photocurrent loss

For a more quantitative understanding of the use of the CCM, and to better understand the standard deviation in the reflectances shown above, we evaluate the photovoltaic response of the CCM-optimized and RSA samples by measuring the reflected photocurrent J_R using Eq. 2.76.

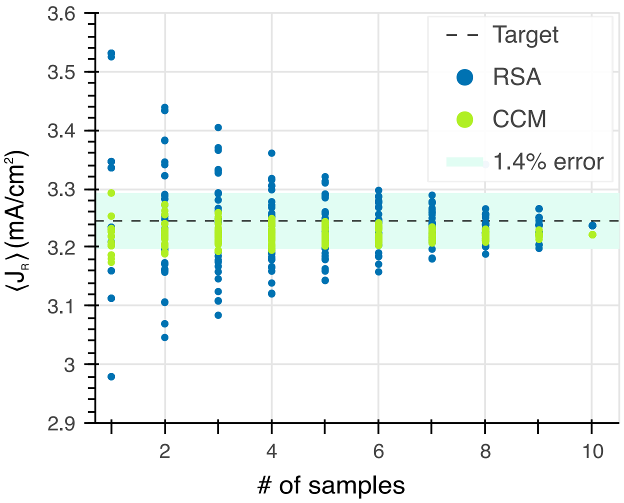

Figure 4.11: Mean reflected photocurrents of 2 × 2 μm^2, ρ_p = 4 μm^{-2} RSA and CCM-optimized patterns for a varying number of samples used for the ensemble-average. The dashed black line represents the current loss from the 15×15 μm^2 sample while each colored point represents a mean calculated from fixed number of randomly drawn samples.

To better understand the impact of ensemble-averaging over multiple pattern realizations, we calculate the mean current loss from an arbitrary selection of samples drawn from the generated data of ten samples. Figure 4.11 shows the mean current loss for varying numbers of samples chosen for the ensemble average, where each blue and green point on the figure represents the mean calculated from a fixed number of randomly drawn samples of types RSA and CCM-optimized, respectively. We clearly see that even a single CCM-optimized sample is sufficient to estimate the response from a larger 15 × 15 μm^2 sample (shown by the dashed black line) up to an error of 1.4%. For an equivalent error, the results from the RSA samples would have to be averaged over 7 samples, which would correspond to more than 7 times the overall simulation run-time.

Next, we examine the impact of a change in particle density (ρ_p) on the overall statistics of the sample types while keeping the simulation domain size and other nanodisk parameters constant. We simulate ten particle configurations for each sample type and particle density using FDTD. The results are shown in Fig. 4.12. As anticipated, when the particle density is small, the reflected photocurrent (J_R) is significantly higher. This is because, for smaller particle densities, the light trapping properties of the nanodisk metasurface shifts to longer wavelength where solar irradiation is less intense.

The optimal particle density, where J_R is minimized, is found to be around ρ_p = 4 μm^{-2}. This value aligns with what we observed in earlier discussions related to periodic lattice optimization, emphasizing the effectiveness of utilizing hyperuniform disordered structures. It is important to note that increasing particle density beyond approximately 4.5 μm^{-2} can lead to challenges in the particle arrangement process, as it leaves very limited space

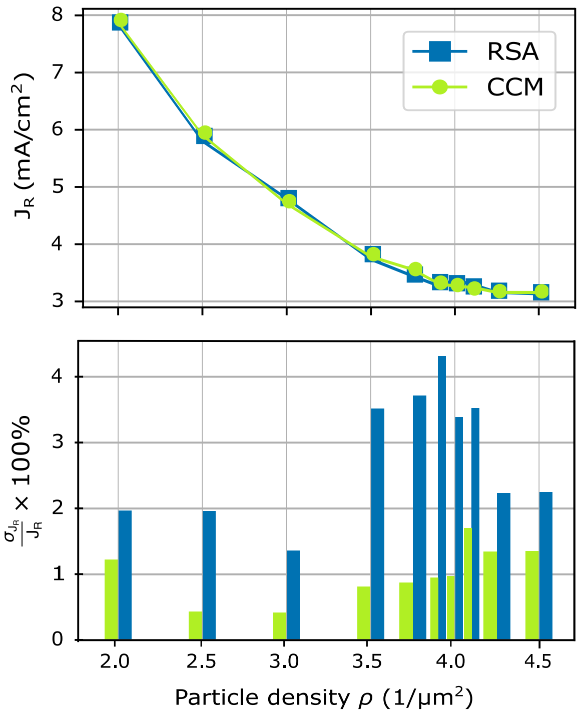

Figure 4.12: Mean reflected photocurrents of 3×3 μm^2 RSA and CCM-optimized patterns across varying particle densities averaged over ten samples, each shown by the line curves. The bar chart shows the relative standard deviations.

for sequential adsorption. Moreover, the filling fraction, given by $FF = \pi(r/\bar{d})^2$, is large enough to allow severe aggregation of particles in the system. This implies enhanced higher-order multipolar interactions that are not captured in the first-order approximated structure factor used for CCM optimization and is, therefore, outside the scope of this work.

While the ensemble-averaged reflectance curves in Fig. 4.7 already demonstrate good agreement in their corresponding current losses, as evident in the line chart in Fig. 4.12, a closer look at the relative standard deviation among these samples, as depicted in the bar chart in Fig. 4.12, reveals a significant insight. The relative standard deviation of the CCM-optimized samples consistently remains lower than that of their RSA counterparts across all particle densities. This distinction is particularly noteworthy for the optimal particle density $\rho_p = 4$ μm^{-2}, where the RSA samples exhibit a notably higher standard deviation. The significance of this finding lies in the spatial correlations within the system, where $\lambda \approx \bar{d}$ corresponds to the spectral region where the solar irradiance spectrum $\Phi_{\mathrm{AM1.5G}}(\lambda)$ reaches its maxima. In this region, even minor deviations in the inter-particle distances from $\bar{d}$ can have a pronounced effect on the system's diffusive scattering properties. This sensitivity is effectively captured by the RSA samples through ensemble averaging. In contrast, the CCM-optimized samples, having been optimized with a target structure factor, demonstrate isotropy in the resulting 2D-$\tilde{S}(\boldsymbol{q})$ for all samples, leading to similar diffusive characteristics around 500 nm. This results in a more precise prediction of the

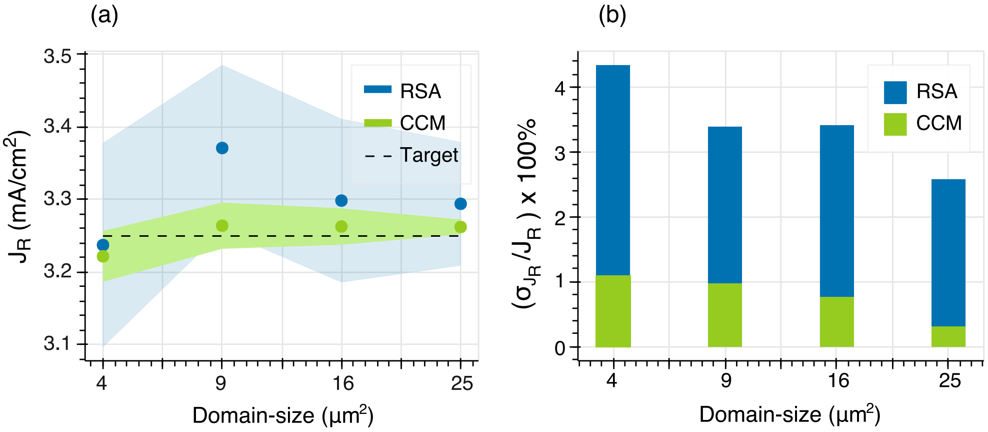

Figure 4.13: a) Mean reflected photocurrents of $\rho_p = 4\ \mu\text{m}^{-2}$ RSA and CCM-optimized patterns across different domain sizes, averaged over ten samples each. Error bars show 2σ worth of standard deviation. b) Relative standard deviations in detail.

mean spectra. In essence, this suggests that the utility of CCM for modeling small-scale disorder is not limited to optimal parameters but extends to arbitrary particle densities, emphasizing its robustness and versatility.

Both types of samples depicted in Fig. 4.12 exhibit a nominal increase in standard deviation as the particle density increases. For a fixed simulation domain size, lower densities inherently capture fewer long-range correlations, leading to more pronounced statistical deviation. However, lower particle densities shift the diffusive scattering response towards longer wavelengths, where solar irradiance is less intense. This shift has only a weak impact on the standard deviation of the calculated current loss. To further investigate this phenomenon, we maintain a constant particle density of $\rho_p = 4\ \mu\text{m}^{-2}$ now and examine the influence of various simulation domain sizes on the averaged reflected photocurrent J_R, averaging over ten samples each. A similar convergence study has been conducted for statistically uniform monolayers of spherical scatterers described by electric and magnetic dipoles, demonstrating good convergence with around 40 particles [131].

The results of these simulations are presented in Figs. 4.13(a) and (b). These figures reveal that the mean reflected photocurrent J_R is only weakly influenced by the spatial extent of the simulation domain for the CCM-optimized samples. Moreover, it becomes evident that both ensembles exhibit lower standard deviation as the domain size increases, as larger domains encompass more detailed long-range information owing to higher k-space resolution.

With minor fluctuations, both RSA and CCM-optimized samples average closely align with the current loss of the $15 \times 15\ \mu\text{m}^2$ target sample, which is approximately $3.25\ \text{mA}/\mu\text{m}^2$ across all domain sizes. In fact, the average of the CCM-optimized samples converges slightly closer to the target value, indicating that CCM-optimized samples are statistically more stable and more accurately resemble the features of larger-scale samples.

Furthermore, the standard deviation increases for smaller RSA samples. The relative standard deviations, illustrated in Fig. 4.13(b), provide a detailed view of this trend. Essentially, smaller samples sparsely sample the reciprocal space, which leads to more pronounced statistical fluctuations in the effective statistics of the disordered system. However, these statistical deviations are significantly reduced for the CCM-optimized samples across all sample sizes. Their predicted mean value is nearly independent of the domain size. These curves, in particular, very much highlight enhanced precision of the optimized samples in terms of agreement with the target sample and their superior statistical accuracy compared to their RSA counterparts.

4.6 Summary

In this chapter, we explored the extensive uses of the collective coordinate method (CCM) for generating particles distributions that are endowed with very unique light-scattering properties. Based on our modified version of the CCM, we show how a stealthy hyperuniform disordered metasurface clearly explains how complete suppression of single-scattering for a subset of wave vectors results in almost zero backscattering from a solar cell from the helicity preservation perspective. This argument also allowed us to consider an approximate, nearly hyperuniform RSA particle distribution that is more suitable for a large-scale fabrication routine through a self-assembly process.

In an effort to obtain more computationally feasible small scale simulation objects, we extended the applicability of the CCM beyond its conventional use. Our study demonstrated the reliability of the CCM for emulating the broad scattering features of a large-scale, many-particle sample in a small scale few-particle sample by minor collective displacements of the particles. Our findings indicate that the proposed approach of using few or even only a single CCM-optimized sample as a standalone simulation object for ensemble averages or a larger-scale sample yields a suitable response in studying optical properties of disordered metasurfaces in the context of light trapping in solar cells.

In Chap. 3, we studied how spatial properties of an inhomogeneous medium designed through Transformation Optics can be tailored for light trapping and anti-reflection in solar cells. In the current chapter, we looked at how the spatial arrangement of discrete particles can be tailored for light trapping and anti-reflection in solar cells. With the knowledge of these topics, we are now fully equipped for considering a more complicated metasurface whose particles are distributed in a nearly hyperuniform manner, and where the overall structure is conformally covered with several layers of varying refractive index. A "Graded Index metasurface" of this type can then capitalize on the excellent anti-reflection property of the inhomogeneous medium as well as the excellent light trapping property of the hyperuniform disorder. Such a system is experimentally and numerically investigated in the next chapter.

5 Anti-reflective gradient index metasurface for silicon solar cells

In this chapter, we combine the knowledge of designing an inhomogeneous media using principles of transformation optics, and designing a disordered metasurface using statistical properties of a correlated disorder, to ultimately design a graded index metasurface with correlated disorder. This metasurface will then be integrated into a planar solar cell. After an introduction in Sec. 5.1, In Sec. 5.2, we describe the geometrical details that characterise the considered graded index metasurface and also describe the quantities used for assessing its optical performance. The geometrical parameters characterising a periodic graded index metasurface are optimized in Sec. 5.3. The optimal parameters obtained from here will then give insight on the parameter space that needs to be considered for the experimental realization of its nearly hyperuniform counterpart. Section 5.4 briefly discusses the experimental details for fabricating such a disordered graded index metasurface. Section 5.5 discusses the numerical and experimental optical measurements for the optimally performing disordered sample. Finally, we discuss the aggregated results from all the fabricated samples along with its numerical counterparts in Sec. 5.5.1. The contents of this chapter are mainly taken from [P4]. This project was carried out in close collaboration with Dr. Maria Gaudig from the Institute of Physics at the Martin-Luther-University, Halle-Wittenberg, who fabricated the solar cell samples with disordered graded index metasurface, disordered nanodisk array (with the gradient layers), and a planar one-dimensional GRIN coating. Additionally, she also did optical measurements for the fabricated samples.

5.1 Introduction

The quest for highly efficient solar cells is a pivotal endeavor in addressing future energy needs. Recent research efforts have made significant stride in developing innovative structures for the solar cells that improve light coupling for reducing reflection losses as well as light trapping for maximizing absorption [9]. While textured interfaces optically address this issue, they suffer from an increased surface recombination current due to the enlarged surface area from the texturing [15, 16]. An alternate to the texturing approach was suggested in Chap. 3 where we designed an all-dielectric graded-index nanostructure integrated on top of an unstructured, i.e., a planar, solar cell [P1]. The design involves transformation optics and conformally maps a given texture onto an equivalent structure with a planar interface. This procedure allowed us to derive an optically similar structure with a spatially inhomogeneous refractive index distribution whose spatial features can directly be linked to geometrical properties of the texture, thus giving a straightforward

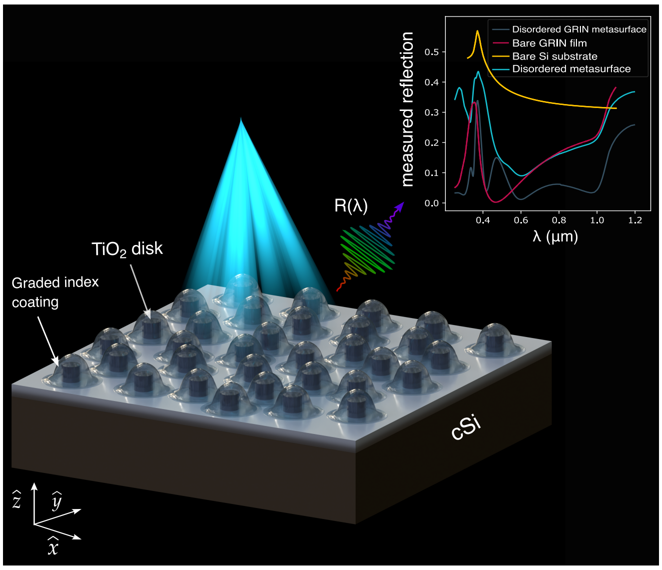

Figure 5.1: Artistic illustration of the light management structure considered here. The disordered GRIN metasurface consists of dielectric discs arranged in a nearly hyperuniform manner deposited on a polished silicon wafer. Then, a conformal graded-index coating above the disks is achieved by conformal deposition of layers with varying fractions of Al_2O_3 and TiO_2. The inset in the figure compares the reflection from such a device with an unstructured bare GRIN coating, disordered metasurface, and a bare Si substrate. Adapted from Ref. [P4] with permission from © John Wiley and Sons.

design methodology. However, this design methodology is only limited to two dimensions and cannot be used to design a full three-dimensional structure. This is because, according to Liouvilles' theorem, conformal maps in three dimensions are restricted to Möbius transformations, i.e., inversion, rotation, translation, and similarities [132, 133].

For generating a three-dimensional graded index structure with identical features as the two-dimensional transformation optics structure, the design strategy can come directly from the available large-scale fabrication techniques that would potentially be used to realise the final device. Such a design strategy will ensure that the actual design, and even the optimization, of the structures is done in the parameter space accessible in the fabrication process. Otherwise, the final structures would be too demanding or infeasible for fabrication. With the direct application of transformation optics, this would be barely possible.

The novel structures proposed here shall exhibit two distinctive features. Firstly, the light-scattering and light trapping characteristics that were originally in a textured interface, are present in the form of inhomogeneous material distribution at specific spatial frequencies in the lateral direction. Secondly, the broadband reflection suppression characteristics from a smoothly varying graded-index coating are present in the form of a graded-index material in the normal direction. The state-of-the-art considered here for lateral structuring, involves a self-organization process that arranges high-index nanodisks in a nearly hyperuniform disordered pattern atop the absorber, as previously described in Sec. 4.2.3, and in other references [23, 129]. To achieve the desired gradient-index (GRIN) profile on top of these nanodisks, we employ atomic layer deposition (ALD) to deposit a thin-film coating layer by layer, carefully adjusting the refractive index for each layer on the disordered pattern's surface. The resulting disordered GRIN metasurface, as depicted in Fig. 5.1, showcases remarkable reflectance suppression, as highlighted in the inset figure, especially when compared to reference structures. Our innovative design eliminates the necessity for a conformal transformation optics approach and simplifies the challenge of determining the optimal geometric features for both the metasurface and the covering graded-index profile.

In this work, we fabricate samples with various geometrical dimensions, perform optical characterization, and compare them to simulations. Our findings demonstrate that our disordered GRIN metasurface offers substantial back reflection suppression and enhances light trapping in a c-Si wafer, outperforming structures that employ only one of the two design strategies. While our focus in this study is on enhancing light management in solar cells, it is worth noting that these materials hold promise for various other applications as well.

5.2 Geometry and design parameterization for graded-index structure

5.2.1 Geometry and optical parameters

The considered layer structure consists of a conceptual solar cell geometry as shown in Fig. 5.2(a). A cSi substrate is used, with the upper half-space filled with air. To focus solely on assessing the anti-reflective properties of the structures, we simplify the model by disregarding reflections from the bottom interface into the simulation domain. This simplification is achieved by considering a semi-infinite lower half-space of cSi. To assess absorption within a finite wafer of thickness $L = 200\ \mu\mathrm{m}$, this cSi lower half-space is divided computationally into a thin absorbing region and a non-absorbing semi-infinite half-space, as depicted by the blue regions in Fig. 5.2(a). It is then ensured that the transmitted fields are always recorded by field field monitor within this non-absorbing semi-infinite half-space. These fields are then used to extrapolate on the absorption in the finite wafer of thickness $L = 200\ \mu\mathrm{m}$ using Eq. 2.80. For our particular geometry, this is given as

$$A(\lambda) = \mathcal{A}(\lambda) + \sum_{k_x,k_y} T(k_x, k_y, \lambda)(1 - e^{-\alpha_{cSi}(\lambda)L/\cos(\theta(k_x,k_y,k_z))}), \tag{5.1}$$

where the first term, $\mathcal{A}(\lambda) = 1 - R(\lambda) - T(\lambda)$ is the absorption in the thin cSi layer. While this distinction between an absorbing and non-absorbing cSi material is not ideal, it does not result in spurious reflections. At shorter wavelengths, cSi exhibits high absorption, and all absorption occurs exclusively within the absorbing layer. In this regime, the artificial interface remains inconspicuous to the incident light. Conversely, in the longer

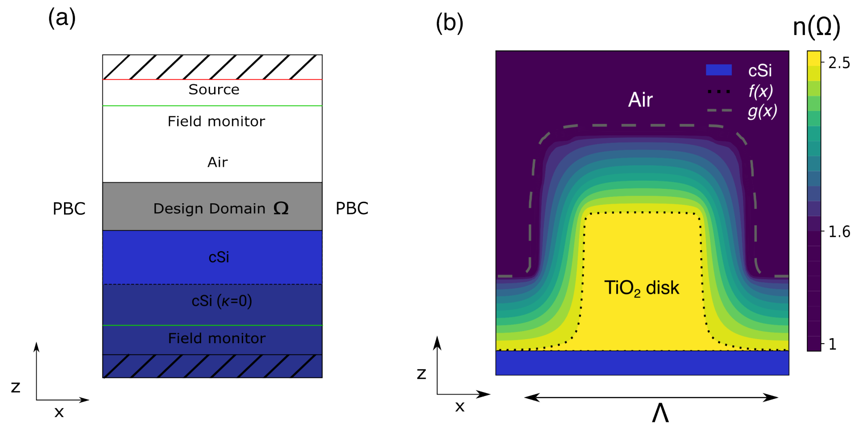

Figure 5.2: (a) Illustration of the geometry considered for the simulations. (b) Design domain for the GRIN metasurface shown with the refractive index distribution $n(\Omega)$ in the xz-plane.

wavelength range, where silicon demonstrates weaker absorption, the two layers exhibit minimal impedance mismatch, also leading to the absence of spurious reflections. The specular, diffused and total reflectance from the device is calculated using Eq. 4.5. The optical response for all the structures is evaluated using finite-difference time-domain (FDTD) simulation as implemented in Meep [75].

The design domain, shown in grey in Fig. 5.2(a), where the gradient AR coating or the TiO_2 nanodisks or its composite are to be studied are integrated just above the cSi layer. Dispersive material properties for the dielectric materials, as considered in the simulations, are taken from experimental measurements, whereas the properties for cSi are taken from the literature [92].

5.2.2 Design parameterization

Figure 5.2(b) shows the refractive index distribution $n(\Omega)$ obtained for our GRIN metasurface within the design domain Ω, and in the xz-plane. The conformal layers above the nanodisk vary in their refractive index based on the ratio of high refractive index material, TiO_2 and low refractive index material, Al_2O_3 deposited in the given layer. This constraint limits the upper and lower bounds for the refractive index at wavelength λ to be $n_{\mathrm{TiO_2}}(\lambda)$ and $n_{\mathrm{Al_2O_3}}(\lambda)$, respectively. The refractive index at a given point $\mathbf{r}$ in the design domain can then be written as

$$n_{\Omega}(\mathbf{r},\lambda) = n_{\mathrm{Al_2O_3}}(\lambda) + U(\mathbf{r})\left(n_{\mathrm{TiO_2}}(\lambda) - n_{\mathrm{Al_2O_3}}(\lambda)\right) , \tag{5.2}$$

where $U(\mathbf{r})$ represents a continuous design variable that linearly interpolates between the two given materials. The spatial distribution of this design variable is obtained by solving:

$$\nabla^2 u = u_{xx} + u_{zz} = 0 , \tag{5.3}$$

where $u = U(\mathbf{r})$ are the weights in the xz-plane with boundary conditions:

$$\begin{aligned} u(f(x)) &= 1 & u(g(x)) &= 0 \\ u_x(-\Lambda/2, z) &= 0 & u_x(\Lambda/2, z) &= 0\,, \end{aligned} \tag{5.4}$$

where Λ is the lattice constant (or mean-interparticle distance for disorder), respectively. The functions $f(x), g(x)$ define the shape of a single disk and the contour bounding the graded-index structure, respectively. These are shown in Fig. 5.2(b) with grey dashed line and black dotted line. The 2D Laplace's equation in Eq. 5.3 is numerically solved on a discrete grid within the boundaries defined by $f(x)$ and $g(x)$. This is done by solving the matrix equation [134]:

$$\boldsymbol{L}''\boldsymbol{\mathcal{U}}'' = \boldsymbol{B}''\,, \tag{5.5}$$

$$\boldsymbol{L}'' = \boldsymbol{L}' \odot \left(\boldsymbol{m} \otimes \boldsymbol{m}^{\mathrm{T}}\right)\,, \tag{5.6}$$

$$\boldsymbol{B}'' = \boldsymbol{B}' \odot \boldsymbol{m}\,, \quad \boldsymbol{\mathcal{U}}'' = \boldsymbol{\mathcal{U}} \odot \boldsymbol{m}\,, \tag{5.7}$$

where $\odot$ and $\otimes$ are Hadamard product and Kronecker product respectively. The primed quantities are given as:

$$\boldsymbol{L}' = \boldsymbol{F} + (\mathbb{I} - \boldsymbol{F})\boldsymbol{L}\,, \tag{5.8}$$

$$\boldsymbol{B}' = \boldsymbol{F}\boldsymbol{u}\,. \tag{5.9}$$

The operator $\boldsymbol{L} = \boldsymbol{D}_x^2 + \boldsymbol{D}_y^2$ is the second-order approximated Laplacian evaluated using finite-differences and $\boldsymbol{\mathcal{U}}$ is a column vector storing the values of $U(\mathbf{r})$ at discrete locations in space. $\boldsymbol{F}$ is a diagonal matrix with 1's in places that correspond to spatial locations with known value of $U(\mathbf{r})$ and 0's everywhere else. The values of $U(\mathbf{r})$ at these locations are stored in a column vector $\boldsymbol{u}$. The spatial locations with known values of $U(\mathbf{r})$ along with its values are given from the boundary conditions in Eq. 5.4. The column vector $\boldsymbol{m}$ is a mask with 1's in places where solution for Eq. 5.3 is desired and 0's where it is not. In this manner, Eqns. 5.5-5.7 ensure that the design variable $U(\mathbf{r})$ is only evaluated in the region enclosing $f(x)$ and $g(x)$. The continuous design variable $U(\mathbf{r})$ obtained from Eq. 5.5, will then ensure that $n_\Omega(\mathbf{r}, \lambda)$ contains equipotential surfaces with a constant refractive index above the disk. Each layer is then conformally stacked over subsequent layers with gradually varying indices along the normal and lateral directions. This refractive index distribution closely resembles the material distribution obtained from the ALD fabrication process.

At this point, it is worth emphasizing that, the inhomogeneous refractive index obtained above closely resembles the refractive index distribution obtained using a conformal transformation shown in Fig. 3.3. This is because, any transformation that satisfies Eq. 5.3 is naturally conformal [50]. It is then not very surprising that characteristic features in Fig. 5.2(b) resemble typical structures obtained using Transformation Optics for wavefront shaping in flat lenses [46, 135] and planarized parabolic reflectors [47, 136], and are also essential for light-trapping in our proposed structures [P1].

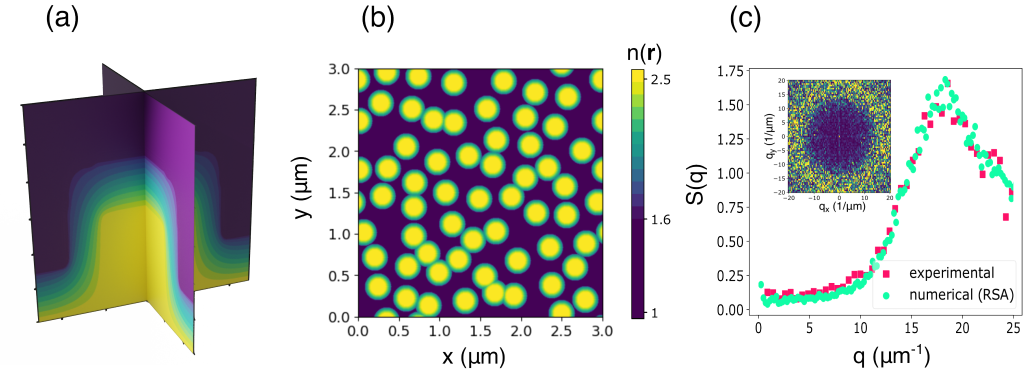

Figure 5.3: (a) Cross-sectional view (xz- and yz-plane) of the numerically generated structure with a GRIN coating. (b) Top view (xy-plane) of the disordered array with GRIN coating. (c) Angular-averaged structure factor $\tilde{S}(q)$ extracted from experiment compared to $S(q)$ of a simulated sample. The good agreement indicates the correct arrangement of the nanodisks in the simulations. The inset shows experimental $\tilde{S}(\boldsymbol{q})$ for the same sample in 2D.

Till now, the structure has been described exclusively in the two-dimensional xz-plane. To transform this two-dimensional profile into a three-dimensional material distribution, we split the design domain into two regions and generate the index profile separately in each region, following the equations:

$$n(x, y, z) = n(\rho \leq \Lambda, z) + n(\rho > \Lambda, z)\,, \tag{5.10}$$

where $\rho = \sqrt{x^2 + y^2}$. The first term, $n(\rho \leq \Lambda, z)$, rotates the above layer azimuthally around the rotation axis of the nanocylinders to get a single cylindrically symmetric scattering element, as shown in Fig. 5.3(a). The second term, $n(\rho > \Lambda, z)$, serves to guarantee the uniform deposition of the conformal index layer across the surface of the cSi wafer, extending beyond the cylindrically symmetric scatterers. This is necessary because the cylindrical symmetry is applicable only to the individual scatterers and not the entire structure as a whole. The resulting structure can now be used in an infinite square lattice. In the following subsection, we briefly describe the procedure for similarly generating a disordered structure.

5.2.3 Disordered system

For generating a disordered array of scatterers forming the metasurface, (Fig. 5.3(b)), we quantify their arrangement using the structure factor $\tilde{S}(\boldsymbol{q})$. First, we generate a large 30×30 μm^2 sample using a modified Random Sequential Adsorption (RSA) process, as described in Sec. 4.2.3. Figure 5.3(c) plots its angular averaged structure factor $\tilde{S}(q = |\boldsymbol{q}|)$ (light blue circles). Comparing $\tilde{S}(q)$ with experiment (pink squares), extracted from particle-center positions of SEM images, we find that numerically generated disordered arrays statistically correspond well with our experimentally achieved ones. Second, we use the CCM described in Sec. 2.4.2, and Chap. 4, for obtaining smaller samples feasible for a FDTD

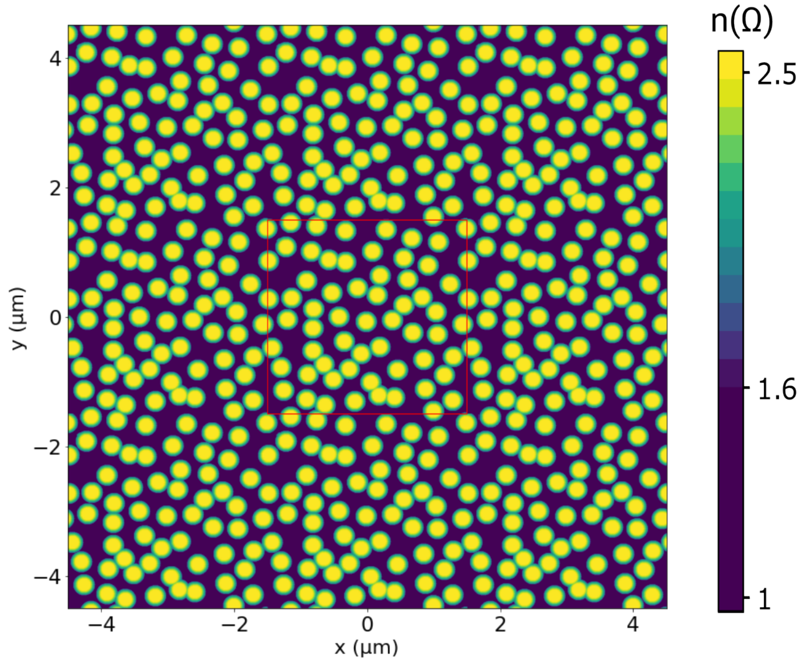

Figure 5.4: Illustration of periodic boundaries in a GRIN metasurface. The red box in the center comprises of a unit-cell used for the FDTD simulations.

simulation. To get a final material distribution that can be considered in simulations, each lattice coordinate is decorated with the previously identified refractive index distribution for an individual cylinder. Such graded-index structure is then integrated over prototypical solar cell geometry with crystalline Silicon (c-Si). From that point, it can be considered for further simulations.

Handling periodic boundaries and overlapping particles in simulations

The scatterers in the simulations avoid overlaps in the bulk and on the periodic boundaries due to the nature of the particle-generation algorithm [P2]. However, after integrating the gradient layers uniformly on the sample, the overlaps are no longer restricted, and aggregation of particles occurs more frequently, as also observed in SEM images of the fabricated samples. If unaccounted, these overlaps can lead to inaccurate and non-converging FDTD simulations due to periodicity condition not met on the boundaries or spurious scattering elements created in the system. We compute the material $n_{\text{eff}}(\mathbf{r}_0)$ at an overlapping point $\mathbf{r} = \mathbf{r}_0$ in volume $\mathcal{V}$ using

$$n_{\text{eff}}(\mathbf{r}_0) = \eta n_1(\mathbf{r}_0) + (1 - \eta) n_2(\mathbf{r}_0) \,, \tag{5.11}$$

where $n_1(\mathbf{r}_0)$ and $n_2(\mathbf{r}_0)$ are the refractive indices at a overlapping point. The value of η is decided based on the overlapping elements occuring inside the volume $\mathcal{V}$ or on the periodic boundaries $\partial\mathcal{V}$. Figure 5.4 shows the refractive index distribution in the simulations along the xy−plane at a certain height z_0 above the cSi-TiO$_2$. It can be seen that the scattering elements are correctly represented on the boundaries and inside the bulk. In the following section, we use the design parameterization developed here to find the optimal set of parameters which will then serve as a target for experimental realization of its disordered counterpart.

5.3 Parameter optimization

5.3.1 Optimization problem

The controllable parameters in our experiments include the height h, diameter d, and mean interparticle distance $\bar{d}$ of the nanodisks, as well as the GRIN coating thickness t. This allows us to fine-tune and optimize the light management characteristics of the disordered GRIN metasurfaces. To streamline the optimization process, we initially establish a simpler system with defined parameters that will serve as our target for the fabrication of the final metasurfaces. These target parameters are determined through systematic investigations involving periodic simulations with lattice constant Λ. In our subsequent disordered simulations, we replace the lattice constant with the mean interparticle distance (correlation length), keeping the other factors constant. This entire parameter set, denoted as $\mathbf{P} = [h, d, t, \Lambda]$, represents the optimization problem as follows:

$$\begin{aligned} &\min_{\mathbf{P}} J_{\mathrm{R}}(\mathbf{P}) = e \int_{320\ \mathrm{nm}}^{1100\ \mathrm{nm}} \Phi(\lambda) R(\mathbf{P}, \lambda) d\lambda \\ &\text{s.t } \boldsymbol{L}''(\mathbf{P}) \boldsymbol{\mathcal{U}}''(\mathbf{P}) = \boldsymbol{B}''(\mathbf{P}) , \end{aligned} \tag{5.12}$$

where $R(\mathbf{P}, \lambda)$ is the reflection spectrum obtained for the given set of parameters $\mathbf{P}$ and $J_{\mathrm{R}}(\mathbf{P})$ is simply the current loss. The constraint $\boldsymbol{L}'(\mathbf{P})\boldsymbol{U}(\mathbf{P}) = \boldsymbol{B}(\mathbf{P})$ essentially creates the gradient layer using the operator $\boldsymbol{L}'(\mathbf{P})$ given by Eq. 5.3 with the boundary conditions $B(\mathbf{P})$ given by Eq. 5.4. Similar to Sec. 4.3.1, these parameters are then fed to a hyperparameter search algorithm for minimizing $J_{\mathrm{R}}(\mathbf{P})$ [128].

5.3.2 Results

Figure 5.5 summarizes the results of the hyperparameter optimization in a parallel-coordinates plot. Each axis in the figure indicates the range of values for the corresponding parameter. This way, a single simulation run is identified with a line passing through each axis at points that correspond to the parameters considered for the simulation. In this figure, we present three types of structures: a periodic GRIN metasurface, a periodic nanodisk array, and a planar GRIN coating.

Given the nature of the optimization problem, it is crucial to distinguish between two distinct parameter spaces: one that considers the complete GRIN metasurface and another that does not, i.e., the bare nanodisk array without GRIN coating as well as the planar GRIN coating without nanodisks. This distinction is essential as it ensures that we strive for the optimum in each of these scenarios, which is a prerequisite for a fair evaluation of the advantages gained when combining nanodisks and GRIN coating to form a GRIN metasurface. To distinguish between each case, we employ various line styles,

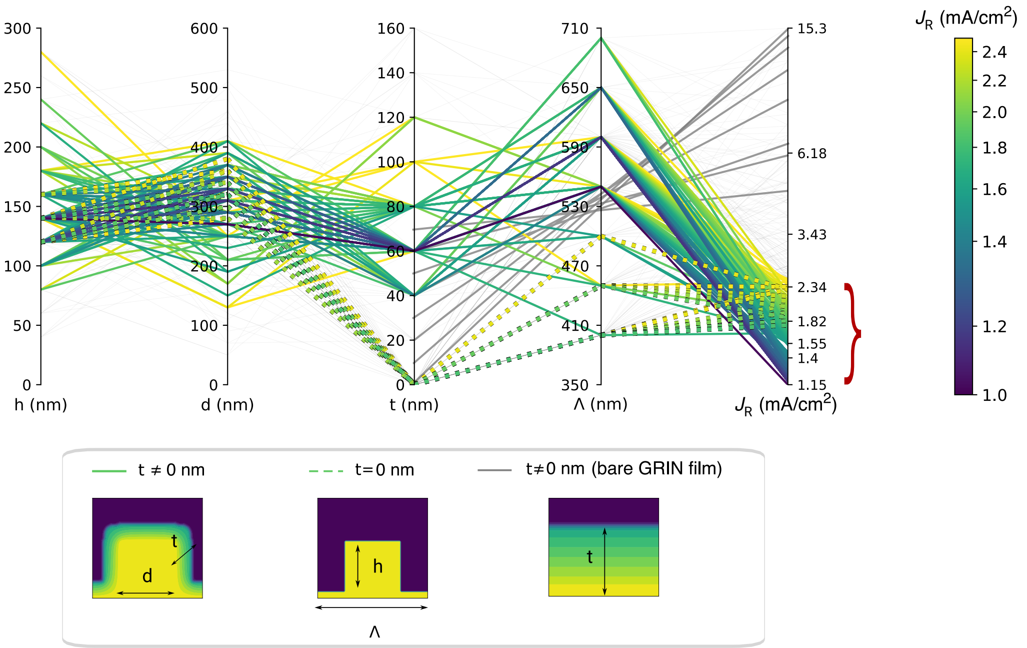

Figure 5.5: Parallel-coordinate representation of the optimization for minimizing reflected photocurrent J_R as a function of geometric parameters $\mathbf{P} = [h, d, t, \Lambda]$. Solid lines (colored and light grey) depict complete GRIN metasurfaces, dashed lines depict bare nanodisk arrays without GRIN coating, and solid dark grey lines depict bare GRIN coatings without nanodisks. Additionally, the colored lines represent parameter sets $\mathbf{P}$ for which broadband reflection is suppressed below $J_R = 2.5\,\text{mA/cm}^2$.

as specified in the figure caption and inset of Fig. 5.5. Additionally, we use color coding to indicate parameter sets represented by $\mathbf{P}$ that result in relatively low reflection losses ($J_R < 2.5$ mA/cm^2), while all other sets ($J_R > 2.5$ mA/cm^2) are shown in light grey. The former are selected as candidates for experimental sample fabrication.

The optimization results for the bare nanodisk array are shown by dashed lines passing through $t = 0$ nm. This dataset is also what is reported in Sec. 4.3.2. From these dashed lines, we see that by tuning the nanodisk parameters, and the lattice constant of the metasurface, the bare nanodisk array is already able to outperform the planar GRIN coatings, shown by solid dark grey lines.

The results for the periodic GRIN metasurfaces are shown by solid lines passing through $t \neq 0$. By optimizing the parameters of the gradient layers and the nanodisks, the GRIN metasurface is able to outperform the planar GRIN coatings as well as the bare nanodisk array. The minimal reflection currents are $J_R = 1.15$ mA/cm^2, $J_R = 4.26$ mA/cm^2, and $J_R = 1.80$ mA/cm^2, respectively. The gradient index coating of thickness $t = 60$ nm for the GRIN metasurface is found to be optimal in terms of minimizing broadband reflection. When we compare the performance trajectories of optimally-designed GRIN metasurfaces with those of optimally-designed bare nanodisk arrays, it becomes evident that the inclusion of a GRIN coating results in a reduced sensitivity of J_R to the remaining parameters, namely h, d, and Λ. In particular, we observe that there is only a limited range of parameter sets denoted by $\mathbf{P}$ with $t = 0$ nm (indicating no GRIN coating) that can achieve J_R values even comparable to those obtained with a GRIN coating of any given thickness t. This indicates that adding the conformal GRIN coating relaxes the requirements of very fine-tuned nanodisk filling fractions and heights. Indeed, we can confirm this trend when extending our studies to include nearly hyperuniform disorder. For this, please refer to Sec. 5.5.1.

Regarding bare GRIN coatings, it is apparent that with a continuous increase in thickness beyond the largest value depicted here ($t = 70$ nm), lower J_R values can be achieved. However, it is important to note that, as observed in the experiment (and as discussed in Sec. 5.5), this reduction in J_R does not necessarily translate to an increase in the useful absorbed photocurrent. This is because planar structures, like the bare GRIN coatings, cannot couple to scattering or diffraction channels, which are crucial for enhanced absorption in the near-infrared spectral range [10, 137].

The optimal parameter sets, denoted as $\mathbf{P}$, for GRIN metasurfaces and bare nanodisk arrays are notably distinct. One significant difference is the shift in the optimal lattice constant from $\Lambda = 0.4$ µm for bare nanodisks to $\Lambda = 0.55$ µm when a GRIN coating is introduced. Interestingly, the filling fraction, calculated as $\mathrm{FF} = \pi(d + 2t)^2/4\Lambda^2$, remains similar, if not exactly the same, for both cases. This highlights that the superior performance achieved with nanodisks combined with a GRIN coating cannot be trivially replicated by nanodisks alone with the same lattice constant. The parametric space, shown in Fig. 5.5, is used as a referential target in the experiments for fabrication. In the following section, the colleagues from the Univesity of Halle-Wittenberg fabricate these disordered metasurface samples with and without the GRIN coating, and also characterize them.

5.4 Experimental details

5.4.1 Correlated-disorder TiO_2 nanodisk arrays

The initial step involves fabricating disordered TiO_2 nanodisk arrays on a standard 200 µm floatzone silicon wafers with a sample area of 2×3 cm^2. This fabrication process is accomplished using our previously detailed self-organized colloid-based nanolithography technique [P3, 23]. Through this experimental approach, we have precise control over three critical structural parameters: the height (h), diameter (d), and mean center-to-center distance ($\bar{d}$) of the nanodisks. This way, both the experiment and the simulations are parameterized with the same variables. Figures 5.6(a) and (b) show scanning electron microscopy (SEM) images of fabricated nanodisk arrays on c-Si wafer with parameters [h, d, $\bar{d}$] = [152.5, 235, 461] nm before depositing the GRIN coating.

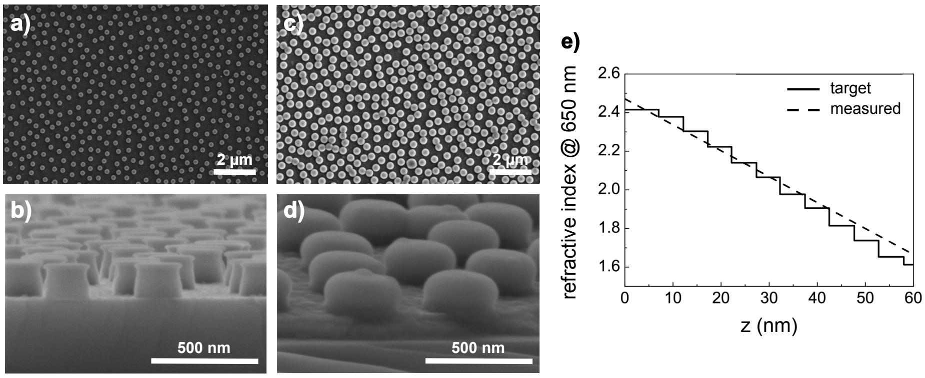

Figure 5.6: SEM images of nearly hyperuniform disordered TiO_2 nanodisks arrays (a,b) and (c,d) after deposition of the GRIN film (t = 60 nm), with parameters $[h, d, \bar{d}] = [152.5, 235, 461]$ nm. (e) Targeted refractive index profile (solid line) of a planar GRIN coating with t = 60 nm and the corresponding experimentally realized profile measured by spectroscopic ellipsometry (dashed line) at a wavelength of λ = 650 nm. The SEM images and the experimental data are taken by Dr. Maria Gaudig from the Institute of Physics, Martin-Luther-University Halle-Wittenberg. Adapted from Ref. [P4] with permission from © John Wiley and Sons.

5.4.2 Graded-index layer deposition

Following the fabrication of the disordered nanodisk array, a GRIN coating is applied to it. This is achieved through a sequential deposition process, where we successively add multiple ultrathin layers, each 5 nm in thickness. These layers consist of TiO_2 and Al_2O_3 with varying compositions, achieved using atomic layer deposition (ALD). The composition of each layer determines its refractive index, allowing us to create a multilayer coating with refractive index variations in increments of 5 nm. The refractive index of each ultrathin layer is precisely controlled by adjusting the ratio of Al_2O_3 to TiO_2 within that layer [138, 139]. This method enables the experimental creation of transparent GRIN coatings with a flexible and nearly continuously varying refractive index profile along the thickness t, satisfying the condition $n_{\mathrm{Al_2O_3}} \leq n(t) \leq n_{\mathrm{TiO_2}}$.

The index profile of the planar GRIN coating (t = 60 nm), consisting of 12 layers on a silicon wafer, is depicted in Fig. 5.6(e). This experimentally realized linear index profile, determined through spectroscopic ellipsometry, closely matches our target index profile. By modifying the material deposition ratios and sub-layer thicknesses, it is possible to create different polynomial index profiles, such as quadratic or cubic. Such polynomial profiles are well explored in literature for broadband AR coatings [24–26, 59]. However, our choice of this linear profile was substantiated by both theoretical simulations discussed in Sec.5.3 and also from practical constraints. Moreover, we anticipate that profiles of higher polynomial orders would only yield marginal changes in the overall broadband optical response of the final structure, including the nanodisk array.

Our disordered GRIN metasurfaces are produced by depositing GRIN coatings like the one shown in Fig. 5.6(e) onto the TiO_2 disordered nanodisk arrays. The SEM images in Figs. 5.6(c) and (d) display the resulting structure after applying a GRIN coating to the disordered nanodisk arrays shown in Figs. 5.6(a) and (b). In addition to the deposited GRIN coating with a thickness of t in the region between the nanodisks, we observe that the radius and height of the overgrown nanodisks have also increased by t. This observation suggests a successful conformal deposition onto the disordered nanodisk arrays, achieving the spatially varying index profile we aimed to create, both vertically and laterally. In the following section, we use these fabricated samples and study their optical properties. The results are also compared with the numerical simulations.

5.5 Optical response of disordered GRIN metasurfaces

The insights from the parametric optimization described above are directly fed into the experimental fabrication as target parameters. Additionally, we perform full-wave simulations of the disordered structures using FDTD, similar to the method described in Chap. 4. We use in-house image-processing for extracting the structure factors $S(q)$ from SEM images (field-of-view $80 \times 80\ \mu m^2$) of fabricated samples, a typical example is shown in Fig. 5.3(c). We use experimental $S(q)$'s as target structure factors $S(q)_{\mathrm{tar}}$ for realizing CCM samples of cross-section $3 \times 3\ \mu m^2$. Given the size of the nanodisks and the mean-interparticle distances considered here, the sample size of $3 \times 3\ \mu m^2$ was found sufficient to yield a good agreement with the experimental results.

5.5.1 Results and Discussion

In Fig. 5.7, we show the experimental optical response of our best-performing disordered GRIN metasurface, characterized by $\mathbf{P} = [h = 153, d = 234, t = 60, \bar{d} = 461]$ nm, alongside numerical simulations. To provide a comprehensive comparison, we also include the optical response of the disordered nanodisk array (without the GRIN coating), the bare GRIN coating, and the plain c-Si wafer. The measured reflectance, absorbance, and their corresponding photocurrents exhibit all the principal characteristics anticipated by our simulations, indicating the accuracy of our numerical approach for both the disordered nanodisk array and the disordered GRIN metasurface. Notable deviations from the simulations are observed solely for wavelengths $\lambda > 1\ \mu m$, where the measured reflectance for all samples increases due to rear side reflection. This rear-side reflection was not considered in our simulations. As a result, it leads to higher absorption in the wafer beyond the absorption of a single pass, thus rendering the measured absorption greater than our simulated values.

As anticipated, the presence of a GRIN coating enhances the absorption within the c-Si wafer while effectively suppressing back reflection in a broadband manner, as illustrated in Figs. 5.7(a) and (b). This effect is, unsurprisingly, observed for geometries with flat Si interface (yellow and magenta data) but also extends to the structured case (green data). In the latter scenario, the disordered GRIN metasurface not only increases absorption at

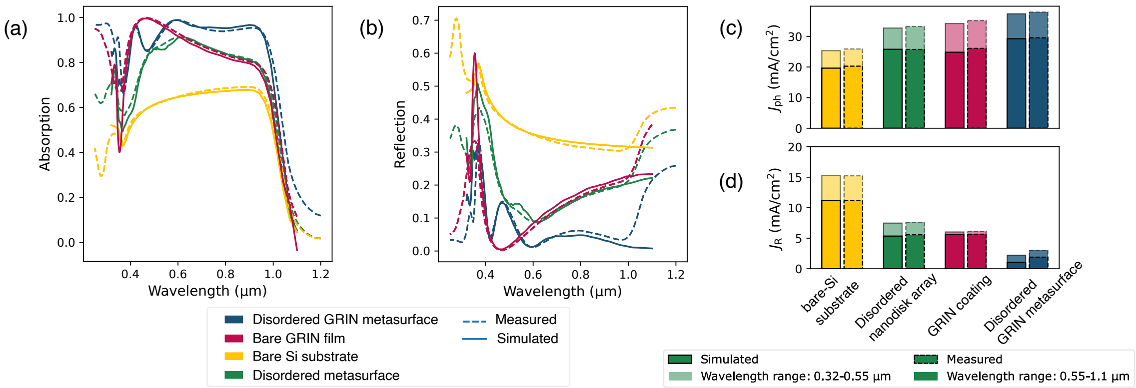

Figure 5.7: Experimental and simulated (a) absorption and (b) reflection spectra of a disordered GRIN metasurface with $\mathbf{P} = [153, 234, 60, 461]$ nm and the corresponding disordered bare nanodisk array, the bare GRIN coating and a bare Si substrate. (c) Absorbed and (d) reflected photocurrents J_R and J_{ph} for the same sample evaluated in different spectral regions respectively. The solid and dashed lines for each subfigure correspond to the experimentally measured and simulated result, respectively. Adapted from Ref. [P4] with permission from © John Wiley and Sons.

shorter wavelengths, a characteristic shared with the bare GRIN coating, but also at longer wavelengths. This outcome is consistent for the fabricated samples and the numerical results. To provide a more quantitative perspective, we can observe in Figs. 5.7(c) and (d) how the absorbed and reflected photocurrents J_R and J_{ph}, respectively, calculated using Eqns. 2.76 and 2.75, are decomposed into their respective contributions from the short and long spectral ranges.

In the wavelength range of $0.32 - 0.55$ µm, it is evident that individual scattering elements play a more substantial role in the overall response than the statistics of their arrangement for $\bar{d} = 461$ nm. This is primarily due to the spectral range being comparable to the mean interparticle distance. The current densities (both absorbed and reflected) of the fabricated samples agree well with the simulations, thus indicating the mean height and diameter of the deposited nanodisks and the thickness of the gradient layer coating match well with the simulated values. The anti-reflective attributes of the graded-index coating are most prominent in this spectral region, as the smooth refractive index transition minimizes the impedance mismatch between air and c-Si. Given the short absorption depth of silicon (< 2 µm) in this range, improved light incoupling suffices to enhance absorption, as illustrated by the lightly shaded bar plots for the bare GRIN coating and disordered GRIN metasurface (depicted in magenta and dark blue, respectively). In the subsequent wavelength range of $0.55 - 1.1$ µm, where correlated disorder plays a more significant role in overall scattering, the current densities of the fabricated disordered metasurface also correspond well with the simulations, indicating that the particle statistics from the experiments align closely with the simulated data.

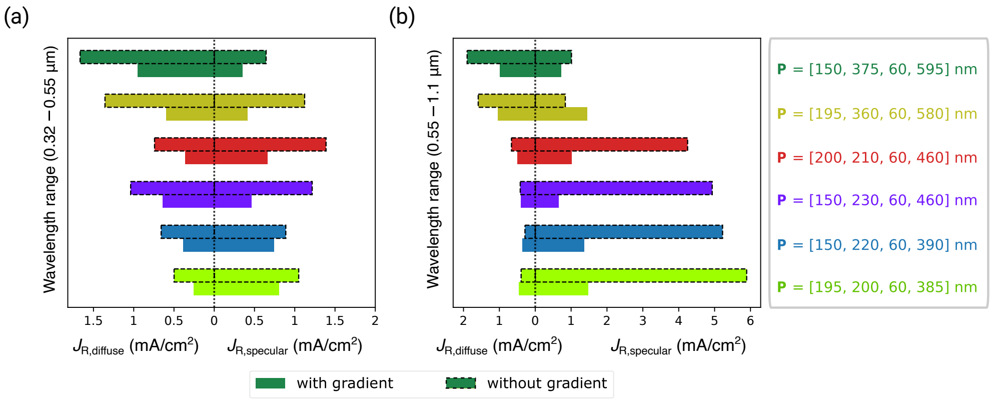

Figure 5.8: Decomposition of reflection losses J_{R} of disordered GRIN metasurfaces and bare disordered nanodisk arrays for (a) the wavelength range $0.32 - 0.55$ μm and (b) ($0.55 - 1.1$ μm). For each subfigure, the left-side bars represent contributions of diffused reflection whereas the right-side bars represent contributions of specular reflection. Each color represents a sample with different geometric parameters given by $\mathbf{P} = [h, d, t, \bar{d}]$. The solid and dashed bounding boxes indicate structures with and without the graded-index coating, respectively.

The superior optical properties of our disordered GRIN metasurface become apparent when examining not just a single fabricated sample but rather a range of samples with varying parameters. Figure 5.8 provides an overview of these properties across various parameter sets, decomposing the reflected photocurrent of the simulated nanodisk samples into its specular and diffused components for different spectral regions.

In the wavelength range of $0.32 - 0.55$ μm, the dominance of diffused back reflection becomes more prominent as the inter-particle distance increases. This is evident by the larger $J_{\mathrm{R,diffuse}}$ compared to $J_{\mathrm{R,specular}}$ as the mean interparticle distance ($\bar{d}$) increases from bottom to top in Fig. 5.8(a). In this spectral region, the wavelength is comparable to the mean interparticle distance, the height, and the diameter of the scatterers. The contribution to diffused back reflection is a result of both the individual scatterer responses and their disordered arrangement, as indicated by the large values of $S(\boldsymbol{q})$ for $q \approx 2\pi/\bar{d}$, as shown in Fig. 5.3(c).

Effective suppression of reflection for $\lambda < 0.45$ μm can be achieved by having a smoothly varying refractive index along the normal direction. However, for $0.45\ \mu\mathrm{m} \leq \lambda < 0.55$ μm, reflection suppression depends on lateral features, such as the dielectric nanodisks in the sample [114, 140]. Additionally, these lateral features contribute to enhanced light trapping by exciting higher diffraction orders in the absorbing layer, resulting in a longer optical path length. The GRIN disordered metasurface leverages both aspects by having a conformally varying refractive index along both the normal and lateral directions above the disordered nanodisks. Consequently, the reflectance of the GRIN disordered metasurface in this spectral region, as shown in Fig. 5.8(a), is reduced for both specular and diffused components. This reduction surpasses what is observed in its bare disordered nanodisk counterpart and holds true for all the geometric parameters presented in Fig. 5.8. Such features were also characteristic of the transformation optics structures investigated in Chap. 3 where the lateral variation in the index lead to enhanced absorption at longer wavelength [P1].

Conversely, for the wavelength range $0.55 - 1.1$ µm, the lateral features in the sample are not resolved by the incident wavelength, resulting in backscattering that is primarily limited to small angles. This is due to the nearly-hyperuniform particle arrangement, as shown in Fig. 5.3(c). In simpler terms, the suppressed density fluctuations at longer wavelengths ensured by the hyperuniformity, allows the system to effectively behave like a homogeneous medium [125]. This trend is also applicable to the disordered GRIN metasurface. This response is not anticipated from a bare GRIN coating with a similar thickness because it excels as an efficient in-coupler at shorter wavelengths. However, it loses this advantage in the longer wavelengths from the increased reflection. Interestingly, the same gradient layer coating, when considering the disordered GRIN metasurface, makes for a better effective medium in this spectral region compared to the bare nanodisk array or the bare GRIN coating. The disordered GRIN metasurface then clearly capitalizes on the advantageous properties of both the disordered nanodisk array and the GRIN coating. It acts as an efficient anti-reflective structure at both short and long wavelengths, while also functioning as an efficient light-trapping structure at longer wavelengths.

To gain a more comprehensive understanding of how the geometric parameters affect the overall performance of the disordered GRIN metasurface, we fabricate several of these metasurfaces with varying geometrical parameters and then compare their optical responses with simulations. The aggregated results of all the samples are shown in Fig. 5.9. It shows the photocurrent (reflected and absorbed) for all the samples, considering both those with and without a GRIN coating ($t = 60$ nm). We varied the height ($50 \text{ nm} \leq h \leq 210 \text{ nm}$), diameter ($130 \text{ nm} \leq d \leq 370 \text{ nm}$), and mean distance ($240 \text{ nm} \leq \bar{d} \leq 600 \text{ nm}$) for the samples. However, for the sake of simplicity, we chose to focus on the variation in diameter. The choice of the parametric range is well-justified by the hyper-parameter optimization results shown in Fig. 5.5.

We see a reasonable agreement between experimentally measured spectra (empty markers) and simulated spectra (same color, but with solid markers) for structures with and without the GRIN coating, not only for a single fabricated sample but rather for a wide range of parameter variations. We notice that, while the disordered nanodisk array manages to perform comparably to the bare GRIN coating for only a few specific parameter values, our proposed disordered GRIN metasurface consistently outperforms both alternative strategies for all the considered parameter combinations. This showcases its robustness to minor geometric variations, as already hinted at in the periodic simulations described earlier. In Figs. 5.9(c) and (d), we illustrate this robustness by comparing two different devices with parameters $\mathbf{P} = [153, 234, 60, 461]$ nm (shown in purple) and $\mathbf{P}' = [195, 361, 60, 577]$ nm (shown in olive green) in the top figure, along with their respective structures with $t = 0$ nm in the bottom figure.

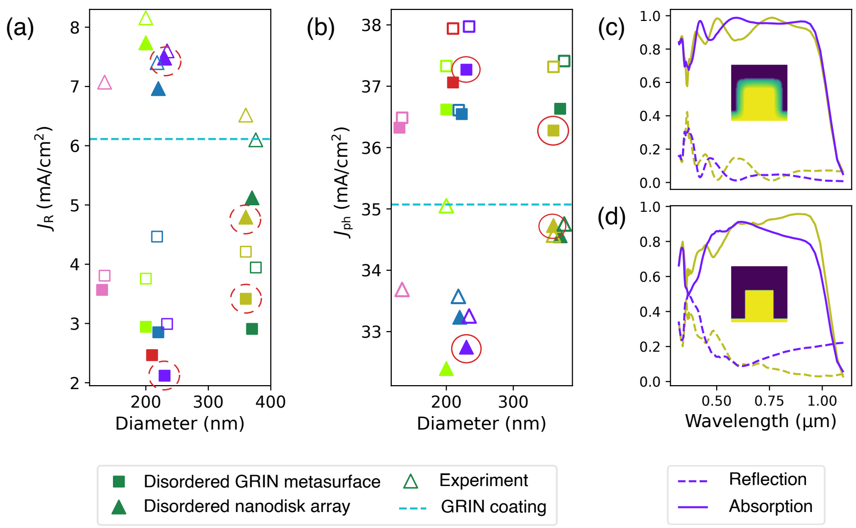

Figure 5.9: (a) Reflected and (b) absorbed photocurrent of samples for varying height, diameter, and particle density of the nanodisks. The empty and filled markers for a given color represent results from the experiments and simulations, respectively. The absorbed and reflected photocurrent were evaluated in the wavelength range $[0.32 - 1.1]$ μm. c) Simulated absorbance and reflectance spectrum represented by purple and olive green data points in (a) and (b) from a disordered GRIN metasurface with parameters, $\mathbf{P} = [153, 234, 60, 461]$ nm and $\mathbf{P}' = [195, 361, 60, 577]$ nm, respectively. d) Spectra with the same parameters as in c) but with $t = 0$ nm.

For the disordered GRIN metasurface, both the purple and olive devices have comparable scattering features. As result, these devices have comparable photocurrents, such that $\Delta J_{\mathrm{ph}} \approx 0.95$ mA/cm^2 for the simulated results. In contrast, this is not the case for the disordered bare nanodisk array. The absorption and reflection spectrum for the purple and olive devices have notably different scattering features because of which $\Delta J_{\mathrm{ph}} \approx 2.05$ mA/cm^2 for the simulated results. Of course, this trend can also be seen in the reflected current, such that $\Delta J_{\mathrm{R}} \approx 1.2$ mA/cm^2 and $\Delta J_{\mathrm{R}} \approx 2.7$ mA/cm^2 for the disordered GRIN metasurface and bare nanodisk array, respectively.

5.6 Summary

In this chapter, we investigated an approach for light-trapping that exploits the insights from a typical conformal transformation optical device and the insights from scattering response of correlated disordered systems to create a disordered graded index metasurface. Unlike the transformation optics structures, the design parameterization for the smooth gradient in the refractive index directly considered the fabrication techniques and the materials available. As a result, we were also able to fabricate them using state-of-the-art techniques for thin-film deposition and validated through comprehensive simulations. The conformal variation in the refractive index distribution significantly reduces reflection losses by effectively suppressing both specular and diffused scattering across the entire spectral range of interest. Additionally, the addition of the GRIN coating relaxes the need for fine-tuned geometric parameters of the nanodisks. Consequently, these structures offer substantial improvements in light absorption, potentially leading to higher photocurrents when integrated into standard solar cell configurations. Such structures also holds promise for thinner solar cells, especially ultra-thin c-Si solar cells, where direct texturing of the absorber layer may be challenging but achieving effective antireflection and light-trapping is more crucial.

6 Conclusion and Outlook

This thesis extensively investigated the utilization of correlated disorder in the design of light-trapping and anti-reflective structures for planar crystalline silicon (c-Si) solar cells. These structures aim to mitigate the degraded electrical properties of a textured solar cell. This degradation is due to increased surface recombination current from the surface nanotexturing. In this chapter, we provide a summary of the findings presented in previous chapters and explore potential avenues for future research.

First, we explored the idea of using transformation optics (TrO) to design an inhomogeneous refractive index, which can directly be integrated onto a planar solar cell. The design of this structure relied on using conformal coordinate transformations for mapping the semi-infinite half-space above the textured interface onto a planar equivalent. Then, the details of the coordinate transformation are interpreted in terms of a material distribution in the original space. The resulting graded index structures have similar optical functionality as a textured interface and are anticipated to have improved electrical properties. We find that such a design approach directly correlates the spatial features of a correlated disordered texture to spatial features in the material distribution thereby fully characterizing the disordered texture. Our results indicate that, with careful choice of the statistical properties of the texture properties, its equivalent planar structure can enhance absorbance in a 1 µm thick film of c-Si wafer close to the textured c-Si counterpart and also outperform a broadband gradient AR coating with a similar refractive index range. Best results are reported for structures with a disorder where both, the texture and its planar counterpart, approach the Lambertian limit for 1D textured interface. When compared to the photocurrent of a 1 µm bare c-Si layer, the photocurrent for the optimal textured interface was reported to be 1.57 times greater while that of the TrO structure was found to be 1.39 times greater.

In the next chapter, we studied how the positional disorder of discrete scattering elements in a system can be tuned using the collective coordinate method (CCM) to give a target structure factor $\tilde{S}(\boldsymbol{q})$. Using CCM, we generated disordered stealthy hyperuniform particle configurations that completely suppress single-scattering for a subset of wave-vectors. This particle distribution was used for designing a disordered metasurface with TiO_2 nanocylinders. With finite-difference time-domain simulations, we showed that such metasurfaces operate quite comparably to an infinite square lattice of the same nanocylinders by yielding comparable reflected photocurrent. A nearly hyperuniform particle configuration was considered at a later stage, which could be realized experimentally using a self-assembly technique. The metasurface designed with this particle configuration was found to have comparable optical performance to the stealthy disordered case. For such systems where the particle configurations are a steady-state outcome of an interaction process, we demonstrated how considering a small-sized sample of the same process degrades the statistical stability of its optical response. By using the CCM, we generate a small-sized sample whose scattering properties are optimized to have the scattering features of a large-sized sample containing hundreds of scatterers. With this approach, we show that our optimized samples can be used as a standalone simulation object, circumventing the need for ensemble averages of the optical response.

In the next chapter, we reconsidered the graded index structures for planar solar cells. However, the design strategy for such structures fully appreciates the state-of-the-art fabrication techniques and the materials available to us. The experimental routine first involves a self-organization process that places TiO_2 nanodisks atop a planar silicon wafer in a nearly hyperuniform disorder arrangement. Second, the desired refractive index gradient is obtained by using atomic layer deposition to deposit layer-by-layer thin films of smoothly varying refractive index. The conformally varying refractive index of each individual thin-film coating is carefully adjusted by tuning the ratio of two materials deposited in that layer. Numerically, such a structure is obtained by linearly interpolating between the same two materials. The spatial distribution of the weights that interpolate the materials then fully characterizes the inhomogeneity of the system. These weights are obtained by numerically solving Laplace's equation in space for a set of boundary conditions to give the conformal variation representative of the experiments. We numerically and experimentally demonstrate that the disordered graded index metasurface designed this way offers much lower reflection loss throughout the spectral range of interest. Furthermore, such a metasurface considerably relaxes the constraints of fine-tuned geometric parameters of the nanodisks, as all such structures yield considerably high absorption enhancement with the potential of yielding a higher photocurrent upon integration into a standard solar cell stack.

In summary, this thesis presents a new perspective on the design strategies that can be adopted for a light-trapping and anti-reflection structure, in the context of planar solar cells. Our approach involves designing a spatially inhomogeneous distribution of material. It relied on the primary notion that a smooth index variation along the normal direction (axis of illumination) is already a well-established solution for broadband anti-reflection in solar cells. By introducing index variation along the lateral direction, the incoupled light can be scattered inside the absorbing medium of the solar cell at oblique angles, thereby giving light-trapping in the system. Unlike the normal direction index variation, which is typically a polynomial function of height, the lateral features in the index are not intuitive. By using the TrO approach, the resulting index distribution was found to contain both the normal and lateral features, with the lateral features being a direct consequence of the properties of the texture used to generate it. Alternatively, these lateral features were also created using a hyperuniform disordered arrangement of dielectric nanodisks, generated using CCM. By using this approach to design a GRIN metasurface, the resulting index distribution contained similar features, with the lateral features arriving from the disordered nanodisks underneath the gradient layer coating. Moreover, the final metasurface designed here could target the parameter space offered by the experiments.

While this thesis addresses the major experimental and computational challenges for adopting a correlated disorder approach to light-trapping, we still identify a few aspects that were outside the scope of this thesis that can prospectively be studied in the future.

The idea of multiple species of scatterers with different geometrical and optical properties being individually and collectively hyperuniform was introduced in Chap. 4 through the concept of multihyperuniformity. Till now, these systems have primarily been studied only using structure factor. Such systems can be very useful for a disordered metasurface designed for a solar cell. Since the spectral response of a solar cell is desired to be broadband, a multihyperuniform disordered metasurface can potentially target different spectral regions by optimizing the response of each individual species comprising it. This will considerably relax the criteria of having an optimal arrangement of identical scatterers that yield a broadband absorption enhancement. Moreover, by targeting a nearly hyperuniform arrangement, as opposed to the stealthy one presented in this thesis, such metasurfaces could also be potentially fabricated on large surfaces. The choice of the individual scatterers for each species then remains a subject for further research.

While we claim that the structures investigated in this thesis can be placed on a planar solar cell, it is worth mentioning that these structures, from the top interface, are not planar. For fully incorporating such structures in a final solar cell device, an encapsulate like, Ethyl-vinyl Acetate (EVA), must be coated above. This will maintain the structural integrity of the nanostructures as well as the metallic contacts of the solar cell. Since this encapsulant will replace the semi-infinite half-space of air considered in Chap. 4 and Chap. 5, it would be necessary to first, study the optical response of this geometry and later, incoherently consider the Air-EVA interface, similar to Chap. 3.

The disordered metasurfaces presented in Chap. 4 and Chap. 5 are used for a c-Si wafer of hundreds of microns thickness. To study the actual light-trapping performance of these structures, it would be important to also consider thin-film absorbing layers, like those considered in Chap. 3. For a thin-film solar cell, the angular distribution of the scattered light into the absorbing layer would play a crucial role in enhancing the absorption of incident light. For such devices, the optimal parameter space would then drift away from the optimal parameters obtained in this thesis. The optimization of such systems would be of particular interest as the industry moves towards thin-film solar cells.

Bibliography

P1. Dhawan, P., Gaudig, M., Sprafke, A., Wehrspohn, R. B. & Rockstuhl, C. Light-trapping structures for planar solar cells inspired by transformation optics. *Optics Express* **29,** 19903–19919 (2021).

P2. Dhawan, P., Schulte, L., Piechulla, P., Augenstein, Y., Gaudig, M., Sprafke, A., Wehrspohn, R. B. & Rockstuhl, C. On the reliability of the collective coordinate method to simulate metasurfaces with correlated disorder used for light management. *Journal of the Optical Society of America B* **40,** B8–B18 (2023).

P3. Piechulla, P. M., Slivina, E., Bätzner, D., Fernandez-Corbaton, I., Dhawan, P., Wehrspohn, R. B., Sprafke, A. N. & Rockstuhl, C. Antireflective Huygens' metasurface with correlated disorder made from high-index disks implemented into silicon heterojunction solar cells. *ACS Photonics* **8,** 3476–3485 (2021).

P4. Dhawan, P., Gaudig, M., Sprafke, A., Piechulla, P., Wehrspohn, R. B. & Rockstuhl, C. Anti-Reflective Graded-Index Metasurface with Correlated Disorder for Light Management in Planar Silicon Solar Cells. *Advanced Optical Materials,* 2302964 (2024).

1. Simonin, L. L. Industrial applications of Solar heat. *Popular Science Monthly* **9,** 550 (1876).
2. Fritts, C. E. ART. LII.–On a New Form of Selenium Cell, and some Electrical Discoveries made by its use. *American Journal of Science (1880-1910)* **26,** 465 (1883).
3. Umweltbundesamt. Erneuerbare Energien in Deutschland, Daten zur Entwicklung im Jahr 2022. `https://www.umweltbundesamt.de/publikationen/erneuerbare-energien-in-deutschland-2022` (2023).
4. Wirth, H. Recent Facts about Photovoltaics in Germany. *Fraunhofer ISE report.* `https://www.ise.fraunhofer.de/en/publications/studies/recent-%20facts-about-pv-in-germany.html` (2023).
5. Green, M., Dunlop, E., Hohl-Ebinger, J., Yoshita, M., Kopidakis, N. & Hao, X. Solar cell efficiency tables (version 57). *Progress in photovoltaics: research and applications* **29,** 3–15 (2021).
6. Shockley, W. & Queisser, H. J. Detailed Balance Limit of Efficiency of p-n Junction Solar Cells. *Journal of Applied Physics* **32,** 510–519 (Mar. 1961).
7. Schygulla, P., Múller, R., Hóhn, O., Schachtner, M., Chojniak, D., Cordaro, A., Tabernig, S., Blási, B., Polman, A., Siefer, G., Lackner, D. & Dimroth, F. Wafer-bonded two-terminal III-V//Si triple-junction solar cell with power conversion efficiency of 36.1% at AM1.5g. *Proceedings of European Photovoltaic Solar Energy Conference, Lisbon, Progress in Photovoltaics* (2023).

8. Maldonado, S. The importance of new “sand-to-silicon” processes for the rapid future increase of photovoltaics. *ACS Energy Letters* **5,** 3628–3632 (2020).
9. Berry, F., Mermet-Lyaudoz, R., Cuevas Davila, J. M., Djemmah, D. A., Nguyen, H. S., Seassal, C., Fourmond, E., Chevalier, C., Amara, M. & Drouard, E. Light Management in Perovskite Photovoltaic Solar Cells: A Perspective. *Advanced Energy Materials* **12,** 2200505 (2022).
10. Sprafke, A. N. & Wehrspohn, R. B. Light Trapping Concepts for Photon Management in Solar Cells. *Green* **2,** 177–187. ISSN: 1869-8778. (2022) (Sept. 2012).
11. Yablonovitch, E. Statistical ray optics. *Journal of the Optical Society of America* **72,** 899–907 (1982).
12. Otto, M., Algasinger, M., Branz, H., Gesemann, B., Gimpel, T., Füchsel, K., Käsebier, T., Kontermann, S., Koynov, S., Li, X., Naumann, V., Oh, J., Sprafke, A. N., Ziegler, J., Zilk, M. & Wehrspohn, R. B. Black silicon photovoltaics. *Advanced Optical Materials* **3,** 147–164 (2015).
13. Fan, Z., Cui, D., Zhang, Z., Zhao, Z., Chen, H., Fan, Y., Li, P., Zhang, Z., Xue, C. & Yan, S. Recent progress of black silicon: From fabrications to applications. *Nanomaterials* **11,** 41 (2020).
14. Wang, S., Xie, T., Liang, R., Zhang, Y., Ma, F.-J., Payne, D., Scardera, G. & Hoex, B. An artificial-intelligence-assisted investigation on the potential of black silicon nanotextures for silicon solar cells. *ACS Applied Nano Materials* **5,** 11636–11647 (2022).
15. Otto, M., Kroll, M., Käsebier, T., Salzer, R., Tünnermann, A. & Wehrspohn, R. B. Extremely low surface recombination velocities in black silicon passivated by atomic layer deposition. *Applied Physics Letters* **100,** 191603 (2012).
16. Gaudig, M., Hirsch, J., Schneider, T., Sprafke, A. N., Ziegler, J., Bernhard, N. & Wehrspohn, R. B. Properties of black silicon obtained at room-temperature by different plasma modes. *Journal of Vacuum Science & Technology A: Vacuum, Surfaces, and Films* **33,** 05E132 (2015).
17. Munday, J. N. & Atwater, H. A. Large integrated absorption enhancement in plasmonic solar cells by combining metallic gratings and antireflection coatings. *Nano Letters* **11,** 2195–2201 (2011).
18. Bhattacharya, S., Baydoun, I., Lin, M. & John, S. Towards 30% power conversion efficiency in thin-silicon photonic-crystal solar cells. *Physical Review Applied* **11,** 014005 (2019).
19. Grandidier, J., Callahan, D. M., Munday, J. N. & Atwater, H. A. Light absorption enhancement in thin-film solar cells using whispering gallery modes in dielectric nanospheres. *Advanced Materials* **23,** 1272–1276 (2011).
20. Elshorbagy, M., Abdel-Hady, K., Kamal, H. & Alda, J. Broadband anti-reflection coating using dielectric Si3N4 nanostructures. Application to amorphous-Si-H solar cells. *Optics Communications* **390,** 130–136 (2017).

21. Elshorbagy, M. H., López-Fraguas, E., Sánchez-Pena, J. M., García-Cámara, B. & Vergaz, R. Boosting ultrathin aSi-H solar cells absorption through a nanoparticle cross-packed metasurface. *Solar Energy* **202,** 10–16 (2020).
22. Tavakoli, N., Spalding, R., Lambertz, A., Koppejan, P., Gkantzounis, G., Wan, C., Röhrich, R., Kontoleta, E., Koenderink, A. F., Sapienza, R., *et al.* Over 65% sunlight absorption in a 1 μm Si slab with hyperuniform texture. *ACS Photonics* **9,** 1206–1217 (2022).
23. Piechulla, P. M., Muehlenbein, L., Wehrspohn, R. B., Nanz, S., Abass, A., Rockstuhl, C. & Sprafke, A. Fabrication of Nearly-Hyperuniform Substrates by Tailored Disorder for Photonic Applications. *Advanced Optical Materials* **6,** 1701272 (2018).
24. Zhao, Y., Chen, F., Shen, Q. & Zhang, L. Optimal design of light trapping in thin-film solar cells enhanced with graded SiN x and SiO x N y structure. *Optics Express* **20,** 11121–11136 (2012).
25. Fahr, S., Ulbrich, C., Kirchartz, T., Rau, U., Rockstuhl, C. & Lederer, F. Rugate filter for light-trapping in solar cells. *Optics Express* **16,** 9332–9343 (2008).
26. Ge, Z., Rajbhandari, P., Hu, J., Emrani, A., Dhakal, T. P., Westgate, C. & Klotzkin, D. Enhanced omni-directional performance of copper zinc tin sulfide thin film solar cell by gradient index coating. *Applied Physics Letters* **104,** 101104 (2014).
27. Jackson, J. D. *Classical electrodynamics* (John Wiley & Sons, 2021).
28. Johnson, S. G. *Coordinate transformation and invariance in electro- magnetism,* `https://math.mit.edu/~stevenj/18.369/coordinate-transform.pdf` (MIT course 18.369 (Massachusetts Institute of Technology: MIT OpenCourseWare), License: Creative Commons BY-NC-SA, 2007, 2007).
29. Novotny, L. & Hecht, B. *Principles of nano-optics* (Cambridge university press, 2012).
30. Fernandez-Corbaton, I., Zambrana-Puyalto, X. & Molina-Terriza, G. Helicity and angular momentum: A symmetry-based framework for the study of light-matter interactions. *Physical Review A* **86,** 042103 (2012).
31. Fernandez-Corbaton, I. *Helicity and duality symmetry in light matter interactions: Theory and applications* in *Laser Science* (2015), LM1H–2.
32. Fernandez-Corbaton, I. & Molina-Terriza, G. Role of duality symmetry in transformation optics. *Physical Review B* **88,** 085111 (2013).
33. Bialynicki-Birula, I. V photon wave function. *Progress in Optics* **36,** 245–294 (1996).
34. Leonhardt, U. & Philbin, T. *Geometry and light: the science of invisibility* (Courier Corporation, 2010).
35. Pendry, J. B., Schurig, D. & Smith, D. R. Controlling electromagnetic fields. *Science* **312,** 1780–1782 (2006).
36. Valentine, J., Li, J., Zentgraf, T., Bartal, G. & Zhang, X. An optical cloak made of dielectrics. *Nature Materials* **8,** 568–571 (2009).

37. Eskandari, H. & Tyc, T. Controlling refractive index of transformation-optics devices via optical path rescaling. *Scientific Reports* **9,** 18412 (2019).
38. Kadic, M., Guenneau, S., Enoch, S., Huidobro, P. A., Martin-Moreno, L., García-Vidal, F. J., Renger, J. & Quidant, R. Transformation plasmonics. *Nanophotonics* **1,** 51–64 (2012).
39. Rahm, M., Roberts, D., Pendry, J. & Smith, D. Transformation-optical design of adaptive beam bends and beam expanders. *Optics Express* **16,** 11555–11567 (2008).
40. Roberts, D., Rahm, M., Pendry, J. & Smith, D. Transformation-optical design of sharp waveguide bends and corners. *Applied Physics Letters* **93,** 251111 (2008).
41. Li, S., Zhou, Y., Dong, J., Zhang, X., Cassan, E., Hou, J., Yang, C., Chen, S., Gao, D. & Chen, H. Universal multimode waveguide crossing based on transformation optics. *Optica* **5,** 1549–1556 (2018).
42. Ni, X., Emani, N. K., Kildishev, A. V., Boltasseva, A. & Shalaev, V. M. Broadband light bending with plasmonic nanoantennas. *Science* **335,** 427–427 (2012).
43. Luo, Y., Lei, D. Y., Maier, S. A. & Pendry, J. B. Transformation-optics description of plasmonic nanostructures containing blunt edges/corners: from symmetric to asymmetric edge rounding. *ACS Nano* **6,** 6492–6506 (2012).
44. Tao, S., Zhou, Y. & Chen, H. Maxwell's fish-eye lenses under Schwartz-Christoffel mappings. *Physical Review A* **99,** 013837 (2019).
45. Kundtz, N. & Smith, D. R. Extreme-angle broadband metamaterial lens. *Nature Materials* **9,** 129–132 (2010).
46. Yang, R., Tang, W. & Hao, Y. A broadband zone plate lens from transformation optics. *Optics Express* **19,** 12348–12355 (2011).
47. Liang, L. & Hum, S. V. Wide-angle scannable reflector design using conformal transformation optics. *Optics Express* **21,** 2133–2146 (2013).
48. McCall, M. *et al.* Roadmap on transformation optics. *Journal of Optics* **20,** 063001 (2018).
49. Kinsler, P. & McCall, M. W. The futures of transformations and metamaterials. *Photonics and Nanostructures-Fundamentals and Applications* **15,** 10–23 (2015).
50. Werner, D. H. & Kwon, D.-H. *Transformation electromagnetics and metamaterials* (Springer, 2013).
51. Turpin, J. P., Massoud, A. T., Jiang, Z. H., Werner, P. L. & Werner, D. H. Conformal mappings to achieve simple material parameters for transformation optics devices. *Optics Express* **18,** 244–252 (2010).
52. Driscoll, T. A. & Trefethen, L. N. *Schwarz-Christoffel mapping* (Cambridge University, 2002).
53. Driscoll, T. A. Algorithm 756: A MATLAB toolbox for Schwarz-Christoffel mapping. *ACM Transactions on Mathematical Software (TOMS)* **22,** 168–186 (1996).

54. Tang, L., Yin, J., Yuan, G., Du, J., Gao, H., Dong, X., Lu, Y. & Du, C. General conformal transformation method based on Schwarz-Christoffel approach. *Optics Express* **19,** 15119–15126 (2011).
55. Schmiele, M., Varma, V. S., Rockstuhl, C. & Lederer, F. Designing optical elements from isotropic materials by using transformation optics. *Physical Review A* **81,** 033837 (2010).
56. Würfel, P. & Würfel, U. *Physics of solar cells: from basic principles to advanced concepts* (John Wiley & Sons, 2016).
57. Gueymard, C. A., Myers, D. & Emery, K. Proposed reference irradiance spectra for solar energy systems testing. *Solar Energy* **73,** 443–467 (2002).
58. Born, M. & Wolf, E. *Principles of optics: electromagnetic theory of propagation, interference and diffraction of light* (Elsevier, 2013).
59. Southwell, W. H. Gradient-Index Antireflection Coatings. *Optical Letters* **8,** 584–586 (1983).
60. Poitras, D. & Dobrowolski, J. Toward perfect antireflection coatings. 2. Theory. *Applied Optics* **43,** 1286–1295 (2004).
61. Freilikher, V., Kanzieper, E. & Maradudin, A. Coherent scattering enhancement in systems bounded by rough surfaces. *Physics Reports* **288,** 127–204 (1997).
62. Vynck, K., Pierrat, R., Carminati, R., Froufe-Pérez, L. S., Scheffold, F., Sapienza, R., Vignolini, S. & Sáenz, J. J. Light in correlated disordered media. *arXiv preprint arXiv:2106.13892* (2021).
63. Torquato, S. & Stillinger, F. H. Local density fluctuations, hyperuniformity, and order metrics. *Physical Review E* **68,** 041113 (2003).
64. Uche, O. U., Torquato, S. & Stillinger, F. H. Collective coordinate control of density distributions. *Physical Review E* **74,** 031104 (2006).
65. Torquato, S. & Haslach Jr, H. Random heterogeneous materials: microstructure and macroscopic properties. *Applied Mechanics Reviews* **55,** B62–B63 (2002).
66. Crawford, J., Torquato, S. & Stillinger, F. H. Aspects of correlation function realizability. *The Journal of Chemical Physics* **119,** 7065–7074 (2003).
67. Fletcher, R. A new approach to variable metric algorithms. *The Computer Journal* **13,** 317–322 (1970).
68. Liu, D. C. & Nocedal, J. On the limited memory BFGS method for large scale optimization. *Mathematical Programming* **45,** 503–528 (1989).
69. Arslan, D. "Positional disorder in Huygens' metasurfaces", *PhD thesis,* Friedrich Schiller University Jena (2022).
70. Torquato, S. Hyperuniformity and its generalizations. *Physical Review E* **94,** 022122 (2016).
71. Torquato, S. Hyperuniform states of matter. *Physics Reports* **745,** 1–95 (2018).
72. Beck, J. Irregularities of distribution. I (1987).

73. Yee, K. Numerical solution of initial boundary value problems involving Maxwell's equations in isotropic media. *IEEE Transactions on Antennas and Propagation* **14,** 302–307 (1966).

74. Taflove, A., Hagness, S. C. & Piket-May, M. Computational electromagnetics: the finite-difference time-domain method. *The Electrical Engineering Handbook* **3,** 15 (2005).

75. Oskooi, A. F., Roundy, D., Ibanescu, M., Bermel, P., Joannopoulos, J. & Johnson, S. G. Meep: A flexible free-software package for electromagnetic simulations by the FDTD method. *Computer Physics Communications* **181,** 687–702 (Mar. 2010).

76. Fahr, S., Kirchartz, T., Rockstuhl, C. & Lederer, F. Approaching the Lambertian limit in randomly textured thin-film solar cells. *Optics Express* **19,** A865–A874 (2011).

77. Hsu, W.-C., Tong, J. K., Branham, M. S., Huang, Y., Yerci, S., Boriskina, S. V. & Chen, G. Mismatched front and back gratings for optimum light trapping in ultra-thin crystalline silicon solar cells. *Optics Communications* **377,** 52–58 (2016).

78. Tamang, A., Hongsingthong, A., Jovanov, V., Sichanugrist, P., Khan, B. A., Dewan, R., Konagai, M. & Knipp, D. Enhanced photon management in silicon thin film solar cells with different front and back interface texture. *Scientific Reports* **6,** 1–10 (2016).

79. Jäger, K., Fischer, M., van Swaaij, R. A. & Zeman, M. Designing optimized nano textures for thin-film silicon solar cells. *Optics Express* **21,** A656–A668 (2013).

80. Pratesi, F., Burresi, M., Riboli, F., Vynck, K. & Wiersma, D. S. Disordered photonic structures for light harvesting in solar cells. *Optics Express* **21,** A460–A468 (2013).

81. Meng, X., Drouard, E., Gomard, G., Peretti, R., Fave, A. & Seassal, C. Combined front and back diffraction gratings for broad band light trapping in thin film solar cell. *Optics Express* **20,** A560–A571 (2012).

82. Bozzola, A., Liscidini, M. & Andreani, L. C. Photonic light-trapping versus Lambertian limits in thin film silicon solar cells with 1D and 2D periodic patterns. *Optics Express* **20,** A224–A244 (2012).

83. Ferry, V. E., Polman, A. & Atwater, H. A. Modeling light trapping in nanostructured solar cells. *ACS Nano* **5,** 10055–10064 (2011).

84. Lee, Y.-C., Huang, C.-F., Chang, J.-Y. & Wu, M.-L. Enhanced light trapping based on guided mode resonance effect for thin-film silicon solar cells with two filling-factor gratings. *Optics Express* **16,** 7969–7975 (2008).

85. Abass, A., Le, K. Q., Alu, A., Burgelman, M. & Maes, B. Dual-interface gratings for broadband absorption enhancement in thin-film solar cells. *Physical Review B* **85,** 115449 (2012).

86. Zaidi, S. H., Ruby, D. S. & Gee, J. M. Characterization of random reactive ion etched-textured silicon solar cells. *IEEE Transactions on Electron Devices* **48,** 1200–1206 (2001).

87. Sakai, H., Yoshida, T., Hama, T. & Ichikawa, Y. Effects of surface morphology of transparent electrode on the open-circuit voltage in a-Si: H solar cells. *Japanese Journal of Applied Physics* **29,** 630 (1990).

88. Python, M., Dominé, D., Söderström, T., Meillaud, F. & Ballif, C. Microcrystalline silicon solar cells: effect of substrate temperature on cracks and their role in post-oxidation. *Progress in Photovoltaics: Research and Applications* **18,** 491–499 (2010).

89. Schumann, M. F., Wiesendanger, S., Goldschmidt, J. C., Bläsi, B., Bittkau, K., Paetzold, U. W., Sprafke, A., Wehrspohn, R. B., Rockstuhl, C. & Wegener, M. Cloaked contact grids on solar cells by coordinate transformations: designs and prototypes. *Optica* **2,** 850–853 (2015).

90. Schumann, M. F., Langenhorst, M., Smeets, M., Ding, K., Paetzold, U. W. & Wegener, M. All-Angle Invisibility Cloaking of Contact Fingers on Solar Cells by Refractive Free-Form Surfaces. *Advanced Optical Materials* **5,** 1700164 (2017).

91. Schumann, M. F., Abass, A., Gomard, G., Wiesendanger, S., Lemmer, U., Wegener, M. & Rockstuhl, C. Single-pass and omniangle light extraction from light-emitting diodes using transformation optics. *Optics Letters* **40,** 5626–5629 (2015).

92. Nguyen, H. T., Rougieux, F. E., Mitchell, B. & Macdonald, D. Temperature dependence of the band-band absorption coefficient in crystalline silicon from photoluminescence. *Journal of Applied Physics* **115,** 043710 (2014).

93. Jiang, Y., Pillai, S. & Green, M. A. Realistic silver optical constants for plasmonics. *Scientific Reports* **6,** 30605 (2016).

94. Harris, F. J. On the use of windows for harmonic analysis with the discrete Fourier transform. *Proceedings of the IEEE* **66,** 51–83 (1978).

95. Yu, Z., Raman, A. & Fan, S. Fundamental limit of light trapping in grating structures. *Optics Express* **18,** A366–A380 (2010).

96. Jäger, K., Köppel, G., Hammerschmidt, M., Burger, S. & Becker, C. On accurate simulations of thin-film solar cells with a thick glass superstrate. *Optics Express* **26,** A99–A107 (2018).

97. Hafermann, M., Schöppe, P., Rensberg, J. & Ronning, C. Metasurfaces enabled by locally tailoring disorder in phase-change materials. *ACS Photonics* **5,** 5103–5109 (2018).

98. Rahimzadegan, A., Arslan, D., Dams, D., Groner, A., Garcia-Santiago, X., Alaee, R., Fernandez-Corbaton, I., Pertsch, T., Staude, I. & Rockstuhl, C. Beyond dipolar Huygens' metasurfaces for full-phase coverage and unity transmittance. *Nanophotonics* **9,** 75–82 (2020).

99. Jang, M., Horie, Y., Shibukawa, A., Brake, J., Liu, Y., Kamali, S. M., Arbabi, A., Ruan, H., Faraon, A. & Yang, C. Wavefront shaping with disorder-engineered metasurfaces. *Nature Photonics* **12,** 84–90 (2018).

100. Haghtalab, M., Tamagnone, M., Zhu, A. Y., Safavi-Naeini, S. & Capasso, F. Ultrahigh angular selectivity of disorder-engineered metasurfaces. *ACS Photonics* **7,** 991–1000 (2020).

101. John, S. Strong localization of photons in certain disordered dielectric superlattices. *Physical Review Letters* **58,** 2486 (1987).

102. Segev, M., Silberberg, Y. & Christodoulides, D. N. Anderson localization of light. *Nature Photonics* **7,** 197–204 (2013).

103. Florescu, M., Steinhardt, P. J. & Torquato, S. Optical cavities and waveguides in hyperuniform disordered photonic solids. *Physical Review B* **87,** 165116 (2013).

104. Huisman, S. R., Huisman, T. J., Wolterink, T. A., Mosk, A. P. & Pinkse, P. W. Programmable multiport optical circuits in opaque scattering materials. *Optics Express* **23,** 3102–3116 (2015).

105. Yu, S., Qiu, C.-W., Chong, Y., Torquato, S. & Park, N. Engineered disorder in photonics. *Nature Reviews Materials* **6,** 226–243 (2021).

106. Rothammer, M., Zollfrank, C., Busch, K. & von Freymann, G. Tailored disorder in photonics: Learning from nature. *Advanced Optical Materials* **9,** 2100787 (2021).

107. Bigourdan, F., Pierrat, R. & Carminati, R. Enhanced absorption of waves in stealth hyperuniform disordered media. *Optics Express* **27,** 8666–8682 (2019).

108. Paetzold, U., Smeets, M., Meier, M., Bittkau, K., Merdzhanova, T., Smirnov, V., Michaelis, D., Waechter, C., Carius, R. & Rau, U. Disorder improves nanophotonic light trapping in thin-film solar cells. *Applied Physics Letters* **104,** 131102 (2014).

109. Hauser, H., Mühlbach, K., Höhn, O., Müller, R., Seitz, S., Rühe, J., Glunz, S. W. & Bläsi, B. Tailored disorder: a self-organized photonic contact for light trapping in silicon-based tandem solar cells. *Optics Express* **28,** 10909–10918 (2020).

110. Bozzola, A., Liscidini, M. & Andreani, L. C. Broadband light trapping with disordered photonic structures in thin-film silicon solar cells. *Progress in Photovoltaics: Research and Applications* **22,** 1237–1245 (2014).

111. Coenen, T., van de Groep, J. & Polman, A. Resonant Modes of Single Silicon Nanocavities Excited by Electron Irradiation. *ACS Nano* **7,** 1689–1698 (2013).

112. Kerker, M., Wang, D.-S. & Giles, C. L. Electromagnetic scattering by magnetic spheres. *Journal of the Optical Society of America* **73,** 765 (1983).

113. Slivina, E., Abass, A., Baetzner, D., Strahm, B., Rockstuhl, C. & Fernandez-Corbaton, I. Insights into Backscattering Suppression in Solar Cells from the Helicity-Preservation Point of View. *Physical Review Applied* **12,** 054003 (2019).

114. Spinelli, P., Verschuuren, M. & Polman, A. Broadband omnidirectional antireflection coating based on subwavelength surface Mie resonators. *Nature Communications* **3,** 692 (2012).

115. Fernandez-Corbaton, I. Forward and backward helicity scattering coefficients for systems with discrete rotational symmetry. *Optics Express* **21,** 29885 (Nov. 2013).

116. Piechulla, P. M., Fuhrmann, B., Slivina, E., Rockstuhl, C., Wehrspohn, R. B. & Sprafke, A. N. Tailored Light Scattering through Hyperuniform Disorder in Self-Organized Arrays of High-Index Nanodisks. *Advanced Optical Materials* **9,** 2100186 (June 2021).

117. Uche, O. U., Stillinger, F. H. & Torquato, S. Constraints on collective density variables: Two dimensions. *Physical Review E* **70,** 046122 (2004).

118. Leseur, O., Pierrat, R. & Carminati, R. High-density hyperuniform materials can be transparent. *Optica* **3,** 763–767 (2016).

119. Gorsky, S., Britton, W. A., Chen, Y., Montaner, J., Lenef, A., Raukas, M. & Negro, L. D. Engineered hyperuniformity for directional light extraction. *APL Photonics* **4,** 110801 (Nov. 2019).

120. Florescu, M., Torquato, S. & Steinhardt, P. J. Designer disordered materials with large, complete photonic band gaps. *Proceedings of the National Academy of Sciences* **106,** 20658–20663 (2009).

121. Torquato, S., Zhang, G. & Stillinger, F. H. Ensemble theory for stealthy hyperuniform disordered ground states. *Physical Review X* **5,** 021020 (2015).

122. Batten, R. D., Stillinger, F. H. & Torquato, S. Classical disordered ground states: Super-ideal gases and stealth and equi-luminous materials. *Journal of Applied Physics* **104** (2008).

123. Jiao, Y., Lau, T., Hatzikirou, H., Meyer-Hermann, M., Corbo, J. C. & Torquato, S. Avian photoreceptor patterns represent a disordered hyperuniform solution to a multiscale packing problem. *Physical Review E* **89,** 022721 (2014).

124. Kim, J. & Torquato, S. Effect of imperfections on the hyperuniformity of many-body systems. *Physical Review B* **97,** 054105 (2018).

125. Torquato, S., Uche, O. & Stillinger, F. Random sequential addition of hard spheres in high Euclidean dimensions. *Physical Review E* **74,** 061308 (2006).

126. Piechulla, P. M., Slivina, E., Baetzner, D., Fernandez-Corbaton, I., Dhawan, P., Wehrspohn, R. B., Sprafke, A. N. & Rockstuhl, C. Antireflective Huygens' Metasurface with Correlated Disorder Made from High-Index Disks Implemented into Silicon Heterojunction Solar Cells. *ACS Photonics* **8,** 3476–3485. `https://doi.org/10.1021/acsphotonics.1c00601` (Dec. 2021).

127. Davis, K. O., Jiang, K., Habermann, D. & Schoenfeld, W. V. Tailoring the optical properties of APCVD titanium oxide films for all-oxide multilayer antireflection coatings. *IEEE Journal of Photovoltaics* **5,** 1265–1270 (2015).

128. Akiba, T., Sano, S., Yanase, T., Ohta, T. & Koyama, M. Optuna: A next-generation hyperparameter optimization framework. *Proceedings of the 25th ACM SIGKDD international conference on knowledge discovery & data mining,* 2623–2631 (2019).

129. Piechulla, P. M., Fuhrmann, B., Slivina, E., Rockstuhl, C., Wehrspohn, R. B. & Sprafke, A. N. Tailored Light Scattering through Hyperuniform Disorder in Self-Organized Arrays of High-Index Nanodisks. *Advanced Optical Materials* **9,** 2100186 (2021).

130. Kong, J. A., Tsang, L., Ding, K.-H. & Ao, C. O. *Scattering of electromagnetic waves: numerical simulations* (John Wiley & Sons, 2004).
131. Vynck, K., Pacanowski, R., Agreda, A., Dufay, A., Granier, X. & Lalanne, P. The visual appearances of disordered optical metasurfaces. *Nature Materials* **21,** 1035–1041 (2022).
132. Dubrovin, B., Fomenko, A. & Novikov, S. *Modern Geometry–Methods and Applications, Part I, 2nd English edition* 1992.
133. Blair, D. E. *Inversion theory and conformal mapping* (American Mathematical Society, 2000).
134. Berry, E. A., Gutierrez, J. & Rumpf, R. C. Design and simulation of arbitrarily-shaped transformation optic devices using a simple finite-difference method. *Progress In Electromagnetics Research B* **68,** 1–16 (2016).
135. Quevedo-Teruel, O., Tang, W., Mitchell-Thomas, R. C., Dyke, A., Dyke, H., Zhang, L., Haq, S. & Hao, Y. Transformation optics for antennas: why limit the bandwidth with metamaterials? *Scientific Reports* **3,** 1903 (2013).
136. Kaděra, P., Sánchez-Pastor, J., Eskandari, H., Tyc, T., Sakaki, M., Schüßler, M., Jakoby, R., Benson, N., Jiménez-Sáez, A. & Láčík, J. Wide-angle ceramic retroreflective luneburg lens based on quasi-conformal transformation optics for mm-wave indoor localization. *IEEE Access* **10,** 41097–41111 (2022).
137. Sprafke, A. N. & Wehrspohn, R. B. in *Photon Management in Solar Cells* (eds Wehrspohn, R. B., Rau, U. & Gombert, A.) 1–20 (Wiley-VCH Verlag GmbH & Co. KGaA, Weinheim, Germany, 2015). (2022).
138. Zaitsu, S.-i., Jitsuno, T., Nakatsuka, M., Yamanaka, T. & Motokoshi, S. Optical thin films consisting of nanoscale laminated layers. *Applied Physics Letters* **80,** 2442–2444 (2002).
139. Li, Y., Shen, W., Hao, X., Lang, T., Jin, S. & Liu, X. Rugate notch filter fabricated by atomic layer deposition. *Applied Optics* **53,** A270–A275 (2014).
140. Zhang, Y., Nieto-Vesperinas, M. & Sáenz, J. J. Dielectric spheres with maximum forward scattering and zero backscattering: a search for their material composition. *Journal of Optics* **17,** 105612 (2015).

Acknowledgements

Embarking on this doctoral odyssey felt a bit like setting sail on the high seas of academia. And like any intrepid explorer, I could not have navigated this challenging yet exhilarating voyage without my crew of supporters and fellow adventurers.

First and foremost, I would like to extend my heartfelt thanks to my loyal (and vintage) laptop, which has been my steadfast companion throughout this challenging journey. Despite its battle scars, with plastic pieces missing, cooling fan malfunctioning, hinges broken, and a worn-out screen lid, it has remained remarkably resilient and functional, particularly during the turbulent times of the COVID-19 pandemic. Your unwavering support, even in the face of hardware and software troubles, is nothing short of miraculous, and is greatly appreciated.

Throughout this academic odyssey, my main supervisor, Prof. Dr. Carsten Rockstuhl, has been the North Star, unwavering in guidance and support. From the countless manuscript and thesis revisions to having spontaneous online meetings from train stations, your dedication and guidance has been unfaltering, even shining through at 5 A.M. Your mentorship has taught me to better disseminate scientific research and be an independent researcher.

Amid life's unpredictable tides, my family (Jyoti, Deeksha, and Indrapal Dhawan, Vidita Waghle, Zeba Quadri, and my dog, Scooby), have been the anchors, providing support and direction through fair winds and foul. Your love and encouragement remains a guiding light in this voyage. Despite the recent loss of my father, his legacy of strength and resilience will continue inspire me and keep me afloat.

Keeping the nautical metaphors aside, I would also like to thank:

- Prof. Dr. Wehrspohn for accepting to review this thesis.
- Dr. Maria Gaudig, Dr. Alex Sprafke, and Dr. Peter Piechulla from the Martin-Luther-University Halle-Wittenberg with whom I had the privilege of engaging in numerous insightful discussions and fruitful research collaborations, which greatly contributed to my work.
- My mentors during the masters, Dr. Surya Harikrishnan and Dr. Bhooshan Paradkar, whose mentoring, exceptional teaching style and love for physics fueled my enthusiasm for scientific research, setting me on the path to a Ph.D. Your guidance has been invaluable on this academic journey.
- Dr. Ivan Fernandez-Corbaton, Dr. Aristeidis Lamprianidis, Dr. Ramakrishna Venkitakrishna, Yannick Augenstein, Dr. Evgeniia Slivina, Dr. Theodosios Karamanos,

Dr. Marvin Müller, Dr. Aso Rahimzadegan, Mitchell Whittam, Dr. Xavier Garcia-Santiago, Dr. Thomas Sturges, Dominik Beutel, Maria Paszkiewicz, Maxim Vavilin, Nanda Perdana, and Benedikt Zerulla for your valuable insights, and for engaging in countless, trivial and non-trivial, scientific discussions.